Microstructural Evolution of Electrospun Microfibers for Biomedical Applications

Student: Alana Chandler - 1563759
St. Cross College, University of Oxford
Supervisor: Dr. Hazel Assender
MSc by Research
July 2024

Thesis

Acknowledgements

This MSc project was first made possible due to the enriching supervision and guidance of Dr. Hazel Assender in her Polymers Group. Through our countless meetings in the past two years, she not only advised me in investigative techniques, but also shared her profound expertise in polymer theory. I am also grateful for the insightful collaboration with Dr. Pierre-Alexis Mouthuy on his lab's Biolig implant innovation under the Nuffield Department of Orthopaedics, Rheumatology and Musculoskeletal Sciences. Through this partnership, Dr. Mouthuy gave me the opportunity to further explore my primary interest in biomaterials while fostering my understanding and appreciation for the biomedical implications of polymer physics. I gratefully acknowledge the support provided by the Clarendon Scholarship for funding my research and Oxford experience.

I would also like to thank those who provided me invaluable experimental support, namely Richard and Greg for technical assistance; Dr. Colin Johnston and Nicola Flanagan of the Oxford Materials Characterization Service for training me in instrumentation usage; Ryan Schofield for acquiring the 2D XRD images; Dr. Meng Liang for electrospinning Biolig samples; Georgy Grishchenko of Dr. James Marrow's lab for obtaining the uCT scans; Dr. Andrew Lui for XRD support; and Dr. Leonard Thomas for sharing his superb expertise in DSC over e-mail.

I am grateful to the Polymers Group for welcoming me into the Begbroke community and helping me get situated in the lab. Thank you to my family for grounding and encouraging me through thick and thin, as well as serving as my role models for hard work. Thank you to Grandpa, Grandma, and Ojiichan for continuing to fight for their health and exemplifying tenacity. I extend immense gratitude to my wonderful friends — those back home in the U.S., those who I met at Oxford, and my sister. Their curiosity, creativity, and kindness continue to inspire me to depths that my words cannot capture. Lastly, I dedicate this thesis to Yasuko Janado, my late aunt.

Abstract

The mechanical behavior and degradative properties of polymeric materials are closely tied to their microstructure. In the context of medical devices, understanding this relationship is critical for optimizing device performance and longevity. This thesis investigated how the microstructural evolution of a type of microfibrous electrospun (ES) filament evolved during the critical processing step of post-drawing. Specifically studied were filaments designed for use in knee ligament regeneration implants made from biodegradable, semicrystalline polycaprolactone (PCL). The filaments were characterized at both the fiber and molecular levels. At the fiber level, micro-computed tomography (μCT) and scanning electron microscopy (SEM) showed that stretching caused alignment, thinning, and coalescence of the fibers. At the molecular level, the crystalline microarchitecture within the fibers transformed profoundly after stretching. Techniques such as differential scanning calorimetry (DSC), 1D and 2D X-ray diffraction (XRD), and dynamic mechanical thermal analysis (DMTA) were utilized to analyze these changes. The resulting data were used to create a conceptual model of the possible mechanism for stretch-induced microstructural evolution of PCL. The proposed mechanism involves lamellar fragmentation of chain-folded crystals (CFC) and amorphous chain extension at low strains. At higher strains, CFC unfold and recrystallize into thermodynamically more stable chain-extended crystals (CEC) aligned to the stretch axis. These findings suggest potential mechanical and degradative implications for biomedical applications, warranting further investigation.

Keywords: electrospinning, poly-caprolactone, polymer crystals, microfibers, bio-yarn, strain-induced crystallization

Table of Contents

List of Abbreviations

|| ..... parallel
⊥ ..... perpendicular
ACL ..... anterior cruciate ligament
AFM ..... atomic force microscopy
CEC ..... chain-extended crystals
CFC ..... chain-folded crystals
DMTA ..... dynamic mechanical thermal analysis
DSC ..... differential scanning calorimetry
E ..... Young's modulus
ECM ..... Extra Cellular Matrix
ES ..... electrospun
f ..... Herman's orientation factor
FTIR ..... Fourier transform infrared
FWHM ..... full width at half-maximum
G' ..... storage modulus
G'' ..... loss modulus
HFIP ..... hexafluoroisopropanol
IP ..... in-plane
Mw ..... molecular weight
n ..... scalar multiple of original length (1:n)
OOP ..... out-of-plane
PAN ..... polyacrylonitrile
PBS ..... poly(butylene succinate)
PCL ..... polycaprolactone
PDO ..... polydioxanone
PEEK ..... poly(aryl-ether-ether-ketone)
PGA ..... poly(glycolic acid)
PLLA ..... poly(L-lactic acid)
POM ..... polyoxymethylene
PVDF ..... polyvinylidene fluoride
RT ..... room temperature
SAXS ..... small angle X-ray scattering
SD ..... standard deviation
SEM ..... scanning electron microscopy
tan(δ) ..... damping factor
T_g ..... glass transition temperature
T_m ..... melting temperature
X_c ..... crystallinity
XRD ..... X-ray diffraction
β ..... azimuthal angle
θ ..... Bragg angle
μCT ..... micro-computed tomography

1. Introduction

1.1 Electrospun Scaffold for Tissue Regeneration

Implantable polymeric scaffolds can be used to promote tissue regeneration following injury by providing structural support for healing tissue and guiding cell growth. These scaffolds can be engineered to morphologically, mechanically, and/or chemically resemble the biological extracellular matrix (ECM) to allow for optimal cell differentiation and proliferation. Fibrous materials are of particular interest for use in scaffolds, as they possess structures similar to fibrils in the ECM and large surface areas that promote cell adhesion (*1*). Clusters of electrospun (ES) fibers are ideal for such biomedical applications due to their micro- and nano-scale properties, tailorable porosity (> 60-90% void space) for nutrient exchange and tissue interaction, and a 3D matrix structure that mimics the ECM (*2*, *3*). A variety of polymers can be made into biodegradable, biocompatible filaments via electrospinning, including natural polymers — such as silk fibroin, collagen, and gelatin — and synthetic polymers — such as polycaprolactone (PCL), polydioxanone (PDO), poly(glycolic acid) (PGA), poly(L-lactic acid) (PLLA), and copolymers of the aforementioned materials (*1*). In addition, the uniaxial orientation and anisotropic properties of nanofibrous yarns formed from ES fiber bundles have garnered research attention into their potential use in regenerating linear tissues such as ligaments and tendons (*4*).

Electrospinning is an electrohydrodynamic process in which a high-voltage electrostatic field is applied between a polymer solution and a conductive collector (*5*). The solution is contained within a syringe and is gradually ejected from its needle with a syringe pump. First, a pendant droplet forms at the tip of the needle. The applied voltage charges the droplet, leading to the formation of a Taylor cone where Coulombic charge repulsion is high enough for a thin solution

jet to project from the needle towards the oppositely charged collector. The jet experiences bending instabilities as it travels towards the collector, causing the jet to elongate as the solvent from the polymer solution evaporates and deposits on the collector as an interconnected mesh of fibers (*6*). The properties of the fiber can be changed by controlling the parameters of the electrospinning process, including solution viscosity, spinning voltage, and ambient humidity (*5*, *7*). In the most basic electrospinning set up, the collector is static, resulting in a fibrous mat product. Other collector geometries, such as a rotating drum or dynamic wire (Fig. 1.1), can be used to create an aligned or continuous yarn-like product, respectively.

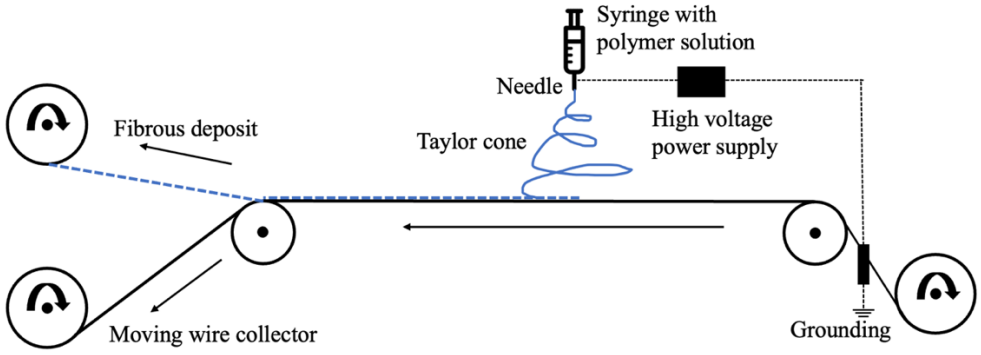

Fig. 1.1 Schematic of unique electrospinning process used to fabricate Biolig, implementing a moving wire collector.

1.2 Bioactive Yarns

Several types of stitching materials exist for ligament repair, including inert, unabsorbable single sutures (e.g., silk, nylon, polypropylene), absorbable single sutures (e.g., PLLA, PGA, PDO), and bioactive yarns (*1*). Single sutures are composed of a simple individual thread that does not mimic morphological features. On the other hand, bioactive yarns mechanically and morphologically approximate tissue while also allowing regenerated tissue to replace the yarn as the material degrades (*8*). Filaments are a specific type of yarn made up of aligned, continuous

bundles of fibers that mimic the hierarchical and anisotropic structure of linear tissue along their longitudinal axis (*9*). They are most commonly produced via melt-spinning (*4*), although electrospinning is a competitive technique that is able to achieve finer diameters and porosities. These characteristics are advantageous in making scaffolds that are designed for endogenous repair. ES yarns, when compared to mats, offer improved mechanics because they can be twisted, braided, or woven into denser, stronger composites (*1*). To date, research into the use of ES yarns for biomechanical applications has pointed to the need for multifilament bundles. For instance, one study found that the use of individual ES yarns lacked sufficient mechanical properties for biomechanical applications (*10*), while another study achieved these properties and successful neovascularization by creating a multifilament from 35 strands of ES yarn twisted together (*11*). When these filaments are made from high-porosity materials, additional benefits may be gained by integrating biological cues and drugs into these materials for controlled release over the patient's regeneration period (*12*).

1.2.1 Biolig

Dr. Pierre-Alexis Mouthuy's laboratory in Oxford's Nuffield Department of Orthopaedics, Rheumatology and Musculoskeletal Sciences is developing Biolig, a degradable synthetic bioactive yarn implanted surgically that structurally supports torn ligaments and stimulates repair (*13*). Biolig was specifically designed to be used in anterior cruciate ligament (ACL) reconstruction surgery, and as a replacement for grafts that present the risk of donor site morbidity and graft failure. To manufacture Biolig, a continuous PCL yarn is electrospun from solution (9% PCL-hexafluoroisopropanol (HFIP) solution), stretched, bundled to create multifilaments, braided, and sterilized with ethylene oxide. Top down, the structural hierarchy of

Biolig, shown in Fig. 1.2, proceeds as follows: braid (made from 24 multifilaments) > multifilament (made from 9 filaments) > filament > fiber > polymer chain.

The purpose of stretching the PCL yarn is twofold: i) to prevent the final braid from further plastic deformation during patient recovery; and ii) to align fibers within the filaments to mimic ligament morphology. Fiber alignment has been shown to improve net mechanical properties of the overall ES specimen, increasing strength and stiffness when the fibers are aligned parallel to the loading direction (*14*). In general, ES fibers can be stretched during electospinning (if using aligning collector geometry) or after, the latter of which is the case for Biolig. Stretching can increase anisotropy on both a macroscopic and molecular level. Macroscopically, the stretch force converts randomly deposited fibers into a highly aligned morphology. Microscopically, stretching can affect crystal microstructure, including crystal orientation, crystallinity (X_c), and crystal transformation.

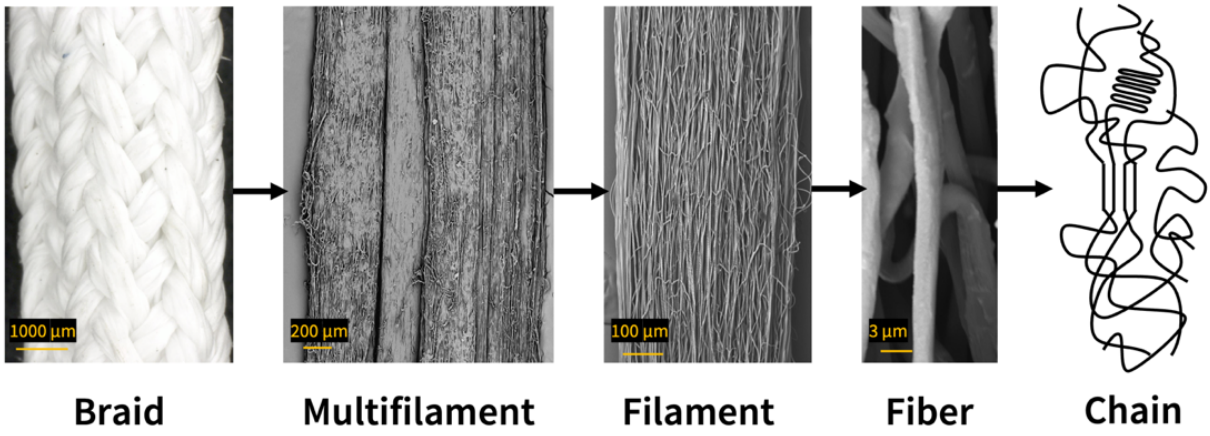

Fig. 1.2 Hierarchical structure of Biolig, progressing left to right from largest to smallest dimension from left to right. Leftmost image courtesy of Dr. Pierre-Alexis Mouthuy.

In 2021, Mouthuy characterized early-stage development of PCL yarns in twisted and woven (i.e., not braided) forms (*13*). Specifically, through processing, the average diameter of the microfibers exhibited a decrease from a single stretched filament (2.9 μm) to cabled yarn (1.9 μm) to woven fabric (1.6 μm). Stretching (manually at a drawing ratio of 1:7) reduced the average width of filaments from 776 to 517 μm and decreased fiber diameter from 2.9 ± 0.6 to 1.9 ± 0.4 μm (*13*). The tensile strength of the woven ES yarn was found to be suitable for ACL reconstruction surgery. The stretched yarns possessed a higher maximum stress (150 MPa) and higher Young's modulus (500 MPa) when compared to literature values for other PCL yarns (3-40 MPa and 5-70 MPa, respectively). The superior performance of Mouthuy's yarns can be explained by the unique dynamic wire collector design employed in the study, which created a densely connected fibrous mesh. Biological characterization showed that the ES sutures were non-cytotoxic and better able to promote an elongated cell morphology compared to the control non-ES suture.

1.2.2 Microstructural Properties

In general, ES yarns exhibit several structural hierarchies, from crystal unit cells at the atomic scale, polymer chain folding at the molecular scale, and fiber bundles at the micro-scale. The interplay among these hierarchies leads to complicated structure-property relationships, as the macroscopic properties of the yarn are not simply the sum of the properties exhibited at each level (*15*).

For biomedical applications, it is of significant value to investigate chain-level supramolecular arrangements, both in terms of crystalline microstructure and underlying polymer physics, to help predict and optimize their degradative and mechanical properties. As their name suggests,

semicrystalline polymers possess both crystalline and amorphous characters. Amorphous regions tend to degrade faster than the denser crystalline regions, which is relevant in predicting a yarn's tissue-regenerative functionality (*16*, *17*). Additionally, the stretching of fibers, both during and after electrospinning, is said to improve mechanical properties by increasing X_c and crystal alignment to the stretch axis (*18–22*). These parameters can directly affect Young's modulus and, in subsequently usage, cell differentiation (*23*, *24*). In ES fibers, the spinning elongation process can align polymer chains with the fiber axis, resulting in crystal orientation (*25*).

Studies have found that the mechanical properties of various ES fibers change significantly when their diameters fall below a critical threshold (*26*). For example, an abrupt upwards shift in the tensile strength of ES PCL fibers was observed when their diameter fell below ~700 nm (*27*). Similarly, in polystyrene nanofibers, an abrupt increase in Young's modulus was recorded as the diameter decreased to ~500 nm (*28*). Wong et al. compared the tensile properties of PCL in bulk solid and compressed fiber forms with the same overall sample size dimensions, finding that the fibrous samples had notably superior mechanical properties (*27*). For these various materials, the abrupt shift in mechanical properties of their narrower fibers may have been due to enhanced alignment of both the amorphous and crystalline regions. Other studies have shown that both molecular orientation and X_c increased with decreasing fiber diameter (*29*, *30*). However, neither the gradual increase in molecular orientation and X_c, nor changes in surface tension, explain the observed abrupt mechanical changes (*30*). Crystal morphology may be the reason for these changes, but there is a lack of consensus in the literature on models of semicrystalline deformation to validate this hypothesis. This study aims to tackle this gap in understanding as to how chain architectures evolve in stretched fibers.

1.3 Material of Interest: Polycaprolactone (PCL)

PCL is a polymer with a wide range of biomedical applications such tissue engineering and drug delivery. Such broad usage is due largely to the biocompatibility, biodegradability, and elasticity of PCL, as well as the Food and Drug Administration approval of PCL for physiological usage (*3*, *25*). Structurally, PCL is a linear aliphatic polyester with repeating (O — $(CH_2)_5$ — CO) units (Fig. 1.3) (*31*). It has an orthorhombic unit cell with lattice parameters a = 7.496 Å, b = 4.974 Å, c = 17.297 Å and a $P2_12_12_1$ space group (*31–33*). The unit cell contains a total of two chains in opposite orientation, depicted in Fig. 1.4, with twists near the ester linkage and a c-axis that coincides with the chain axis (*25*).

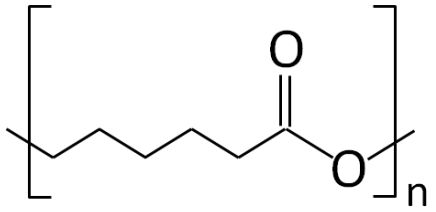

Fig. 1.3 Chemical structure of PCL.

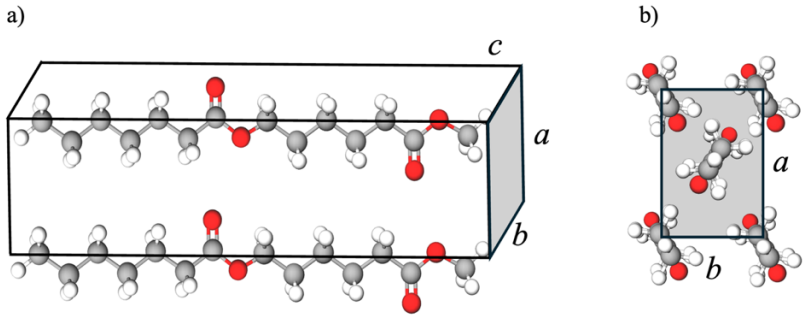

Fig. 1.4 Orthorhombic PCL unit cell viewed along a) b-axis and b) c-axis. Only chains passing through the frontmost face of the unit cell are depicted for viewing simplicity. Figure adapted from Kossack et al. (*34*).

PCL is a semicrystalline thermoplastic polymer that degrades slowly via hydrolytic cleavage of its ester bonds (*7*, *17*). Significant literature exists detailing the mechanisms of PCL degradation (*3*, *22*, *35*). PCL is hydrophobic and takes a few months to several years to degrade depending on a variety of factors including Mw, X_c, the surrounding environment, and morphology (*36*). Hydrolysis is initiated by water absorption into the material bulk (*37*). In addition to affecting the mechanical integrity of PCL during degradation, water uptake is particularly important to consider when using ES microfibers for tissue engineering. Enlarged fiber diameters from swelling can reduce the porosity needed for cell infiltration and growth. Literature reports that ES PCL swells more than bulk PCL. Bulk PCL was found to swell only 5-7% of its initial weight after soaking in artificial saliva for 8 weeks (*38*). For ES PCL, depending on the study, swelling increased the sample mass by 35.5% (*39*), 160% (*17*), and 200% (*3*) its original mass after soaking 10 days in solution. In these three cited studies, the largest increase in solution uptake was most often observed to take place during the first measurement, after which subsequent measurements showed a plateau in solution uptake. It is possible that these studies measured solution mass that adsorbed onto the sample surface and remained trapped between fibers, rather than solution absorbed into the fiber core.

PCL has a melting temperature (T_m) of 60 °C and glass transition temperature (T_g) of -60 °C (*31*). T_m refers to the liquification of polymer crystals, whereas T_g refers to the temperature at which amorphous backbone conformational changes can take place, reversibly transitioning the amorphous phase from brittle to highly viscous or rubber-elastic. PCL's low T_g allows for ease of plastic deformation at room temperature (RT, 20 °C). This also means that, at RT storage conditions, it is possible for PCL fibers to gradually anneal together, as well as increase in X_c

(*40*). However, a study on PCL yarns aged 27 months found that their tensile properties remained consistent (*25*), so ambient secondary crystallization is likely insignificant for PCL from a mechanical standpoint.

1.4 Polymer Crystals

1.4.1 Crystallization

Because polymer crystals are integral to semicrystalline microstructure, which is the focus of this thesis, this section discusses basic principles of crystallization.

Polymer crystals are one length scale above the unit cell, and crystal aggregates such as spherulites are a length scale above polymer crystals (*15*). Crystallization kinetics follows the Avrami equation:

$$1 - X_c = \mathrm{e}^{-\mathrm{K}\mathrm{t}^{\mathrm{n}}}$$

where t = time, n = constant depending on the process of nucleation (between 1 and 4), and K = constant (*41*). After polymers crystallize, secondary crystallization may occur, which can cause the X_c of the material to increase slowly over time. The degree of such secondary crystallization is inversely related to the extent of primary crystallization (*41*).

Polymer crystallization occurs in two main steps. First, a nucleation barrier must be overcome to form a stable nucleus (*42*). This is the case for *homogeneous* nucleation, where nuclei are generated spontaneously, as well as *heterogeneous* nucleation, where an existing nucleus is required to initiate crystallization in a liquid environment. Of these two, the nucleation barrier is smaller for heterogeneous nucleation (*15*). Second, crystalline growth occurs from the nucleus

interface and long-range order develops. Crystallization occurs between the polymer's T_g and T_m. At T_m, the change in volume free energy (G_v) is described by:

$$\Delta G_v = \Delta H_v - T_m \Delta S_v = 0$$

so, T_m can be written as $T_m = \frac{\Delta H_v}{\Delta S_v}$. PCL, for instance, has a very flexible backbone chain that is mostly sp3 hybridized. This leads to a high number of possible microstates in the melted state, which means a greater entropy change occurs upon melting, which ultimately leads to a low T_m of 60 °C. T_g tends to increase with T_m ($T_g \cong (0.5{\sim}0.8)T_m$) (*43*), and is affected by bond stiffness, interchain bonding, branching, and molecular weight (Mw). Studies have found that X_c can raise T_g due to the restrictive effect that crystalline regions have on amorphous chain mobility (*42*, *44*, *45*).

For crystallization to occur spontaneously, the change in Gibbs free energy (ΔG) must be negative. Although crystallization is entropically unfavorable (i.e., it has a negative ΔS because the crystalline phase has fewer possible microstates), exothermic bond formation (i.e., negative ΔH) can compensate for the loss in entropy, particularly at low temperatures. Just below T_m, few nuclei form, causing the growth of large crystals, whereas closer to T_g, many nuclei develop, causing the growth of many smaller crystals. Below T_g, the segmental motion of polymer chains stalls, halting crystal growth. Although crystallization is favorable when ΔG is negative, 100% X_c is rare in semicrystalline polymers due to kinetic barriers and structural constraints. For one, steric hindrances make it difficult for chains to pack in an ordered fashion. Furthermore, high Mw polymers exhibit an increased propensity for chain entanglement, which impedes crystallization (*15*, *23*).

Stretching can facilitate crystallization by reducing the number of possible microstates available to polymer chains, thereby decreasing the configurational entropy loss associated with the transition from an amorphous to crystalline state (*46*). Crystallization occurs when $T\Delta S < \Delta H$, so a lower pre-crystallization entropy (from chain elongation) allows crystallization to occur at higher temperatures than under quiescent conditions (*47*). In other words, applying strain at a given temperature enhances the degree of supercooling, which is the extent to which a melt's temperature is lowered below its T_m without crystallizing. While the thermal-induced mobility of chains is consistent at a given temperature irrespective of the applied strain, the thermodynamic drive to crystallize increases due to greater supercooling when stretched.

Most generally, a two-phase fringed-micelle model is used to describe semicrystalline polymers, where relatively perfect crystals are connected by tie chains that traverse an intermediate amorphous matrix. It is difficult to define a definite border between crystalline and non-crystalline regions, as amorphous regions may also exhibit some level of order when extended (*15*), and crystals may have defects where lattice symmetry is disrupted (*41*, *48*). The two-phase model is a simplification but nonetheless serves as a theoretical basis I used to identify general microstructural trends in my material of interest.

1.4.2 Morphologies

Throughout the history of polymer physics, various morphological models of polymer crystals have been proposed (*41*). The first model (Fig. 1.5a), posited by Hermann Staudinger in the 1930s, assumed that polymeric chains had a relatively long, extended confirmation. Next, the Hess-Kiessig model (Fig. 1.5b) depicted long periodicity (discovered using low angle X-ray scattering) and fibrillar character. The Bonart-Hosemann model (Fig. 1.5c) built upon this by

adding chain folds in the crystalline and amorphous regions, as well as relaxed tie chains in the latter region. Unfortunately, these models are incompatible with the high fracture strain and low tensile strength of actual polymer fibers.

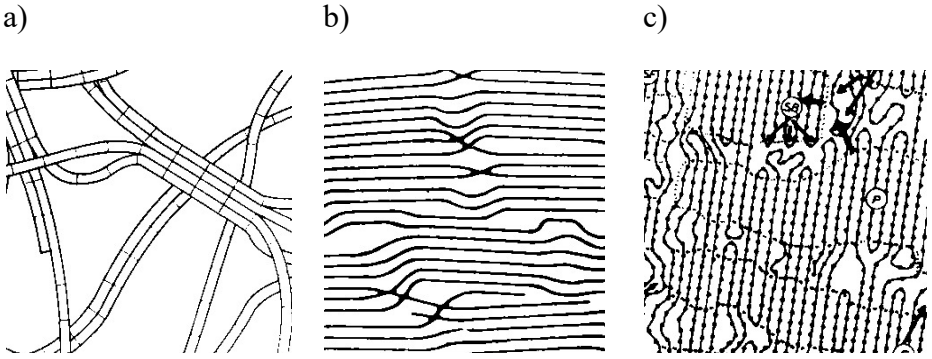

Fig. 1.5 Early models of polymer crystals: a) Staudinger, b) Hess-Kiessig, c) Bonart-Hosemann **(*41*)**.

Thermodynamic considerations predict that linear polymers, such as PCL, present two maxima of morphological stability, and these predications have been confirmed experimentally for chain-extended crystals (CEC) and chain-folded crystals (CFC) (Fig. 1.6) (*49*, *50*). These structures are analogous to 'topomers' from the field of organic chemistry, where molecules of the same composition differ in atomic arrangements without breaking bonds. CFC consist of lamellar blocks, which are packed, folded chains aligned parallel to one another. (In my work, 'lamellae' is used interchangeably with CFC.) Folded lamellae grow in the crystal plane and tend not to thicken beyond their dimension at initial nucleation. CFC thickness is often on the order of 10 nm and depends on the positive energy of the two folded basal surfaces, as well as kinetics (i.e., supersaturation and supercooling leading to thinner crystals) (*43*). On the other hand, CEC consist of straight chains without folds. Generally, polymer crystals that are thicker than 200 nm are considered CEC (*51*). This thickness is based on the definition of a polymer molecule possessing a Mw ≥ 20,000, where surface effects of folds and chain ends become negligible (*52*).

Polymer crystal morphologies differ depending on the chemical, thermal, and mechanical environment in which crystallization takes place (*50*, *53*, *54*).

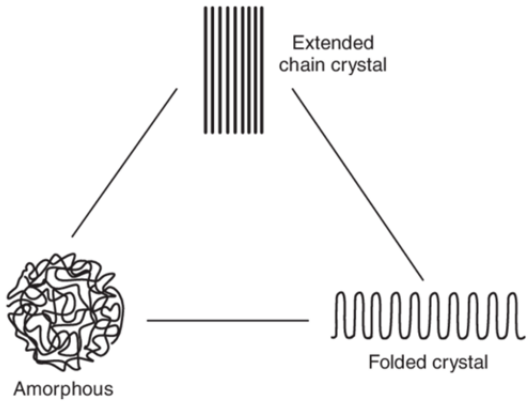

Fig. 1.6 Phases of polymer chains **(*55*)**.

1.5 New Science

While existing studies have explored the effect of electrospinning on the X_c of PCL fibers, no studies have investigated how Biolig's unique electrospinning set-up and post-processing affect the material's polymeric architecture, particularly the stretching of its microfibrous filaments. Understanding the evolution of a material through various processing and mechanical environments can reveal valuable insights into its underlying structure.

This thesis project is a PCL-based case study into the crystal microstructure of ES microfibers subjected to varying degrees of stretching. This work integrated microscopy, thermal, diffractive, and mechanical analyses to assess the impact of post-drawing, or stretching after spinning, on fiber diameter and alignment, as well as crystal morphology, volume, orientation, and overall X_c. The microfibers were characterized using micro-computed tomography (μCT), scanning electron microscopy (SEM), differential scanning calorimetry (DSC), X-ray diffraction (1D and 2D XRD), and dynamic mechanical thermal analysis (DMTA). By synthesizing this study's results

with those of existing literature, a polymer physics-based theoretical framework was developed to describe the evolution of this material's microstructure. This framework can help future researchers develop more accurate models of Biolig to optimize its manufacturing.

2. Experimental Methods

2.1 Material Preparation

To prepare the ES filaments, poly-(ε-caprolactone) (PCL) pellets (Ashland Specialties Ireland, Laboratory A, Synergy Centre, Institute of Technology Tallaght, Ireland) were dissolved in 1,1,1,3,3,3-HFIP (Apollo Scientific Ltd, Cheshire, UK) to a weight-to-volume concentration of 10% PCL. The solution was agitated at RT at 21 rpm (Stuart Roller Mixer SRT9D, Staffordshire, UK) for 1 week to ensure complete polymer dissolution. To form a continuous fibrous filament, a unique electrospinning set-up using a dynamic wire collector was used (Fig. 1.1). A detailed description of this electrospinning technique developed by Mouthuy et al. is referenced (*56*). Dr. Meng Liang performed the electrospinning of the Biolig samples.

Unless otherwise noted, for all experiments, PCL with Mw = 190,000 g/mol was investigated (as measured by gel permeation chromatography) and triplicates of each sample and their standard deviation (SD) were measured. Filaments were stored in a 0 °C freezer prior to their usage in experiments to limit ambient material changes.

To measure how the degree of stretch affects polymer crystal properties, filaments were stretched manually to varying degrees at RT after electrospinning. To ensure uniform stretching, samples

were stretched in 1 cm segments, as drawing of longer segments resulted in inhomogeneous extension. The maximum draw ratio reached was 1:6.

2.2 Stretch Temperature

To examine the effects of heat dissipation during stretching, filaments were stretched 1:3 and 1:5 at RT and in ice water ('cold'; 0 °C). Because filaments reached a maximum stretch of 1:5 in cold but 1:6 at RT, an additional set of so-called 'dual thermal' filaments were stretched using two thermal conditions: first stretched 1:5 in cold, then finished to a stretch of 1:6 in RT.

2.3 Thermal Contraction

To determine whether filaments contracted when heated, 1:1 and 1:6 filaments were placed on a 100 °C hot plate and observed. Contraction could change DSC sample-pan contact during heating ramp up and also reveals microstructural tension within the fibers.

2.4 Water Uptake

To determine the extent of filament swelling in solution, filaments were soaked in phosphate buffer solution for 40 days and weighed periodically after being patted dry.

2.5 Microfiber Morphology

Scanning electron microscopy (SEM) imaging was used to investigate the architectural changes that occurred when the filament was stretched, specifically examining the degree of fiber orientation and changes in diameter. Micro-computed tomography (μCT), in contrast to SEM, offered the capability to non-destructively capture high-resolution trans-axial slices of the sample. μCT complimented SEM by enabling visualization of the filament's interior, whereas SEM was restricted to finer examination of the surface.

2.5.1 Scanning Electron Microscopy (SEM)

The diameter and alignment of fibers within filaments stretched to various degrees (1:1-1:6) were observed using SEM (Hitachi TM3000). To obtain cross-sectional images, filaments were immersed in liquid nitrogen then immediately snapped. In addition to filaments, a multifilament (composed of a bundle of 9 filaments) stored at RT for over 5 months was imaged to observe any longitudinal changes.

Prior to SEM imaging, samples were gold-sputtered to mitigate the effects of charging on image contrast. 2D image analysis was carried out using ImageJ. Anisotropy was quantified using coherency values from the OrientationJ plugin, with calculations based on a structure tensor method where the first eigenvector gives the dominant orientation of the image (*57*). A coherency of 0 corresponded with a completely isotropic image, and a value of 1 corresponded with a completely anisotropic image exhibiting only one orientation (*14*). Images with 500x and 3000x magnification were used for coherence and diameter measurements, respectively.

2.5.2 Micro-Computed Tomography (µCT)

Filaments were scanned in a Zeiss Xradia 510 µCT at 70 kV with an imaging voxel size of 0.7 um. The samples were placed in a tube mounted vertically in the scanner. 1:1 and 1:6 filaments were imaged. 3D visualization was performed on Meshlab, using twice-downsized images due to the large original file sizes that could not be rendered. Coherence was measured using the OrientationJ plugin in Fiji on these reconstructed images from various depths within the filament, including the surface, center, and midpoint between these latter two (i.e., half of the radius). This analysis aimed to determine if the fibers were stretched and aligned uniformly within the filament's interior and exterior. Georgy Grishchenko obtained the uCT scans.

2.6 Crystallization Analyses

2.6.1 Thermal Analysis (DSC)

Differential Scanning Calorimetry (DSC; Perkin Elmer Diamond) was used to obtain heat flow profiles and X_c from samples measured across a thermal range of 0-80 °C under a nitrogen atmosphere. A heating rate of 10 °C/min was used unless otherwise indicated. Between two heating cycles, a faster cooling rate of 100 °C/min was used. DSC curve characterization and integration was performed OriginPro software. Fig. 2.1 depicts how OriginPro was used to fit Gaussians to the endotherms. All DSC curves presented in this work were shifted vertically for ease of visual representation.

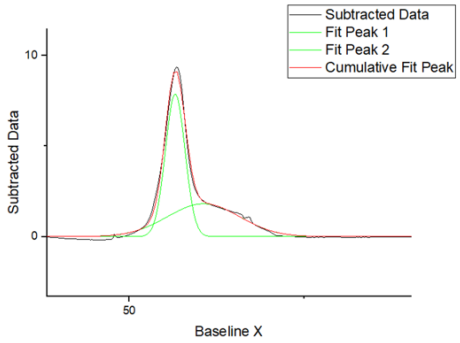

Fig. 2.1 Example of double Gaussian fitting on 190k 1:6 stretched sample using OriginPro software.

Unlike a metallic sample, melting occurs over a broader temperature range in semicrystalline polymeric samples due to a distribution of Mw and crystals. The shape of DSC curves was compared across samples to elucidate the evolution of crystal stability through processing. In general, a material's T_m correlates with the energy state of the solid, so a higher T_m was used as an indicator of more stable crystals.

To determine X_c from DSC, the following equation was used (*16*):

$$X_c = \frac{\int_0^\infty (\frac{dH}{dt})dt}{\Delta H_{100\%}} \times 100\%$$

where H = melting enthalpy of the sample per unit mass, t = time, and $\Delta H_{100\%}$ = enthalpy of a 100% crystalline sample (139.5 J/g) (*31*). H was calculated by integrating the area (A) of the melting peak, which represented heat flow as a function of temperature (T):

$$H = \frac{60 * A}{\frac{dT}{dt} * m}$$

where dT/dt = heating rate, and m = sample mass. This calculation was done using the first heating cycle (Heating 1), which reflected the processing history of the sample, unlike the second heating cycle (Heating 2) where the cooling between cycles subjected the material to different crystallization conditions compared to electrospinning and post-processing.

A variety of DSC experiments were performed, modulating the following variables: sample-pan contact (see Section 2.6.1.1), heating rate (see Section 2.6.1.2), sample type/degree of stretch (see Section 2.1), stretch temperature (see Section 2.2), and Mw (110k, 190k). The first two variables were investigated to determine whether changing instrumental measurement conditions affected subsequent DSC curves, so as not to mix up instrumental artifacts with innate polymer properties.

2.6.1.1 Sample-Pan Contact

To assess the impact of sample contact with the pan base on the DSC curve, experiments were conducted using pellet and 1:6 filaments with either complete or incomplete contact. For the pellets with incomplete contact, they were cut irregularly, rather than flat like samples with complete contact. For the filaments, incomplete contact was achieved by rolling them into a cylindrical shape, ensuring only the base of the cylinder touched the pan. In contrast, for

complete contact, the filaments were cut into short segments to fit the pan without folding and were compressed against the base to maximize contact.

2.6.1.2 Heating Rate

While the standard heating rate for DSC analysis is typically 10 °C/min, a range of heating rates including 2, 5, 10, and 25 °C/min were applied to the pellet, unstretched, and stretched (1:6) filaments. This also allowed for inferences to be made on the metastability of crystal structures within the samples.

2.6.2 Diffractive Analysis (XRD)

2.6.2.1 Crystallinity and Crystal Size (1D)

In addition to DSC, 1D wide angle X-ray diffraction (XRD) was used to determine X_c, as well as crystal size. Because X-rays have wavelengths of comparable length to crystallographic molecular dimensions, the diffraction of such rays can be used to determine the interatomic distance d between specific crystal planes, using Bragg's Law:

$$2d \sin \theta = n\lambda$$

where θ = angle between incident X-ray beam and diffracting crystal plane, $\lambda =$ beam wavelength, and n = positive integer.

The XRD profile was recorded using CuKα radiation (λ = 1.5419 Å) operated at 40 kV and 15 mA on the Rigaku MiniFlex XRD in the range of 2θ = 2-30° at a scanning speed of 1.5°/min. Filaments were positioned either parallel (||) or perpendicular (⊥) to the X-ray beam within the holder, as depicted in Fig. 2.2. These orientations did not show any differences in their traces of intensity as a function of 2θ, as shown in Fig. 2.3, which was expected for samples containing crystal planes with in-plane rotational symmetry. After background signal subtraction and

normalization of maximum intensity to a value of 1, Origin software was used to apply a Gaussian fit and analyze the peaks. Only the (111) peak at 22°, one of PCL's three characteristic planes of diffraction, was fixed with a full width at half-maximum (FWHM) of 0.98, with all other parameters free to change. The (111) peak was fixed because it was obscured by the amorphous halo in stretched samples. The FWHM value was determined from peak fitting of unstretched samples where the (111) peak was most visible.

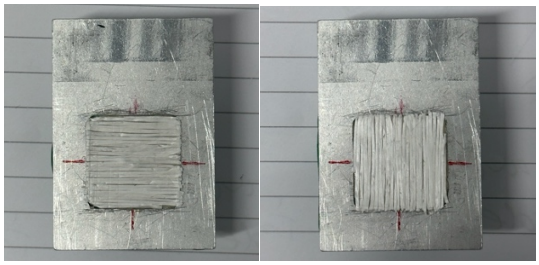

Fig. 2.2 Filaments in sample holder (Mw = 110k; 1:6), with fiber axis oriented parallel (left) and perpendicular (right) to beam incidence.

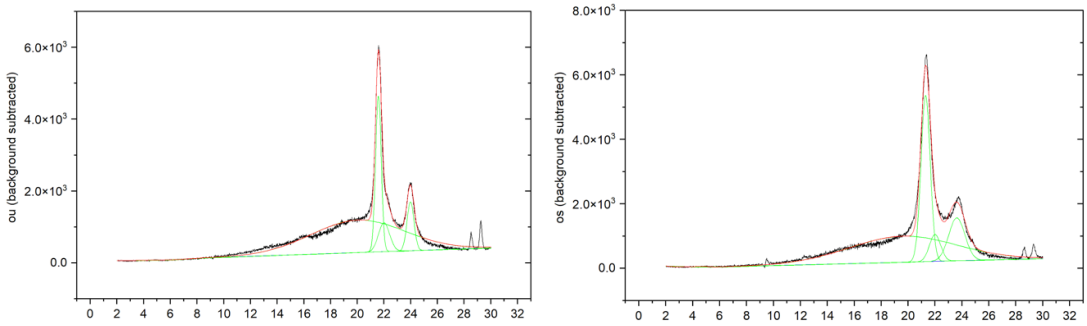

Fig. 2.3 Gaussian curve fitting example on 1:1 (left) and 1:6 (right) 110k filaments oriented perpendicular to beam. Note: Two small peaks on the right of the profile are background artifacts.

X_c was calculated using the following equation:

$$X_c = Ac/(Ac + Aa)$$

where A_c = crystalline peak area and A_a = amorphous halo area.

Crystal size L_{hkl} was calculated for each characteristic peak using the Scherrer equation:

$$\langle L \rangle_{hkl} = \frac{K\lambda}{B \cos\theta} \text{ (L<200 nm)}$$

where K = a geometric constant of 0.94, λ = X-ray wavelength, B = FWHM, and θ = Bragg angle, the latter two variables both in radians.

Lattice parameters for PCL's orthorhombic unit cell was calculated using the following expression:

$$\frac{1}{d_{hkl}^2} = \frac{h^2}{a^2} + \frac{k^2}{b^2} + \frac{l^2}{c^2}$$

where *a*, *b*, *c* = lattice parameters, d = d-spacing, and h, k, l = Miller indices.

2.6.2.2 Crystal Orientation (2D)

To determine the degree of crystal alignment in filaments, quadrant azimuthal profiles were obtained via 2D grazing incidence X-ray scattering for 1:1 and 1:6 filaments. A Rigaku Smartlab X-ray diffractometer was employed, equipped with a PhotonMax 9 kW rotating anode source using CuKα radiation and a HyPix-3000 2D semiconductor detector at a 150 mm sample-to-detector distance. Incident end optics included a 5 mm X-ray spot size height-limiting slit, parallel beam slit, and 1.0° in-plane parallel slit collimator. Out-of-plane (OOP) diffraction was measured with an asymmetric grazing incidence of 0.2° 2θ in 0.04° steps from 0 to 30° 2θ at a rate of 5° 2θ/min. In-plane (IP) diffraction was captured between -2 to 26° 2θ with a detector offset of 12° 2θ. Background azimuthal intensities near the 2θ of interest were subtracted after correcting for the OOP meridian intensity. Filaments were orientated either || or ⊥ to the incident X-ray beam. Ryan Schofield acquired these 2D XRD images.

Each concentric Debye-Scherrer ring in the diffraction pattern corresponded with a specific 2θ, or crystallographic plane. The Bragg condition, relating to the angle between the normal of the crystal plane and incident ray, must have been satisfied for diffraction to occur. The intensities of azimuths at each characteristic 2θ were measured as a function of azimuthal angle β. The azimuthal angle measured rotation around the normal to the sample surface (*58*), as illustrated in Fig. 2.4. The angle of the crystal planes with respect to the substrate dictated the diffraction orientation along the azimuthal OOP-to-IP arc.

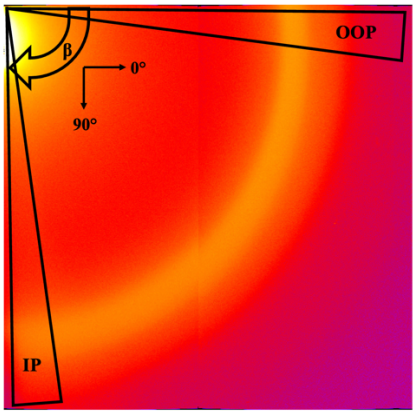

Fig. 2.4 Schematic of in-plane (IP) and out-of-plane (OOP) orientations relative to sample surface face, as well as azimuthal angle β with 0° and 90° direction labeled.

Herman's orientation factor (f) is a scalar that was used to quantify orientation within a system:

$$f = \frac{3\langle \cos^2 \phi \rangle - 1}{2}$$

where $\langle \cos^2 \phi \rangle$ = average cosine square of angle ϕ between an individual specimen's orientation and the reference axis. f = 0 when the specimen was isotropic, 1 when the specimen was perfectly aligned to and parallel with the reference axis, and -0.5 when the specimen was perpendicular to the reference axis. The reference direction used in this study was the filament

(i.e., stretch) axis, which was also the crystal's c-axis along (00l) if the chains comprising the crystal were aligned to the filament.

2D XRD measured overall crystal orientation ($f_{overall}$), which was a convolution of the orientation of crystals in an individual fiber ($f_{crystal}$), of fibers within a filament (f_{fiber}), and of filaments within the XRD sample holder with respect to the intended || or ⊥ placement ($f_{filament}$) (*59*):

$$f_{overall} = f_{crystal} * f_{fiber} * f_{filament}$$

$f_{filament}$ was assigned a value of 1, as the filaments were carefully aligned to be practically parallel to one another. To calculate $f_{overall}$, $\langle \cos^2 \phi \rangle_{00l}$ was first determined using Wilchinsky's method for an orthorhombic unit cell (*60–64*). In the absence of an (00l) diffraction peak in PCL, no planes existed that displayed c-axis orientation directly (*64*). Instead, (110) and (200) crystallographic planes were used to determine backbone chain alignment, which corresponds with the crystal's c-axis alignment to the fiber axis:

$$\langle \cos^2 \phi \rangle_{00l} = 1 - \frac{(1 - 2\sin^2 \rho_{200})\langle \cos^2 \phi \rangle_{110} - (1 - 2\sin^2 \rho_{110})\langle \cos^2 \phi \rangle_{200}}{\sin^2 \rho_{110} - \sin^2 \rho_{200}}$$

where ρ = angle between the (0k0) index (b-axis) and normal of the (hk0) plane. As calculated by Jordan, PCL's lattice parameters were used to calculate ρ trigonometrically, which enumerated the above equation to (*65*):

$$\langle \cos^2 \phi \rangle_{00l} = 1 - 1.441\langle \cos^2 \phi \rangle_{110} - 0.559\langle \cos^2 \phi \rangle_{200}$$

To calculate $\langle \cos^2 \phi \rangle_{110}$ and $\langle \cos^2 \phi \rangle_{200}$, the measured diffraction peak intensity $I(\beta)$ was first converted to radial $I(\phi)$ using the following spherical trigonometric relationship (*66*):

$$\cos \phi = \cos \beta \cos \theta$$

where θ = Bragg angle ((hkl) diffraction peak located at 2θ) and β = angle from the OOP meridian. $I(\phi)$ represented the relative amount of crystalline material having plane normals in

the ϕ direction. The intensity was assumed to be entirely a result of crystalline scattering, although there may be amorphous contributions (*60*, *67*). The average cosine square for (hk0) was calculated using the following integration (*68*, *69*):

$$\langle \cos^2 \phi \rangle_{hk0} = \frac{\int_0^{\frac{\pi}{2}} I(\phi) \cos^2 \phi \sin \phi \, d\phi}{\int_0^{\frac{\pi}{2}} I(\phi) \sin \phi \, d\phi}$$

The corresponding $\langle \cos^2 \phi \rangle$ values for (110) and (200) were plugged into the $\langle \cos^2 \phi \rangle_{00l}$ expression. Then, $\langle \cos^2 \phi \rangle_{00l}$ was plugged into the equation for Herman's orientation factor to obtain $f_{overall}$.

f_{fiber} was also determined to account for the misorientation of fibers from the dominant filament axis (*31*, *53*, *68*, *69*). To do so, the angular distribution ϕ of fibers from the dominant direction was measured using the OrientationJ ImageJ plugin on SEM images at 500x magnification. An assumption was made that the dominant orientation in SEM corresponded to the filament axis.

As described by Wang et al., the orientation of crystals in a single fiber $f_{crystal}$ could thus be approximated by dividing the XRD-derived $f_{overall}$ by the SEM-derived f_{fiber} (*59*):

$$f_{crystal} = \frac{f_{overall}}{f_{fiber}}$$

2.7 Viscoelasticity (DMTA)

Dynamic mechanical thermal analysis (DMTA) was used to determine how the filaments' moduli and T_g changed as a function of temperature and stretch. A DMA800 (Perkin Elmer) equipped with a nitrogen cooling chamber was used, applying a displacement of 0.05 mm in tension at a frequency of 1 Hz. Measurements were performed at a temperature range of -100 to

40 °C at a heating rate of 10 °C/min. Filaments with stretch ratios 1:1, 1:3 and 1:6 were examined. To prevent the samples from slipping out of the DMTA grips, filament ends were cast in Araldite epoxy.

The storage modulus G' (i.e., real; elastic) and loss modulus G'' (i.e., imaginary; viscous) were used to calculate $tan(\delta)$, also known as the damping factor. $tan(\delta)$ represents the dissipation of energy in a cyclically deformed material (*70*):

$$tan(\delta) = \frac{G''}{G'}$$

G' represented the recoverable energy that is stored in a deformed material, whereas G'' represented the non-recoverable energy dissipated as heat when deformed. Changes in moduli and $tan(\delta)$ with temperature indicate important molecular transitions in the material, such as T_g and T_m onset.

The Perkin Elmer software required a diameter input to record moduli. µCT images were used to estimate diameter. Because the samples tested in the DMTA were different from those imaged in µCT, this estimation introduced slight inaccuracy; this could only affect the amplitude of the calculated moduli, not measured T_g nor $tan(\delta)$.

To identify T_g, three discrete points on the DMTA curve could theoretically be used, marked in grey in Fig. 2.5: the peak of G'', the peak of $tan(\delta)$, or the onset of decrease of G' (*71*). In my study, T_g was determined using the first two points. The onset of decrease in G' could not be identified, as the minimum temperature range of my measurements did not extend low enough to capture this transition.

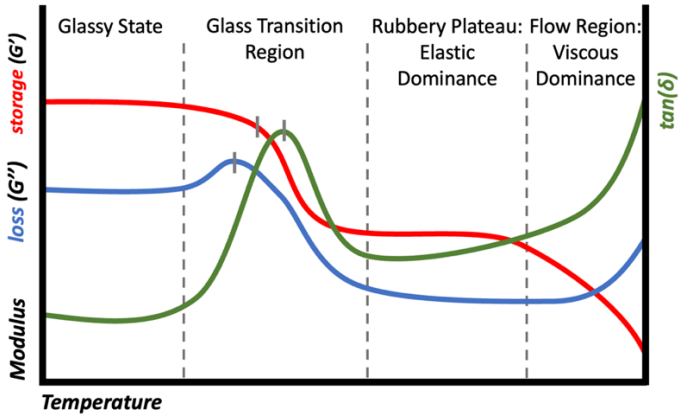

Fig. 2.5 Theoretical DMTA curve for typical thermoplastic polymer. In real experiments, it is not possible to measure the entirety of the right-most flow region, as $\boldsymbol{T_m}$ is contained within this region and the sample will melt out of the machine clamps.

3. Results

This section begins by presenting results at the filament scale, followed by findings at the finer chain level.

3.1 Thermal Contraction

Fig. 3.1 presents photographs of 1:1 and 1:6 filaments on a 100 °C hot plate. Within 2 seconds of initial contact, 1:6 quickly contracted, whereas no contraction was observed during melting of 1:1.

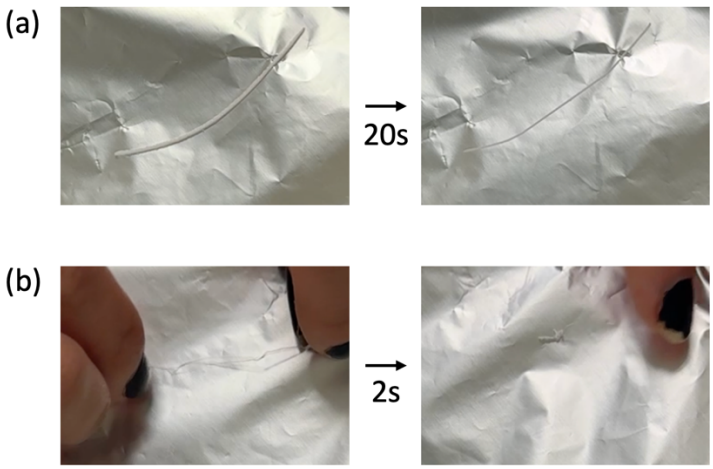

Fig. 3.1 Photographs of (a) unstretched and (b) 1:6 stretched filaments placed on a 100 °C hotplate covered with aluminum foil.

3.2 Water Uptake

After soaking filaments for 4 days, the samples returned to their original mass within 7 minutes after being removed from solution (Fig. 3.2). This indicates the post-soak mass measurements from literature (discussed in Section 1.3) likely captured remaining solution on fiber surfaces rather than true swelling from absorption. The hydrophobic nature of PCL results in slow solution uptake, consistent with its characteristically slow degradation rate.

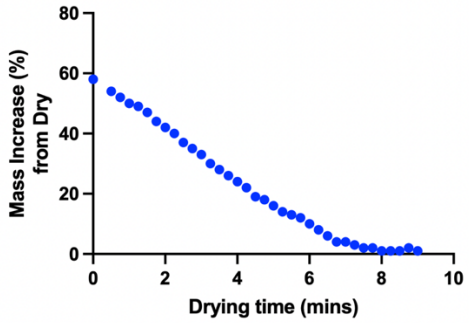

Fig. 3.2 Effect of drying time on stretched filament mass that had been soaked for 4 days.

3.3 Microfiber Morphology

Fig. 3.3 contains SEM micrographs of microscale segments of fibrous filaments stretched to varying degrees. From initiation of stretching, fibers exhibited inhomogeneous stretching and necking, characterized by narrow, elongated regions interspersed with thicker segments. Necking is a manifestation of plastic deformation in which a localized reduction in cross-sectional area occurs under tensile stress. As depicted in Fig. 3.4, at stretch ratios of 1:4 and beyond, noticeable fiber fraying and breakage occurred. Fig. 3.5 depicts bifurcation of fibers, revealing that some fibers originated and split off from one larger fiber.

3.3.1 Diameter

As stretch ratio increased, individual fibers appeared to melt together horizontally and form a large, coalesced fibrous ribbon, as observed in Fig. 3.3's SEM micrographs. For example, the 1:6 3000x micrograph in Fig. 3.3f shows coalescence of neighboring fibers. Two types of dimensional measurements were taken from the SEM micrographs: one that considered only individual fiber diameters and another that also considered the width of coalesced ribbons, or 'wide' fibers. Because fibers coalesce into relatively flat ribbons rather than cylindrical bundles, the measurements of the wide fibers represented isotropic widths, not diameters. Additionally, if the wide fiber was not perfectly normal to the SEM electron beam, the measured width may have represented an angled projection of the ribbon, potentially leading to an underestimation of the true width. Both the average individual-only and wide-inclusive fiber dimensions are plotted in Fig. 3.6 as a function of stretching.

If uniaxial stretching along the filament axis directly corresponded to fiber narrowing, the fiber diameter would change accordingly:

$$d = D/\sqrt{n}$$

where d = expected diameter of the 1:n stretched fiber, D = diameter of the unstretched fiber, and n = scalar multiple of original length (1:n). This expected diameter d is also plotted in Fig. 3.6, with the average individual 1:1 diameter used for D.

Fig. 3.6 shows that the individual fibers closely adhered to the expected outcome if filament stretching corresponded directly to fiber narrowing. Considering that 1:1 filaments consisted of randomly aligned fibers, it could be hypothesized that stretching initially aligned the fibers before straining them. This sequence — from aligning to straining — would likely result in a greater average individual diameter than the expected diameter d at lower stretch ratios n, whereas at larger n the average individual diameter would converge towards d as plastic deformation sets in. However, Fig. 3.6 shows that even from a low n (1:2), individual diameters aligned closely with the expected diameter, indicated by the averages' SD range containing their respective expected diameter. This observation suggests that stretching and realignment occur simultaneously, phenomena that may be facilitated by RT stretching above PCL's T_g, resulting in a low yield strength.

Both the Fig. 3.3 histograms and SDs listed in Fig. 3.6's table reflect that greater stretch was associated with a more uniform individual diameter distribution, thereby improving fiber homogeneity. However, the opposite was true when taking into account wide fibers, which exhibited increasing SD with stretching as more and larger wide fibers formed.

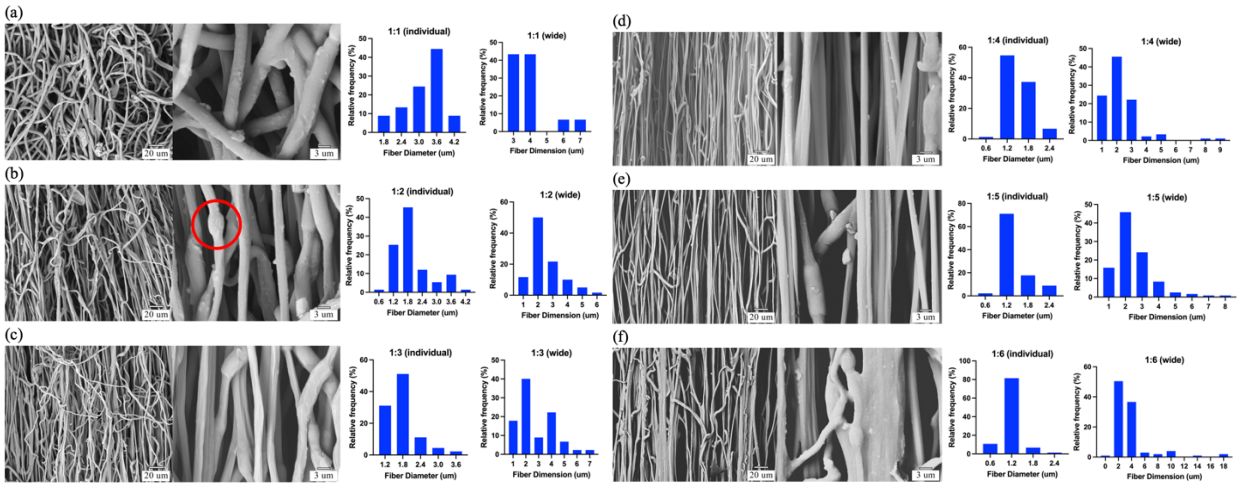

Fig. 3.3 SEM micrographs (500x magnification on left, 3000x on right) of ES PCL fibers at different stretching ratios: (a) 1:1, (b) 1:2, (c) 1:3, (d) 1:4, (e) 1:5, (f) 1:6, alongside histograms of fiber diameter frequency. 'Individual' represents measurements from only individual fibers, whereas 'wide' considers both individual fibers and coalesced ribbons.

(a) (b) (c)

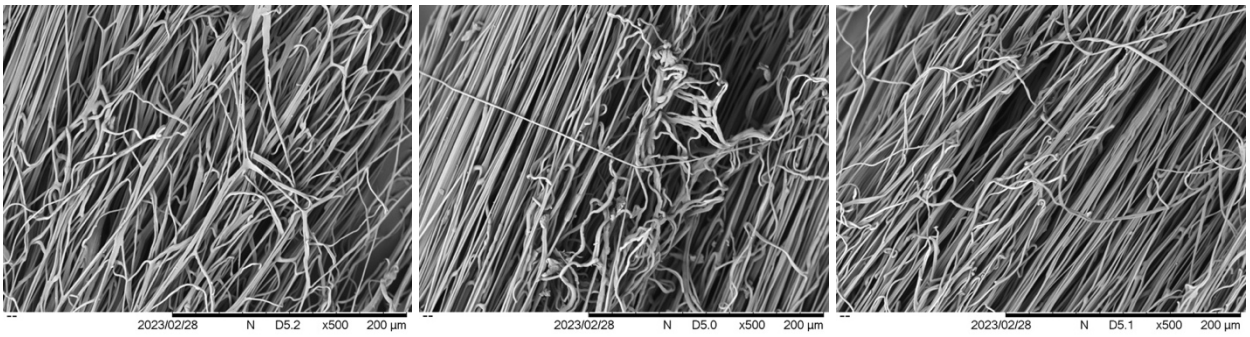

Fig. 3.4 SEM micrographs (500x magnification) of fraying breakage of PCL fibers at different stretching ratios: (a) 1:4, (b) 1:5, (c) 1:6.

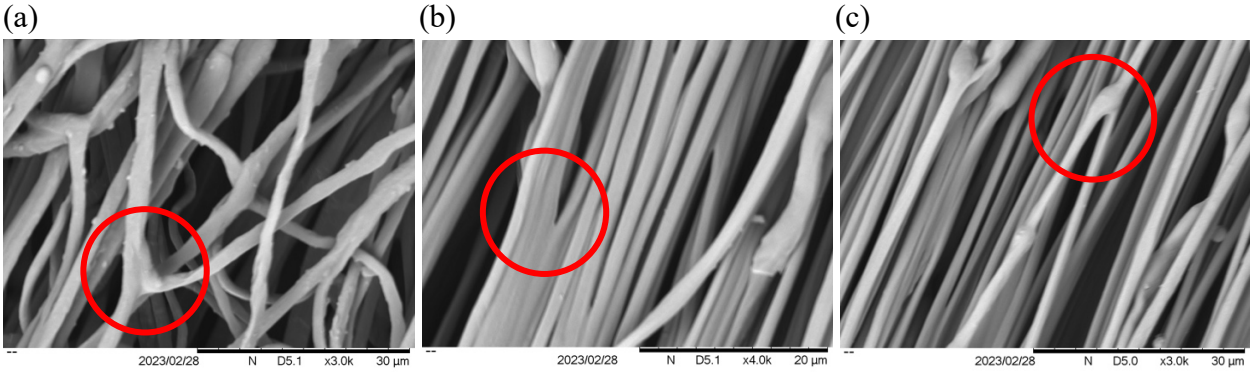

Fig. 3.5 SEM micrographs (3000x magnification) of bifurcations in PCL fibers at different stretching ratios: (a) 1:2, (b) 1:4, (c) 1:5.

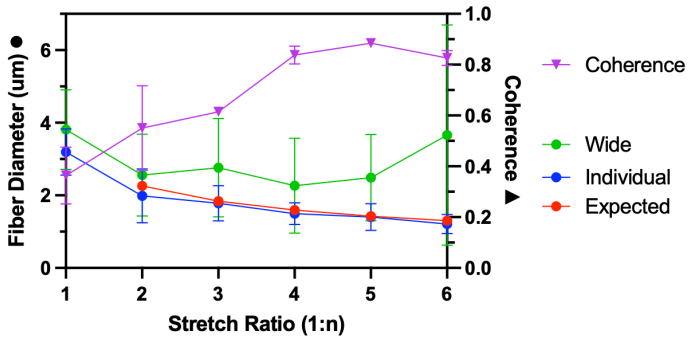

Stretch Ratio (1:n)	X	1	2	3	4	5	6
Individual (um)	Mean	3.19	1.99	1.78	1.50	1.40	1.21
	SD	0.64	0.75	0.49	0.30	0.37	0.27
Wide (um)	Mean	3.81	2.56	2.76	2.27	2.49	3.66
	SD	1.10	1.13	1.36	1.31	1.19	3.04

Fig. 3.6 Coherence of filament exterior and mean fiber diameter (green = wide ribbons included, blue = individual only, and red = expected) of filaments stretched to various degrees, measured from SEM micrographs.

3.3.2 Alignment

Both SEM and µCT were employed to examine the cross-sectional morphology of filaments to assess potential differences in fiber alignment between the filament's interior and exterior. Theoretically, the exterior might exhibit greater alignment due to more available free volume for fiber rearrangement compared to the more constricted interior.

From the SEM micrographs of the filament surface, exterior coherence progressively increased with stretch, plateauing at a peak value of approximately 0.85 at a stretch ratio of 1:4, as shown in Fig. 3.6. Further stretching beyond this ratio did not enhance fiber alignment but instead predominantly strained the fibers. This excessive straining could lead to fiber breakage and fraying, which may underlie the slight decrease in coherence at 1:6.

As for the filament interior, the 1:1 filament cross-sections presented in Fig. 3.7 were relatively circular, each containing a small gap towards the exterior. This gap was the result of the wire collector upon which fibers were collected during electrospinning. The left SEM micrograph in Fig. 3.8 also shows instances of fibers folding back onto themselves. For cold-snapped 1:6 filaments, their SEM micrographs in Fig. 3.9 show that they were flattened, which was likely an unintended consequence of SEM sample preparation. These filaments, having smaller diameters than 1:1 filaments, required greater tweezer compression to avoid slippage during snapping in nitrogen.

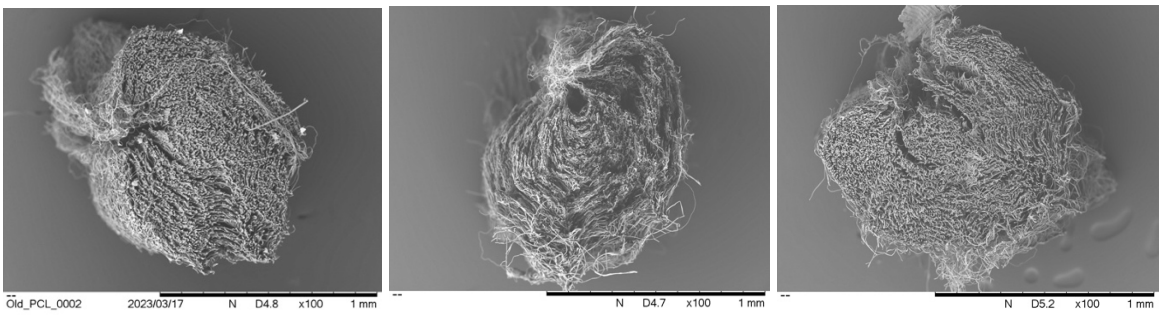

Fig. 3.7 SEM micrographs (100x magnification) of the same unstretched (1:1) filament snapped with liquid nitrogen.

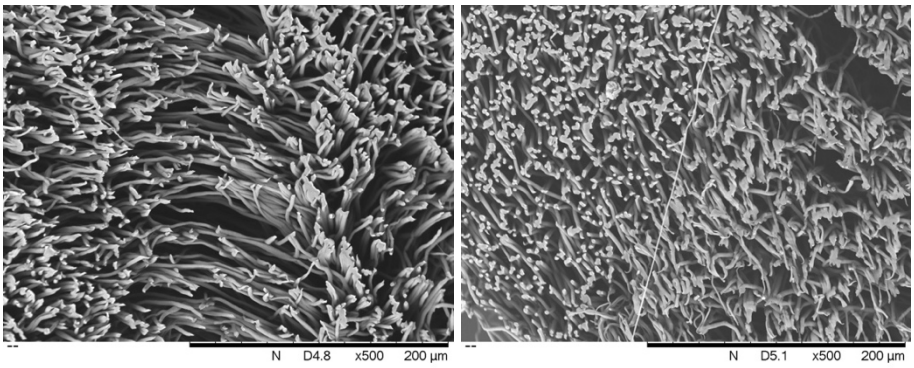

Fig. 3.8 SEM micrographs (500x magnification) of unstretched (1:1) filament snapped with liquid nitrogen.

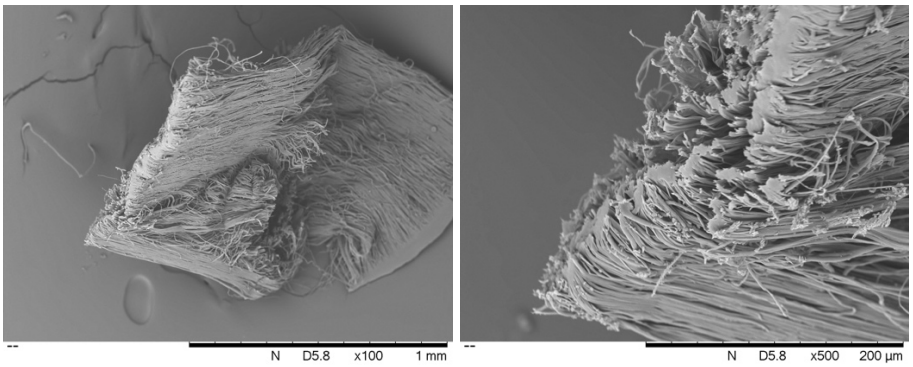

Fig. 3.9 SEM micrographs (100x magnification on left, 500x on right) of liquid nitrogen-snapped stretched (1:6) filaments.

To examine fiber alignment continuously across the fiber axis, µCT was employed. Comparing the 3D µCT renderings of 1:1 and 1:6 filaments in Fig. 3.10 showed that stretching caused exterior filament diameter to decrease and fiber alignment to increase, paralleling the observations from the SEM micrographs. Coherence was calculated on cross-sections at various distances from the filament surface. These cross-sections are shown in Fig. 3.11 and Fig. 3.12, and the coherence values are listed in Table 3.1.While these coherence values were lower than what was measured from the SEM micrographs, both µCT and SEM showed that the coherence of the 1:6 filament was about 4 times greater than that of the 1:1 filament. Notably, this held true for the interior of the 1:6 filament, showing that fibers were uniformly aligned in both the filament interior and exterior.

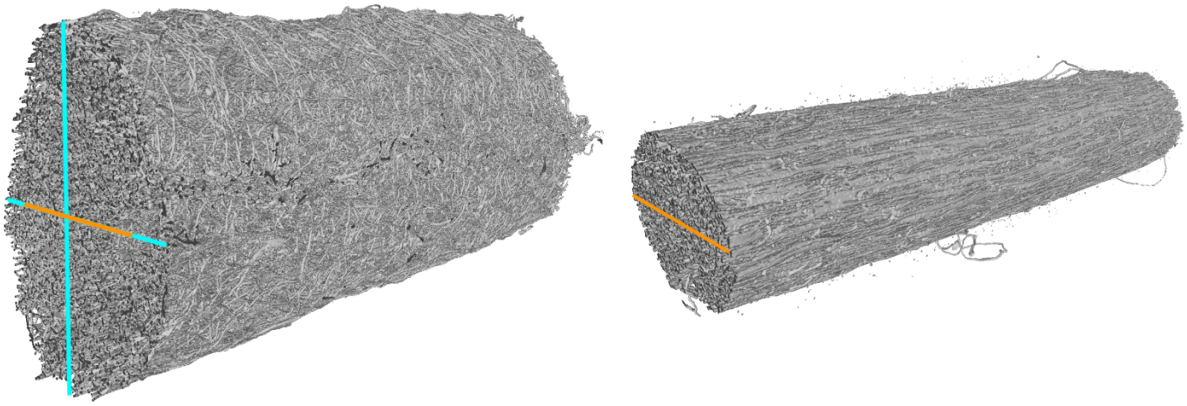

Fig. 3.10 3D µCT rendering of unstretched (left) and stretched (right) filament. Scaling: orange horizontal = 323 um, blue horizontal = 470 um, blue vertical = 670 um.

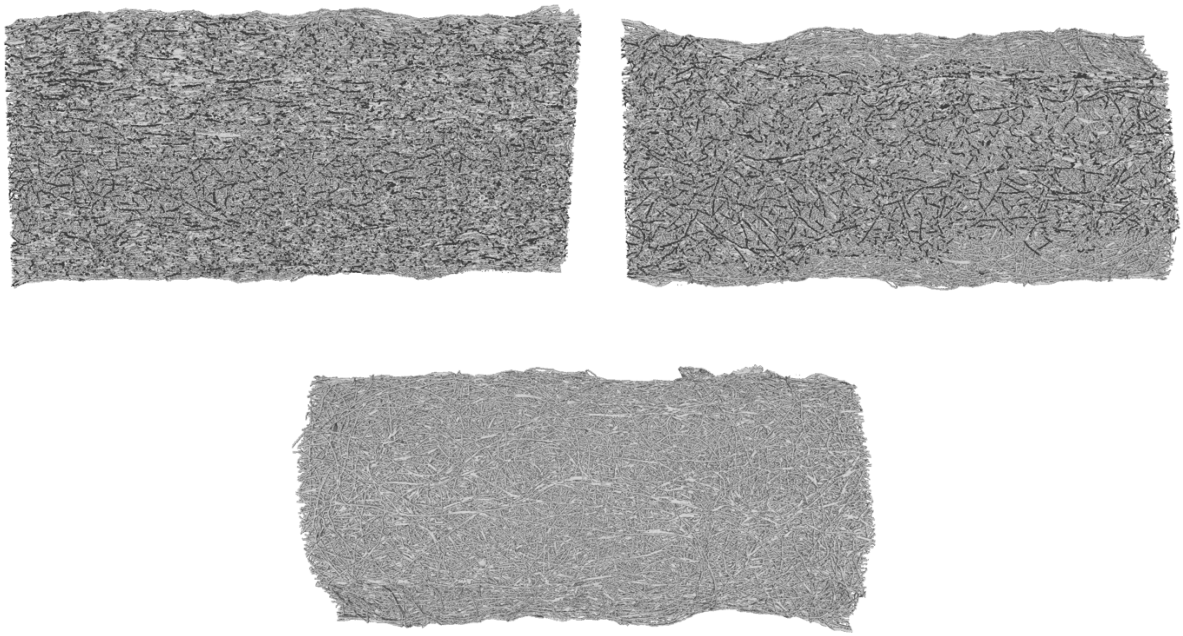

Fig. 3.11 3D µCT rendering of unstretched filament. Axial slices taken at: R (top left), 0.5R (top right), surface (bottom).

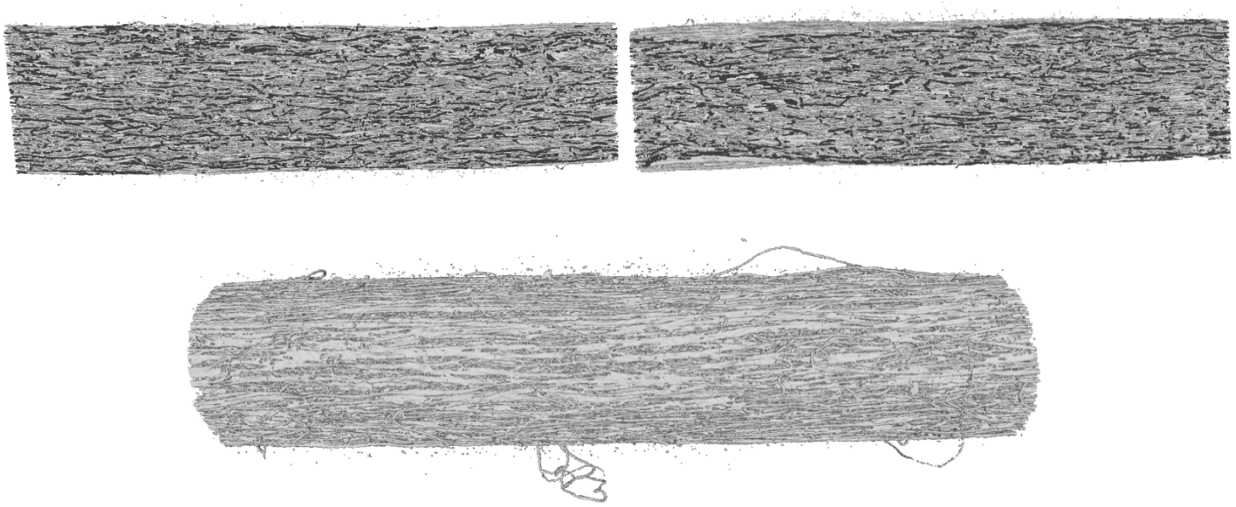

Fig. 3.12 3D μCT rendering of 1:6 stretched filament. Axial slices taken at: R (top left), 0.5R (top right), surface (bottom).

	Unstretched (1:1)	**Stretched (1:6)**
Surface	0.118	0.428
0.5R	0.083	0.406
R	0.154	0.349

Table 3.1 Coherence values for unstretched and stretched filament based on location of axial slice. Note: only one sample of each filament type was imaged in μCT.

3.3.3 Coalescence

As seen in Fig. 3.13, stretching filaments at 0 °C limited fiber coalescence in comparison to 20 °C; however, cold conditions did not completely prevent coalescence. Fig. 3.14 quantifies average fiber width under these two thermal conditions.

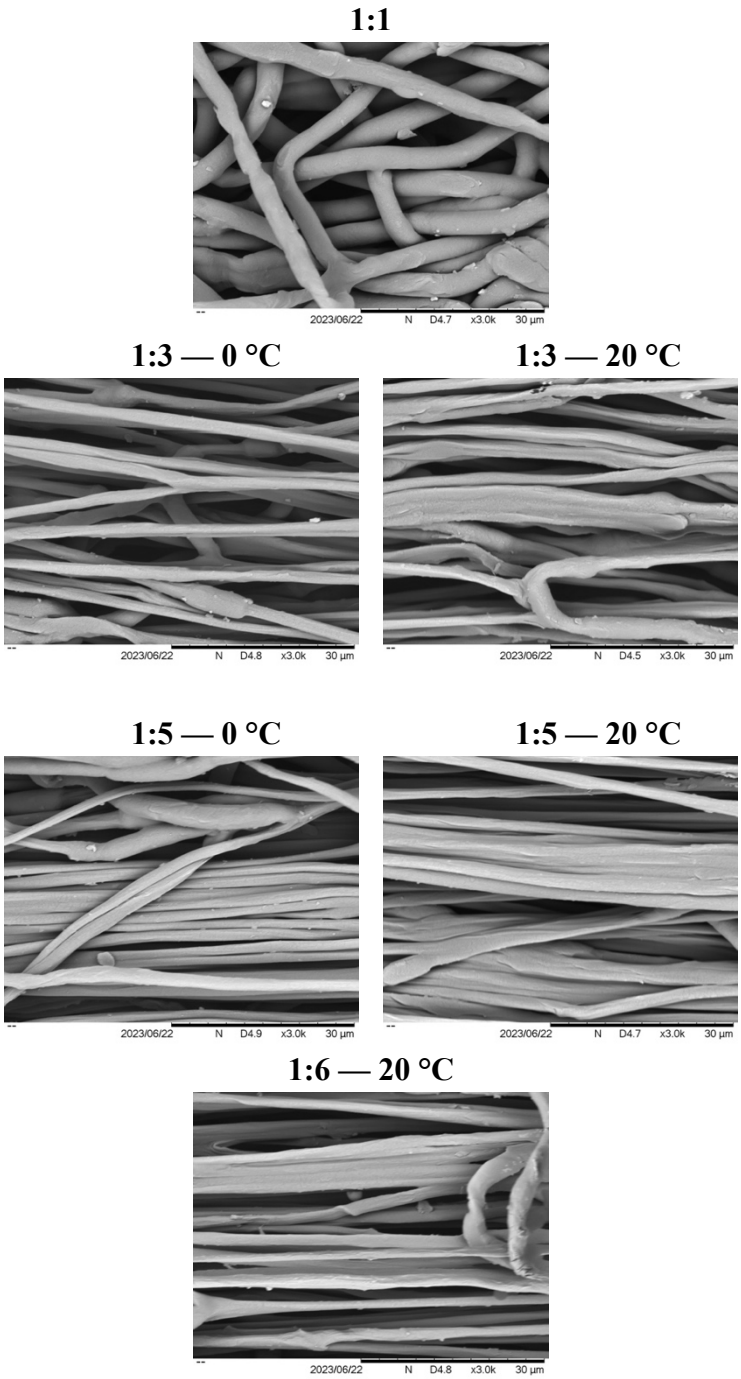

Fig. 3.13 SEM micrographs (3000x magnification) of fibers stretched to varying ratios at either 0 or 20 °C.

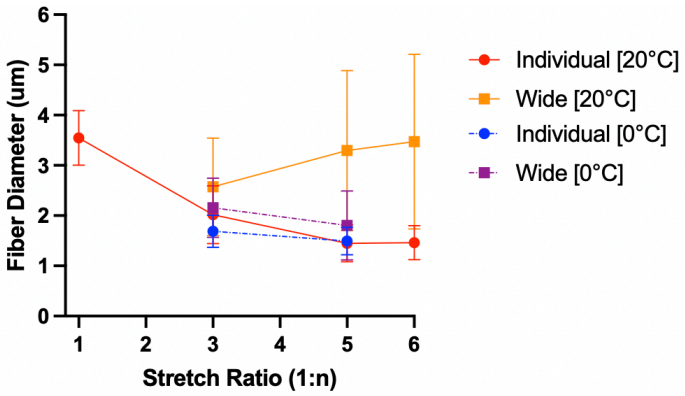

		20°C	20°C	20°C	20°C		0°C	0°C
Stretch Ratio (1:n)	**X**	**1**	**3**	**5**	**6**		**3**	**5**
Individual (um)	Mean	3.55	2.02	1.45	1.46		1.69	1.50
	SD	0.54	0.57	0.37	0.34		0.32	0.27
Wide (um)	Mean		2.58	3.30	3.47		2.16	1.80
	SD		0.97	1.59	1.74		0.59	0.69

Fig. 3.14 Mean fiber diameter (individual and widest included) of filaments stretched to various degrees in either 0°C or 20°C conditions.

SEM showed that coalescence was lower in dual thermal filaments (Fig. 3.15) — stretched to their maximum elongation first in cold conditions, then finishing stretching at RT — in comparison to filaments stretched only at RT (Fig. 3.16). Therefore, consecutive cold-to-RT dual thermal stretching appears to be an effective method to achieve maximum plastic deformation while preserving microstructural integrity.

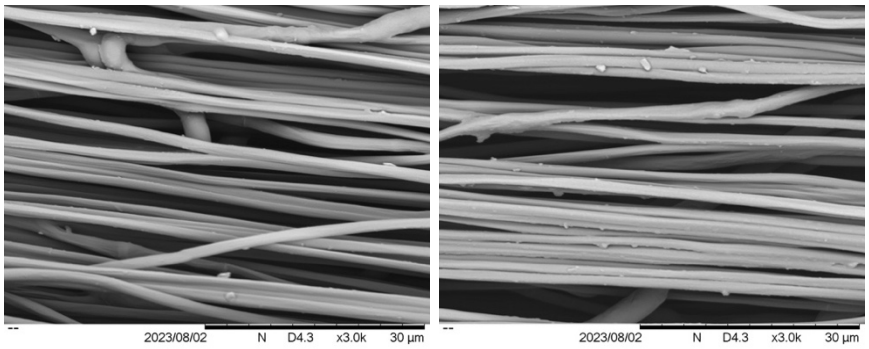

Fig. 3.15 SEM micrographs (3000x magnification) of 'dual thermal' filaments, stretched to 1:5 in ice water then extended to 1:6 in RT.

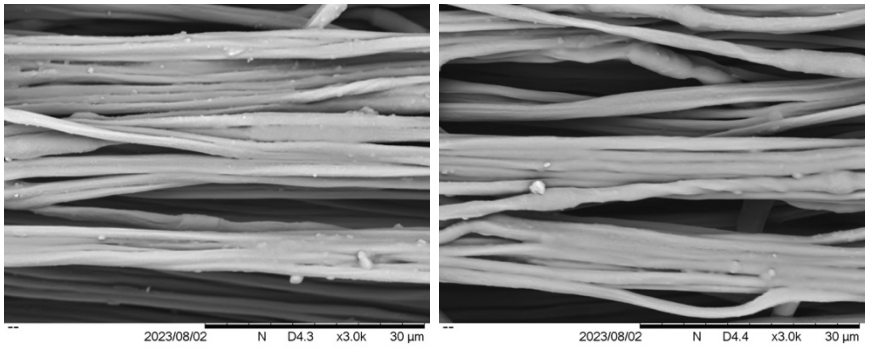

Fig. 3.16 SEM micrographs (3000x magnification) of filaments stretched to 1:6 at RT.

The most severe coalescence was observed in the multifilament stored at RT for over 5 months, with its SEM micrograph presented in Fig. 3.17. This showed that even in ambient conditions, fibers could meld together. To prevent coalescence, filaments should be stretched and stored in colder temperatures to preserve their fine fibrous architecture. Storage temperature should ideally be below T_g to prevent ambient microstructural changes, whereas stretching must take place above T_g so that the filaments are not in the glassy regime, which would cause shattering upon straining.

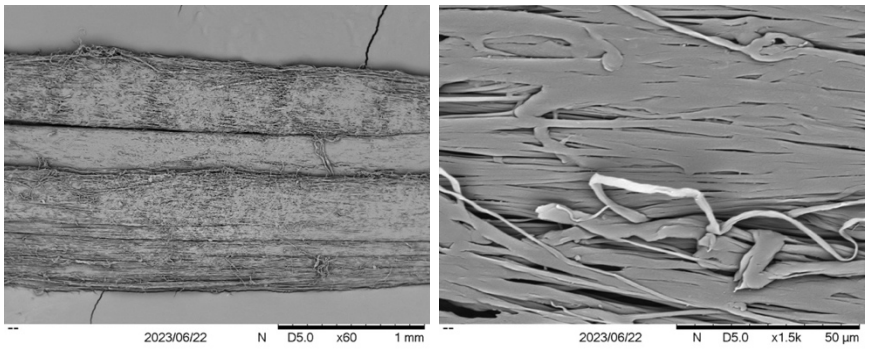

Fig. 3.17 SEM micrographs (60x magnification on left, 1500x on right) of multifilament stretched and stored at RT.

3.4 Thermal Analysis (DSC): Melting Endotherm and Degree of Crystallinity

3.4.1 Sample Type & Degree of Stretch

Fig. 3.18 depicts DSC curves obtained from PCL at various stages in processing: pellet, 1:1 filament, and 1:6 filament. Fig. 3.19 shows the curves of filaments stretched to varying degrees. All filaments exhibited a primary endotherm (Peak 1) with a peak temperature around 60 °C. Progressive stretching of PCL filaments displayed the growth of a secondary endotherm (Peak 2) extending to higher temperatures, reaching a maximum size at the greatest degree of stretch before fracture, 1:6. An endothermic pre-melting peak, or ‘pre-peak’, was most evident in the pellet and at lower stretching ratios, gradually shrinking with stretching.

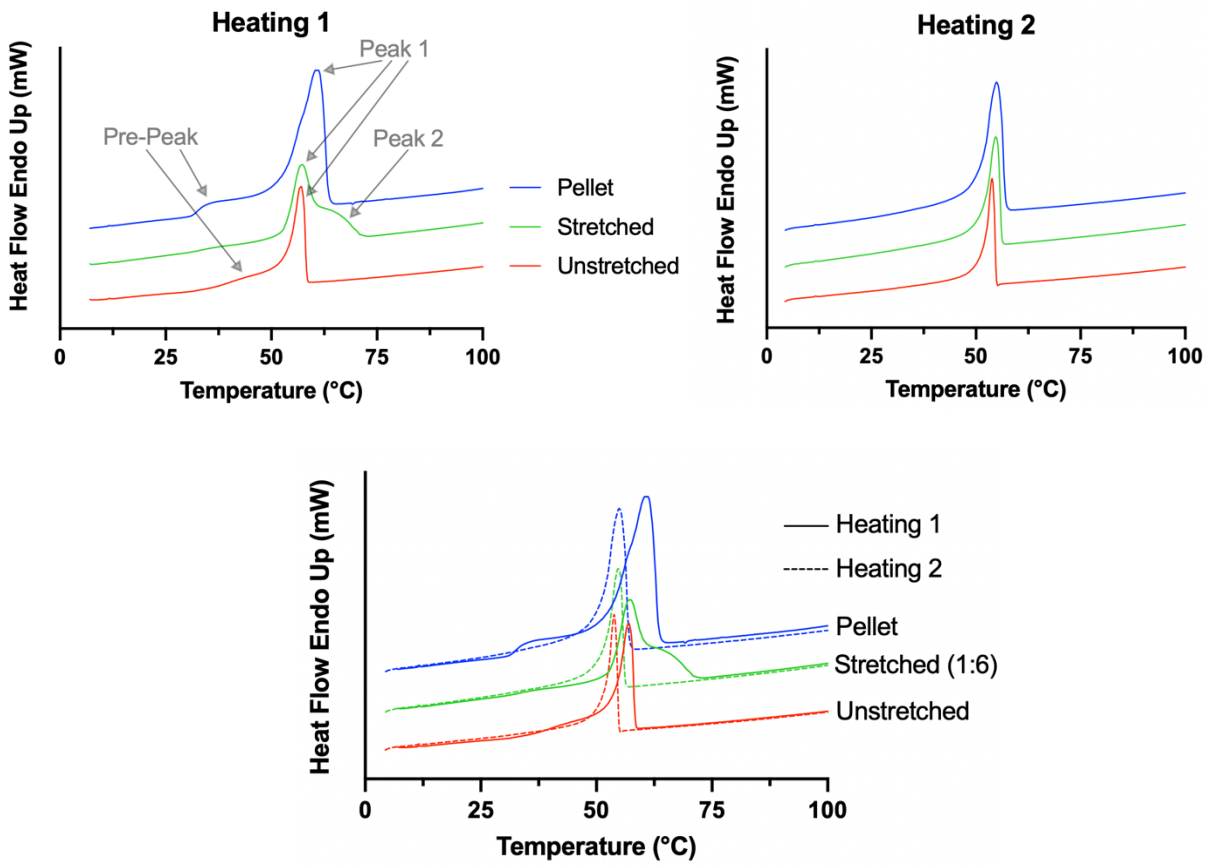

Fig. 3.18 DSC curves of Mw PCL during Heating 1 (top left), Heating 2 (top right), and both cycles (bottom).

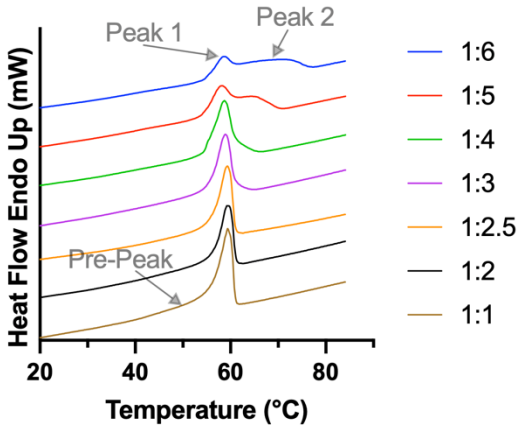

Fig. 3.19 DSC curves of PCL filaments stretched to varying degrees (1:1-1:6).

Fig. 3.20 quantifies the evolution of Peak 2 with stretching. This peak increased in area and width, which correlate with a greater melting enthalpy and melting enthalpy distribution, respectively. The relation of endotherm width to crystal size distribution is explained in Section 4.4.2. Notably, as the sample is stretched, the melting enthalpy of Peak 1 decreased while that of Peak 2 increased. This suggests that the strain initiates crystal transformation of crystals associated with Peak 1 to Peak 2.

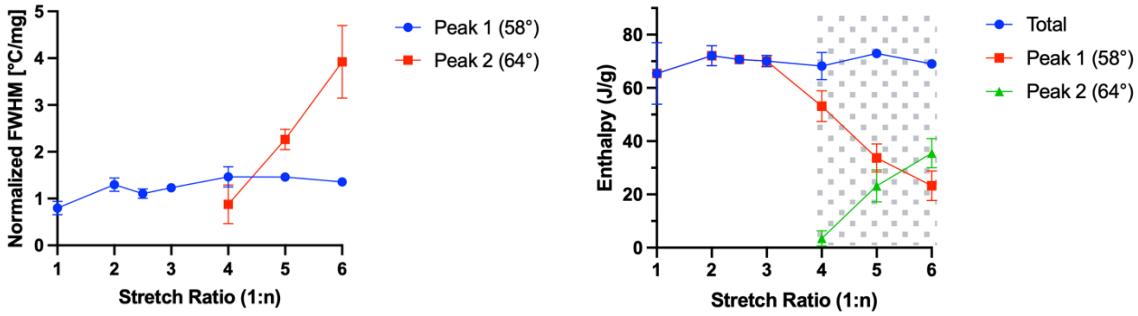

Fig. 3.20 Effect of stretching on FWHM (left) and melting enthalpy (right) on PCL filaments. The shaded region on the right plot reflects curves that exhibited a double peak.

3.4.1.1 Pan Contact

The investigation into the potential effects of sample-pan contact on DSC-measured heat flow was prompted by the initial observation of a pre-peak at approximately 40°C. While a main melting endotherm around 60 °C was observed in all samples, the pre-peak was most obvious in the pellet and 1:1 filaments, but not 1:6 filaments (Fig. 3.18). It was crucial to determine whether the pre-peak was a result of glass transition, melting of lower stability crystals (relative to the crystal population represented by the main endotherm), or an intrusive instrumental artifact. The source of the pre-peak informed whether it should be included in the integration used to calculate melting enthalpy and subsequently X_c. The pre-peak should only be included if it represented crystal melting.

As for the glass transition hypothesis, this idea originated from the fact that inflection points in DSC often indicate a material's T_g. Literature reports PCL's T_g to be -60 °C (*72*), however the pre-peak appeared at a temperature 100 °C higher than the reported T_g. In general, T_g can be raised by an increase in X_c due to the restrictive effect that crystalline regions have on the mobility of chains within the amorphous domain (*42*, *44*, *45*). However, the X_c values in my study were within the reported range for PCL and remained constant across sample types, as will be discussed in further detail in Section 3.4.1.2. Thus, X_c herein could not have caused such a significant increase in T_g from -60 °C, so it was concluded that the pre-peak was not a reflection of T_g.

As for the remaining hypotheses, the pre-peak could have been the result of either i) melting of lower stability crystals, reflective of innate material structure, ii) changing sample-pan contact due to softening of the material onto pan, reflective of a measurement artifact, or iii) a convolution of these two phenomena, with i) leading to ii). For ii), the pre-peak might have been a premature signal resulting from increased heat transfer from improvements in sample-pan contact during DSC heat ramp-up. For iii), lower stability crystals might have melted at temperatures around the pre-peak — crystals which previously acted as obstructions to rubbery amorphous flow. Once these obstructions were eliminated, the material might have more readily softened onto the pan base, improving contact. The extent to which each phenomenon might have contributed to the pre-peak remained to be determined.

This inquiry was addressed through both my experimentation and literature review. The pan contact experiment revealed that regardless of sample contact, the pre-peak was present and similar in size and shape (Fig. 3.21). The differences in peak height were irrelevant, as greater sample mass correlated with greater heat flow.

Literature reports also present a pre-peak at 40 °C in unstretched ES PCL fibers (*31*, *73–77*). The consistency of the pre-peak did not, however, confirm that it reflected PCL's innate structure, as it was possible that fibers across these studies experienced the same instrumental artifact effect. Given the porous nature of unstretched fibers, incomplete sample-pan contact was possibly shared by all these samples. However, the artifact hypothesis was challenged by the absence of a pre-peak in DSC scans of ES fibers comprised of other polymers (e.g., PLLA, polyvinylidene fluoride (PVDF)) (*78–80*). In addition, a study on solid PCL films also reported a pre-peak (*81*), underscoring that poor sample-pan contact caused by fibrous sample morphology was unlikely to be the source of the pre-peak. Integrating my experimental findings with existing literature, there is a greater likelihood that low-stability crystal melting is the primary mechanism underlying pre-peak formation.

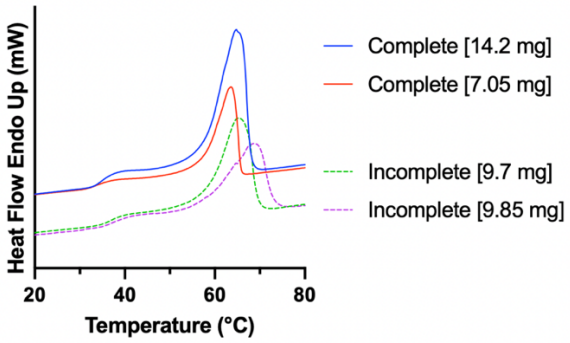

Fig. 3.21 DSC curves of pellet with either complete or incomplete pan contact. Sample mass included due to mass heterogeneity, where greater mass increases heat flow signal.

The calculated X_c for pellets with different pan contact was statistically similar (~61%) as expected due to the consistent presence of the pre-peak, shown in Fig. 3.22. Pellets with incomplete contact had a greater SD (4.56) for X_c compared to pellets with complete contact (1.16). This could have been due to greater thermal lag with incomplete contact, as heat transfer is less efficient with a smaller sample-pan interface. Thermal lag causes a time delay before the sample achieves the same temperature as the furnace, reflected by a broader peak shifted to higher temperatures. Such a peak change was seen in incomplete contact samples for both the pellet (Fig. 3.21) and 1:6 filament (Fig. 3.23).

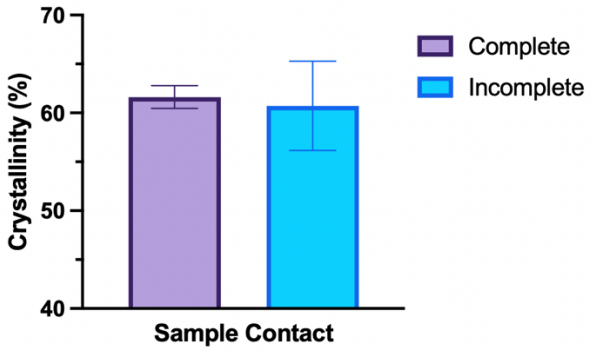

Complete		Incomplete	
Mean	SD	Mean	SD
61.62	1.16	60.69	4.56

Fig. 3.22 Crystallinity of pellet with either complete or incomplete pan contact.

For 1:6 filaments, which exhibited Peak 2, better contact appeared to shrink this peak in breadth and relative height, as shown in Fig. 3.23 and further discussed in Section 4.4.1.2. No significant difference in X_c was observed from differences in pan contact (Fig. 3.24). SD was slightly greater for the complete-contact sample with 1:6 filaments, which was the opposite trend than what was observed for the pellet.

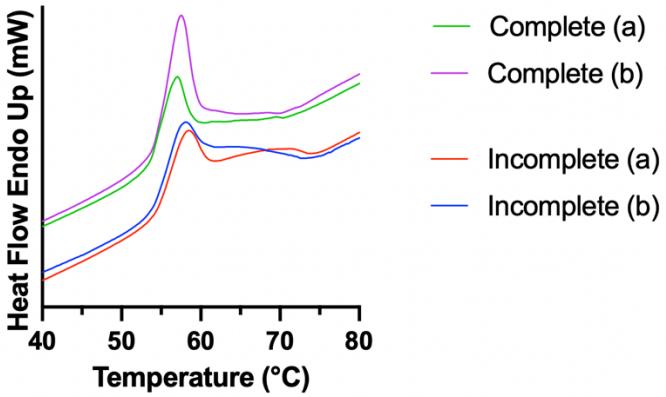

Fig. 3.23 DSC curves of 1:6 stretched filament with either complete or incomplete pan contact.

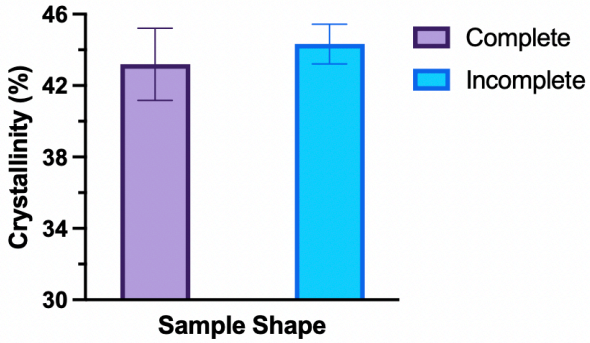

Complete		Incomplete	
Mean	SD	Mean	SD
43.19	2.02	44.33	1.12

Fig. 3.24 Crystallinity of 1:6 stretched filament with either complete or incomplete pan contact.

3.4.1.2 Crystallinity

X_c calculated for all sample types from Fig. 3.18 were not significantly different: 59.9 ± 1.8 %, 57.2 ± 1.0 %, and 57.8 ± 1.6 % for the pellet, 1:1 filament, and 1:6 filament, respectively, as reported in Fig. 3.25. Although the differences in X_c between sample types were not significant, the pellet had the highest average X_c, followed by the stretched filaments, then unstretched. This trend is reflected in literature. Wang et al. found that randomly deposited ES PCL fibers had a lower X_c (50%) than bulk polymer pellets (58%) and aligned fibers produced using two parallel plate collectors during spinning (54-57%) (*31*). In comparison to the pellet, literature attributes

the lower X_c in ES samples to the high solvent evaporation rate upon deposition, leading to rapid chain solidifcation (*31*, *82*). This adds a kinetic barrier to crystallization, lessening the time chains have for rearrangement within the microfibers.

An insignificant difference in X_c was also observed across filaments stretched to varying degrees, reported in Fig. 3.26. Across degrees of stretch, the average X_c was 50.10 ± 1.39 %. While this value was lower than those from the sample type experiment, it is important to remember that in general, the most valuable comparisons of X_c are relative and within experiments, rather than quantitatively absolute and across experiments. Experiments in my present work were conducted over two years which added the variable of aging, and samples were taken from different spin batches. Thus, differential measurement conditions likely underlie the observed differences in X_c across experiments.

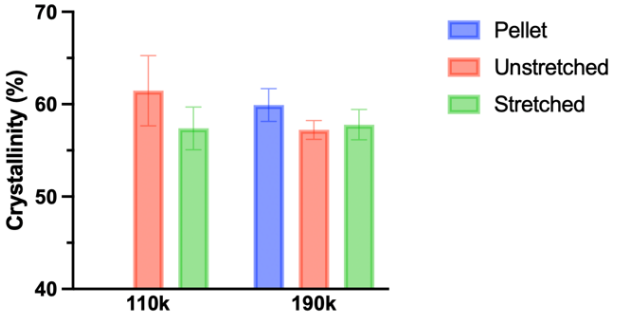

	Pellet		Unstretched		Stretched	
	Mean	SD	Mean	SD	Mean	SD
110k			61.46	3.81	57.39	2.32
190k	59.92	1.78	57.22	1.02	57.79	1.64

Fig. 3.25 Crystallinity calculated from Heating 1 DSC curves in Fig. 3.19 for PCL based on molecular weight and sample type (pellet, unstretched, and stretched filament).

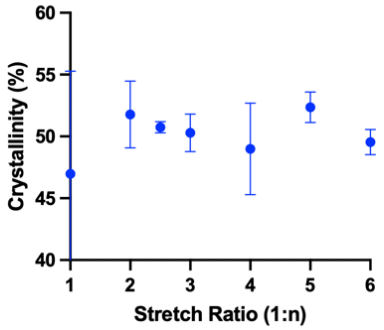

	Stretch Ratio (1:n)						
	1	2	2.5	3	4	5	6
Mean	46.98	51.78	50.75	50.29	48.99	52.35	49.55
SD	8.30	2.70	0.46	1.52	3.70	1.24	1.02

Fig. 3.26 Crystallinity calculated from Heating 1 DSC curves in Fig. 3.18 for progressive stretch of PCL filaments.

These X_c values (Fig. 3.26) reasonably aligned with that of literature, albeit slightly lower, which may have been due to the higher Mw used in this study. Literature values report that the X_c of ES PCL fibers fall between 50 and 65% depending on processing conditions, Mw, and measurement technique (*29*, *31*, *83*, *84*). However, numerous studies report that fibers subject to stretching forces have a greater X_c compared to unstretched fibers (*19–22*, *24*, *27*, *29*, *82*, *85*, *86*). This was not observed in my study.

From Heating 1 to 2, X_c lowered by ~25 percentage points, as shown in Fig. 3.27. This was also observed in other reports on ES PCL fibers (*16*, *53*), suggesting that the thermal and mechanical conditions of electrospinning prompt greater crystallization than DSC melt-cooling.

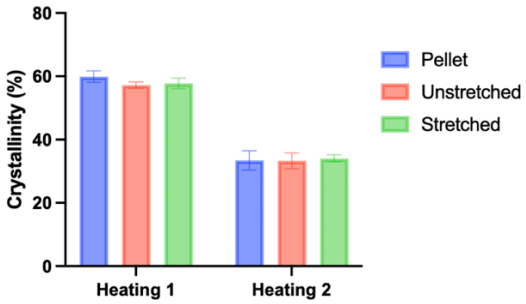

	Pellet		Unstretched		Stretched	
	Mean	SD	Mean	SD	Mean	SD
Heating 1	59.92	1.78	57.22	1.02	57.79	1.64
Heating 2	33.42	3.06	33.31	2.51	34.06	1.14

Fig. 3.27 Crystallinity of PCL based on sample type (pellet, unstretched, and 1:6 stretched filament) from Heating 1 and 2.

3.4.1.3 Onset and Peak Melting Temperature

Fig. 3.28 shows the onset and peak temperatures of the main endotherm, Peak 1. The onset temperature is typically graphically defined as the temperature at which the peak's tangent line intersects with the baseline. It is theoretically defined as the temperature at which melting begins at a measurable rate. The peak temperature marks when maximum heat flow is measured. Heating 1, which reflects processing history, showed no significant difference in onset temperatures between sample types. In Fig. 3.29, the onset temperature is again reported but this time considering the pre-peak. In this case, melting onset was much lower for the pellet and unstretched sample.

As for the peak melting temperature, there was a significantly strong difference, where the pellet presented a much higher peak temperature (61.45 °C) compared to both the unstretched (57.08 °C) and stretched filaments (57.06 °C). The values fell within reasonable range of PCL's reported 60 °C T_m.

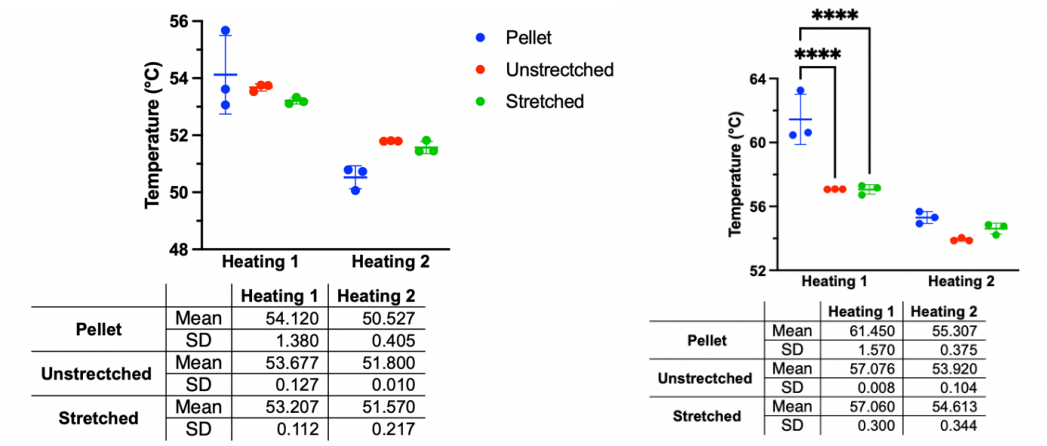

		Heating 1	Heating 2
Pellet	Mean	54.120	50.527
	SD	1.380	0.405
Unstrectched	Mean	53.677	51.800
	SD	0.127	0.010
Stretched	Mean	53.207	51.570
	SD	0.112	0.217

		Heating 1	Heating 2
Pellet	Mean	61.450	55.307
	SD	1.570	0.375
Unstrectched	Mean	57.076	53.920
	SD	0.008	0.104
Stretched	Mean	57.060	54.613
	SD	0.300	0.344

Fig. 3.28 Melting onset (left) and peak (right) temperatures of main melting endotherm Peak 1.

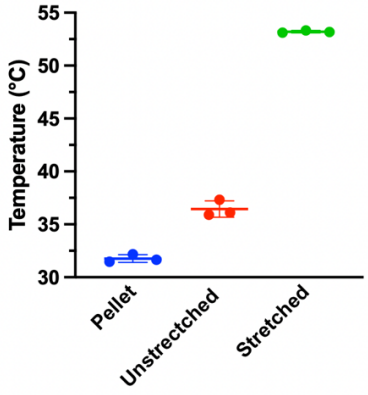

Pellet		Unstrectched		Stretched	
Mean	SD	Mean	SD	Mean	SD
31.77	0.37	36.45	0.77	53.21	0.11

Fig. 3.29 Melting onset temperature when considering pre-peak (from Heating 1).

In DSC, maximum peak temperature is susceptible to multiple variables, including sample mass, density, crucible contact, and heating rate (*87*). On the other hand, onset temperature is not susceptible to factors such as heating rate nor mass (*88*). In the case of the pellet, its larger sample volume compared to the filaments might explain why it had the highest peak temperature, caused by a kinetic lag. A thermal gradient within a sample can result in a higher recorded temperature compared to the actual average sample temperature. The stability of the

onset temperature renders it a useful metric for DSC calibration and a better indicator of a sample's properties compared to peak temperature. The consistency of the main peak's melting onset across samples showed that through processing, the crystal population that melted around 60 °C remains, albeit in varying fractions. The earlier onset of melting in the pellet and unstretched filaments, as represented by the pre-peak, suggests these samples contain a less stable crystal population.

Thermal lag might be used to describe why the onset and peak temperatures decreased from Heating 1 to 2. After Heating 1, the sample completely melted and presumably had nearly perfect contact with the pan base. This increased contact area could mean that the sample experienced less thermal lag during Heating 2, thereby recording a peak temperature lower than that of Heating 1. Alternatively, the lowering of T_m from Heating 1 to 2 could indicate the formation of less stable crystals in Heating 2 as a product of the rapid cooling during DSC measurement.

3.4.1.4 Molecular Weight

In the curves of 1:6 filaments shown in Fig. 3.30, Peak 2 was significantly taller and wider in filaments with Mw of 190k compared to 110k.

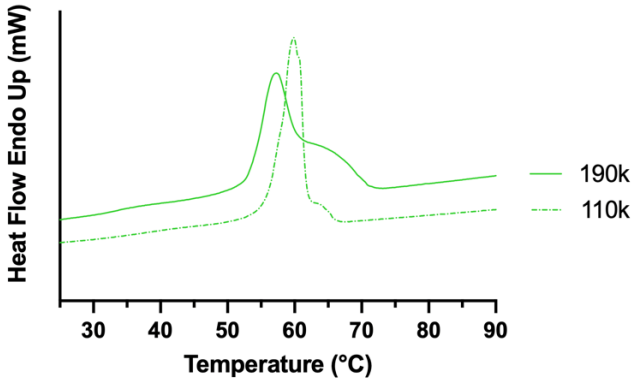

Fig. 3.30 DSC curves of 1:6 stretched filaments for Mw = 110k and 190k during Heating 1.

Fig. 3.31 shows the melting enthalpy of each subpeak for 1:6 filaments of the two Mws. Melting enthalpy is proportional to the area under the endotherm and reflects the relative amount of that crystal subpopulation. The melting enthalpy for Peak 2 was greater in the 190k filaments compared to 110k, indicating that stretching the 190k sample introduces a greater proportion of thermodynamically stable crystals.

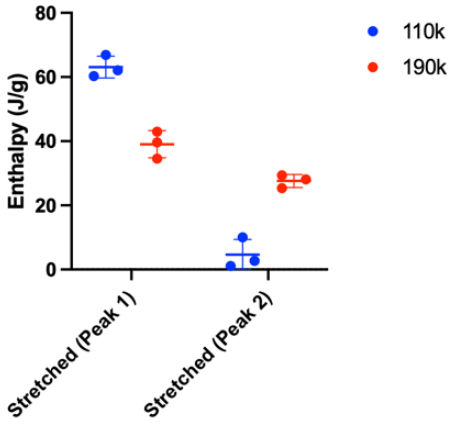

		Stretched (Peak 1)	Stretched (Peak 2)
110k	Mean	63.101	4.610
	SD	3.387	4.782
190k	Mean	39.046	27.606
	SD	4.235	2.057

Fig. 3.31 Melting enthalpy of Mw 110k and 190k 1:6 filaments.

Fig. 3.32 quantifies FWHM for each subpeak. There was no significant difference in the FWHMs of Peak 1: 4.06 ± 0.85 °C and 4.50 ± 1.05 °C, respectively. My Peak 1 FWHM measurements reasonably matched that of literature. A study on unstretched PCL nanofibers (Mw = 90k) found that the FWHM ranged from 4.4-7.8 °C using the same heating rate as my study (10 °C/min) (*16*).

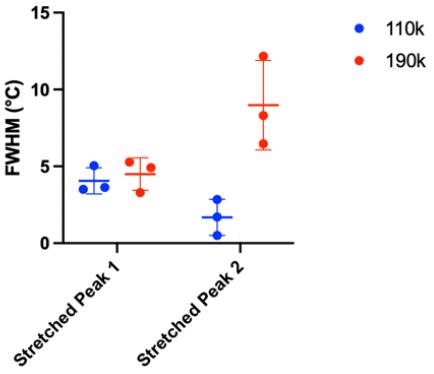

		Stretched (Peak 1)	Stretched (Peak 2)
110k	Mean	4.057	1.685
	SD	0.854	1.174
190k	Mean	4.498	8.982
	SD	1.054	2.909

Fig. 3.32 FWHM of melting peak of Mw 110k and 190k filaments, unstretched and 1:6 stretched. Stretched endotherm is differentiated into two subpeaks due to the development of its higher temperature endotherm, labeled as Peak 2.

Although there was no difference between the X_c of 110k and 190k samples (Fig. 3.33), a significant difference was seen when comparing each's FWHM of Peak 2: 1.69 ± 1.17 °C and 8.98 ± 2.91 °C, respectively. A sharp melting endotherm with a low FWHM is reflective of a crystal population with a narrow range of thermodynamic stabilities (*16*). Accordingly, stretching of 110k filaments resulted in a more uniform range of stabilities within the stretch-induced crystal population. Mw heterogeneity is *not* an explanation, as gel permeation chromatography reported in Fig. 3.34 for each Mw showed no noticeable difference in polydispersity.

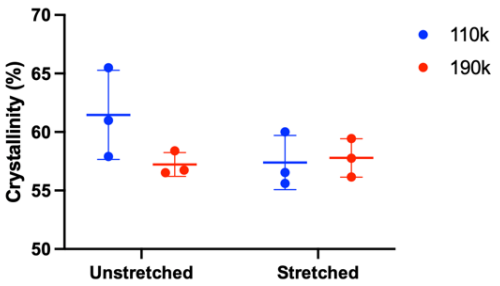

	Unstretched		Stretched	
	Mean	SD	Mean	SD
110k	61.46	3.81	57.39	2.32
190k	57.22	1.02	57.79	1.64

Fig. 3.33 Crystallinity of Mw 110k and 190k filaments, unstretched and 1:6 stretched.

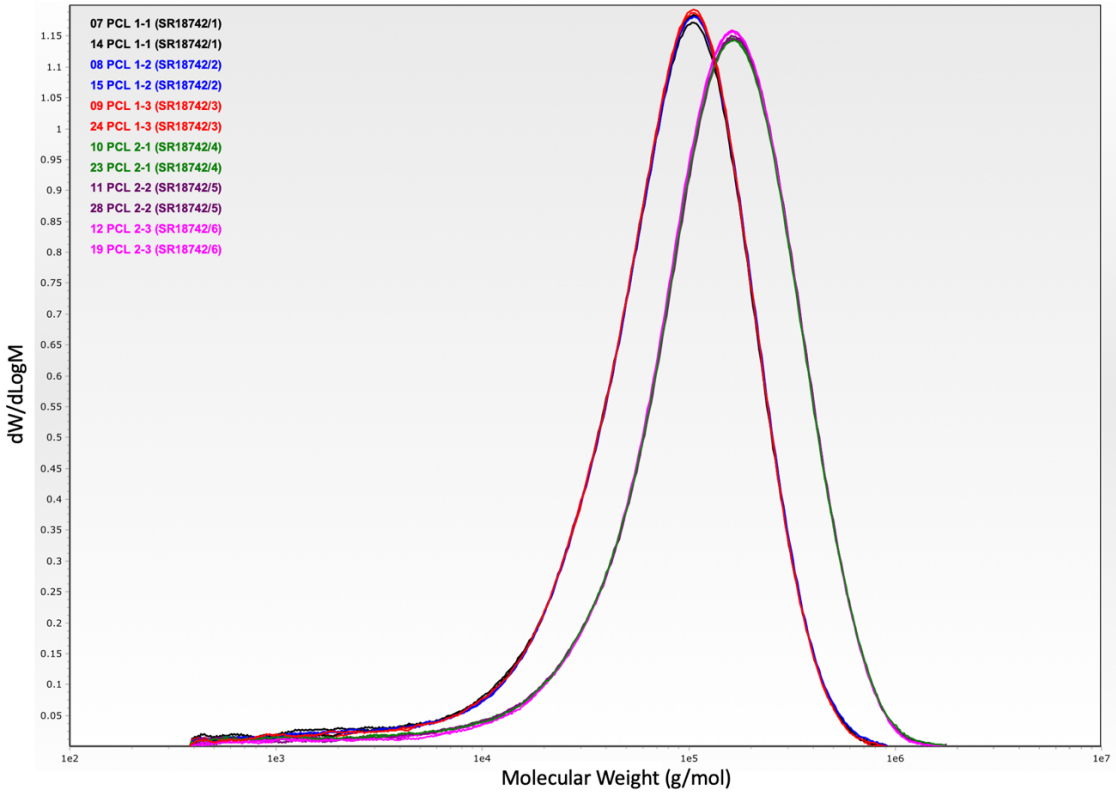

Fig. 3.34 Gel permeation chromatography plots showing Mw distribution in microfibers made from two different batches of PCL, one with an average of 110k (denoted as 1-X in legend) and another 190k (denoted as 2-X).

3.4.2 Stretch Temperature

Fig. 3.35 presents DSC curves of filaments stretched in RT and cold conditions. At 1:3, Peak 2 was not visible for either sample type, but for RT-stretched filaments, the right side of Peak 1 appeared to more gradually taper outwards to higher temperatures. By 1:5, RT-stretched filaments exhibited a much more prominent Peak 2 than cold-stretched. Greater prominence refers to Peak 2's growing height and width relative to Peak 1. For the dual thermal filaments ('Cold-RT'; stretched to their maximum 1:5 in cold conditions, then to their RT-equilibrated maximum of 1:6), Peak 2 was significantly larger than in cold-stretched 1:5 but smaller than in RT-stretched 1:6.

There was no significant difference in X_c across all these samples (Fig. 3.36), although cold-stretched samples presented the greatest SD. The larger SD could be a result of a more uneven stress distribution in cold-stretched filaments due to their stiffer, glassy character at low temperatures closer to T_g.

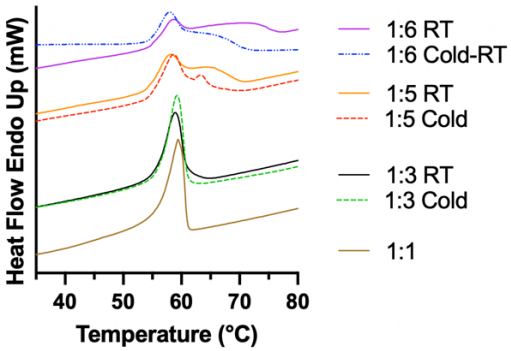

Fig. 3.35 DSC curves of PCL filament stretched to varying degrees in either RT (20 °C), cold (0 °C), or cold-RT (dual thermal) conditions.

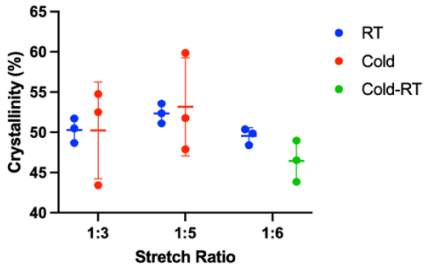

Stretch Ratio (1:n)	X	3	5	6
RT	Mean	50.29	52.35	49.55
	SD	1.52	1.24	1.02
Cold	Mean	50.24	53.18	
	SD	6.00	6.11	
Cold-RT	Mean			46.45
	SD			2.56

Fig. 3.36 Crystallinity calculated from DSC curves in Fig. 3.35 depending on degree of stretch and stretch temperature of PCL filaments.

The DSC baseline for most samples increased linearly with temperature, as seen by the upwards tilt. This is because specific heat capacity increases with temperature due to a thermally induced rise in internal energy (i.e., vibrational, rotational, and translational energy). However, for all dual thermal samples, as well as one 1:5 cold-stretched sample, the baseline was staggered, with the endothermic peak terminating at a heat flow lower than where it began. These baseline differences are depicted in Fig. 3.37. An explanation for the variance in baseline has not yet been formed, although factors such as sample-pan contact and weight loss during heating can be ruled out.

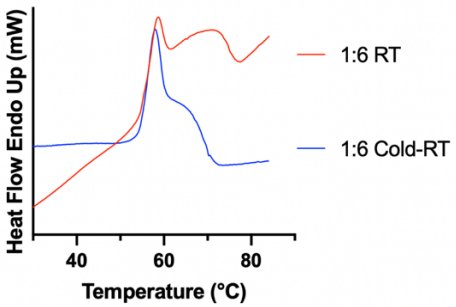

Fig. 3.37 DSC curve exhibiting differences in baseline in an RT-stretched 1:6 filament (red) versus a dual thermal-stretched filament (blue).

3.4.3 Heating Rate

Fig. 3.38 shows how heating rate changes the DSC curves of pellets. What was most significant was the change in endothermic contour. The pre-peak was most prominent at a heating rate of 25 °C/min. While the height of the melting peak increased with a greater heating rate, this was not of analytical value. Increased heat flow signal (dQ/dt) is always expected when using a faster heating rate, as it is nearly proportional to heating rate (dT/dt):

$$\frac{dQ}{dt} = C_p \frac{dT}{dt} + f(T,t)$$

where Cp = sample heat capacity, and f(T,t) = a kinetic parameter of heat flow that is a function of time at an absolute temperature T (*89*).

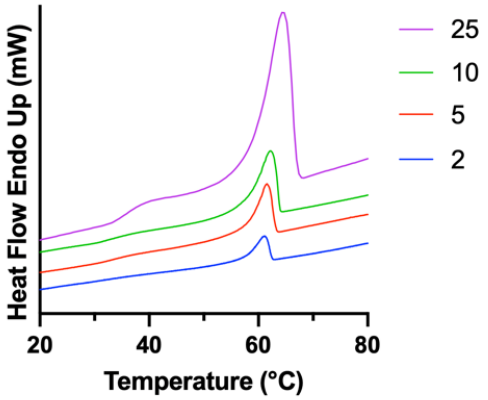

Fig. 3.38 DSC curves of PCL pellet taken at various heating rates (noted in legend, in units of °C/min).

Despite variations in peak shape, there were no significant differences in the X_c of the pellets at most heating rates (Fig. 3.39). This consistency was expected, as the replicates were from the same bulk material. A statistically significant difference in X_c existed only between 10 and 25 °C/min. This could be due to greater thermal gradients in samples heated at high rates like 25 °C/min. In calculating X_c from DSC, peak integration should ideally capture only latent heat

— the energy needed to overcome intermolecular forces during phase transformation. Thermal gradients within a sample could lead to unintended inclusion of some sensible heat in the latent heat integration — sensible heat is the energy needed to raise a material's temperature (*90*). Such an inclusion would overestimate X_c, which could explain why the X_c for 25 °C/min was greater than 10 °C/min.

SD for X_c decreased as the heating rate increases. With a greater heating rate, the same heat flow occurred over a shorter period, making the thermal event larger. Any slight instrumental inaccuracies when measuring at higher heating rates made up a smaller portion of the main Peak 1, thereby increasing measurement precision.

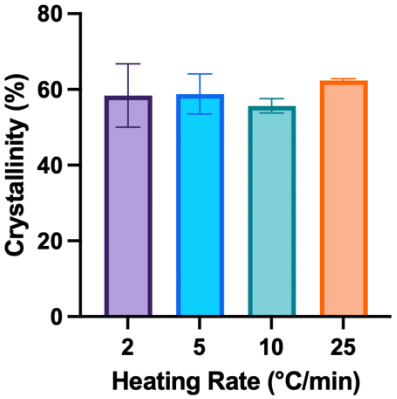

	2	5	10	25
Mean	58.38	58.78	55.65	62.36
SD	8.35	5.31	1.89	0.47

Fig. 3.39 Effect of heating rate of measured crystallinity of pellet at different heating rates.

Moving on from the pellet, Fig. 3.40 shows how heating rate affected the DSC curves of 1:1 and 1:6 filaments. As with the pellet, the pre-peak in 1:1 was most prominent at the greatest heating rate. For 1:6, a greater heating rate caused Peak 2's height to increase. As shown in Fig. 3.41, while X_c was expected to be the same within each sample type regardless of heating rate, the

measured X_c was statistically greater at 25 °C/min than at the lower two heating rates for both 1:1 and 1:6. It is possible that at lower heating rates, the decreased signal sensitivity 'blended' the edges of the melting endotherm into the baseline, subsequently causing them to be excluded from integration. Such an exclusion would result in underestimation of X_c at low heating rates.

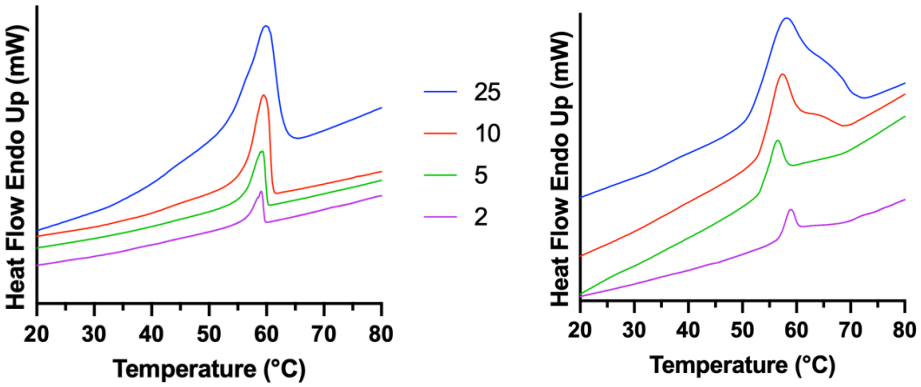

Fig. 3.40 DSC curves of unstretched (left) and 1:6 stretched (right) PCL filament taken at various heating rates (noted in legend, in units of °C/min).

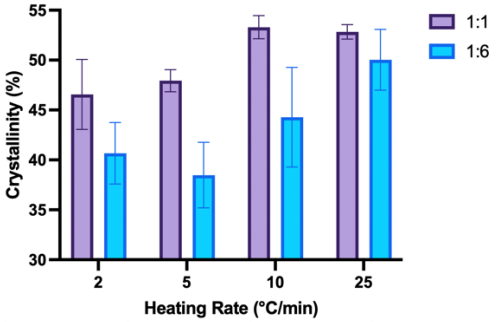

	2		5		10		25	
	Mean	SD	Mean	SD	Mean	SD	Mean	SD
1:1	46.56	3.50	47.94	1.10	53.30	1.16	52.83	0.73
1:6	40.67	3.07	38.48	3.29	44.28	5.00	50.03	3.04

Fig. 3.41 Effect of heating rate of measured crystallinity of unstretched and stretched filaments at different heating rates.

3.5 Diffractive Analysis

Fig. 3.42 shows the 1D XRD profile with the background signal subtracted for 1:1, 1:3, and 1:5 filaments. Characteristic (110), (111), and (200) peaks were located around 21.5°, 22°, and 23.8°

respectively, matching literature values (*27*, *91–95*). Notably, the peaks were broader and exhibited a slight shift towards lower Bragg angles for greater degrees of stretch. A broad halo was also evident in these profiles, arising from scattering associated with the amorphous region. This region is characterized by a lack of long-range order, with a wider distribution of molecular separations compared to the crystalline phase.

One paper identifies a (0 0 14) peak (*96*), but I could not identify such a peak when expanding the detection range beyond 77.1°, the associated 2θ for (0 0 14). The paper that identified this (00l) peak used XRD settings of 50 kV and 200 mA which were beyond the capacity of the XRD I had access to.

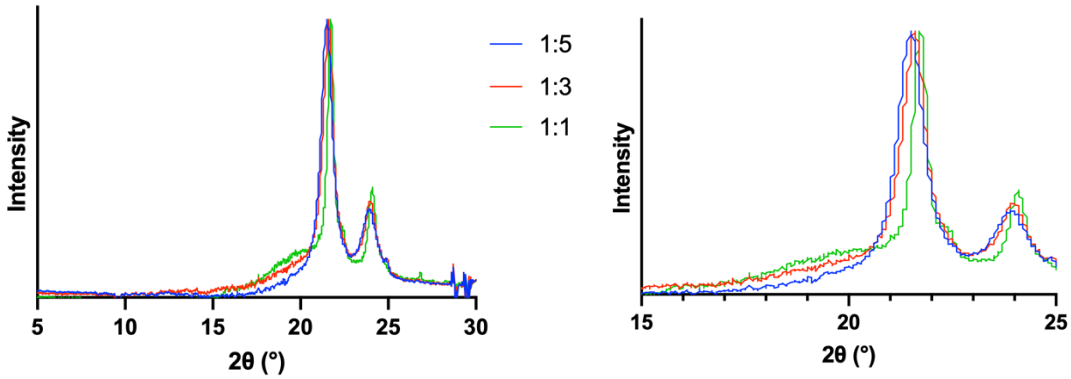

Fig. 3.42 Normalized XRD profile of PCL filaments stretched to various degrees. The right image represents the same data as the left plot but zoomed in to better visualize the left-ward peak shifts of stretched filaments.

3.5.1 Crystallinity

Fig. 3.43 shows how the measured X_c increased with stretching for both 110k and 190k filaments. The increase in X_c was more pronounced for 190k. This sample began with a lower initial X_c and concluded with a higher final X_c. It is possible that the greater initial crystalline

fraction in 110k restricted chain movement and impeded further crystal development. These results stand in contrast to the constant X_c measured in DSC, discussed further in Section 4.3.

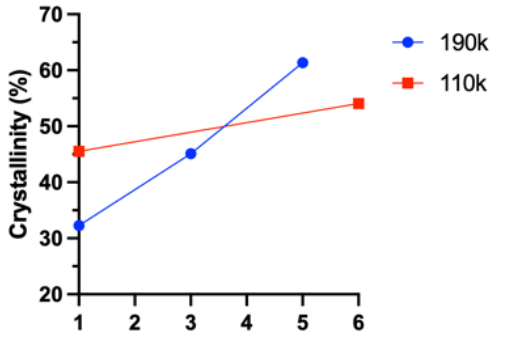

Stretched (1:n)	1	3	5	6
190k	32.28	45.09	61.36	
110k	45.51			54.06

Fig. 3.43 Crystallinity calculated from XRD of filaments as a function of stretching.

3.5.2 Crystal Size

Crystal size calculations were based on the FWHM of crystalline peaks. Smaller crystals typically exhibit wider XRD peaks, as the diffracted rays are less uniformly aligned for a given 2θ. Peak broadening can result from several factors, including lattice imperfections such as dislocations, inherent randomness in unit cell parameter length, excessive twisting of chains, and inhomogeneous strain. The influence of strain in polymer crystals is likely less pronounced than in metal crystals, as polymeric amorphous regions act as a buffer region that allows for greater relaxation before the strain load is shifted to crystalline regions. A Williamson-Hall analysis can be used to deconvolute the effects of crystal size and microstrain on peak broadening (*97*). However, the XRD profile of PCL did not have a sufficient number of peaks to justify this analysis as accurate or useful. Despite these potential contributions, for the sake of analysis, peak broadening was assumed to be the result of crystal size changes.

Horizontal crystal dimensions, perpendicular to the c-axis, shrank upon stretching in both 110k and 190k filaments, as shown in Fig. 3.44. The average horizontal crystal dimension was calculated using the (110) and (200) peaks.

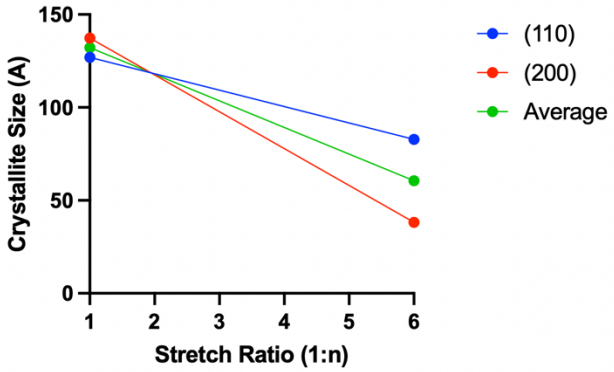

Stretch Ratio (1:n)	1	6
(110)	126.91	82.81
(200)	137.36	38.21
Average	132.14	60.51

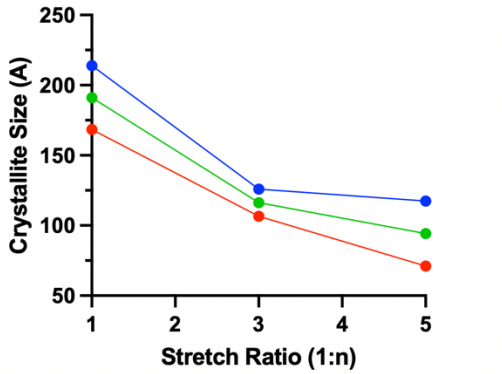

Stretch Ratio (1:n)	1	3	5
(110)	213.90	125.93	117.49
(200)	168.34	106.56	71.14
Average	191.12	116.25	94.32

Fig. 3.44 Crystal length dimensions (in Å) for each plane as a function of stretching for 110k (left) and 190k (right) filaments.

Literature suggests that stretching PCL fibers decreases the horizontal crystal dimensions, as summarized in Table 3.2. For example, in a study on ES PCL nanofibers, Wang found that randomly aligned fibers had a greater horizontal crystal size (140 Å) than aligned fibers (130 Å), which were produced by altering collector geometry (*31*). These aligned fibers experienced greater tensile forces during spinning than those randomly deposited. Wang hypothesized that the reduced crystal size in aligned fibers resulted from the enhanced extension of polymer chains during deposition, which acted as row nuclei for crystallization. However, variations in gap size, corresponding with different degrees of polymer jet stretching during deposition, did not significantly affect crystal size, casting doubt on Wang's hypothesis.

It should be mentioned that not all semicrystalline polymers exhibit decreased horizontal crystal dimensions after stretching. In a study on polyacrylonitrile (PAN) ES nanofibers that were hot-stretched after spinning, Song et al. found that average crystal size increased from 41.4 to 108.3 Å, using PAN's characteristic (100) and (110) reflections (*18*). In contrast, another study on PAN by Wu et al. found that hot-stretching of PAN nanofibers decreased crystal size by 10% based on the (100) reflection (*98*), a much smaller change than Song's study found crystal size to grow. Ultimately, the variability in literature results show that many factors, such as polymer composition and route of crystallization, impact crystal size and the effect of stretching on this parameter.

The (110) crystal dimension was longer than (200) following stretching of Biolig fibers, which other studies on stretched ES PCL fibers corroborate (*96*, *99*). This may be because shearing occurs more readily on the (200) crystal face than on the (110) face due to differences in intermolecular interactions. Of relevance is the dipole-induced dipole interaction between the electronegative oxygen of the carbonyl and the induced electropositive methylene carbon in a neighboring chain. In PCL crystals, closest-neighbor carbonyls between adjacent chains are not aligned, resulting in the nearest electropositive site being a methylene carbon, not a carbonyl carbon (*100*). Consequently, the carbonyl group is oriented more parallel to the normal of the (110) face than the (200) face, enhancing the strength of the dipole interactions along the (110) normal and increasing resistance to shearing.

PCL Form	Unstretched Crystal Size (Å)	Draw Ratio (1:n)	Stretched Crystal Size (Å)	Unstretched fiber diameter (um)	Study
Electrospun fibers	(110): 140	N/A (stretched via collector alignment)	(110): 130	0.5	(*31*)
Melt nozzle fibers	(Average): 256	N/A	N/A	13.5	(*101*)
Melt spun fibers	(110): 79 (200): 74	9	(110): 68 (200): 49	272-280	(*96*)
Melt spun fibers	N/A	6 7	(110): 60 (200): 34 (110): 58 (200): 37	59-92	(*25*)
Thin film	(110): 74 (200): 69	5	(110): 65 (200): 61	N/A	(*99*)

Table 3.2 Literature values of PCL crystal sizes depending on draw ratio and material form.

3.5.3 Lattice Parameter

In Fig. 3.42, the XRD profile for stretched filaments was slightly left-shifted compared to that of unstretched profile. This indicated a larger d-spacing between crystal planes in the stretched samples. The lattice parameters *a* and *b* grew with stretch for both the 110k and 190k samples, as shown in Fig. 3.45. This may be the combined result of tensile forces directly straining unit cells and the formation of non-ideal crystal conformations. During CFC unraveling, average d-spacings may temporarily increase from the thermodynamically ideal. It is also possible that an elevated sample surface could cause a rightward shift in the XRD profile due to diffraction at smaller Bragg angles.

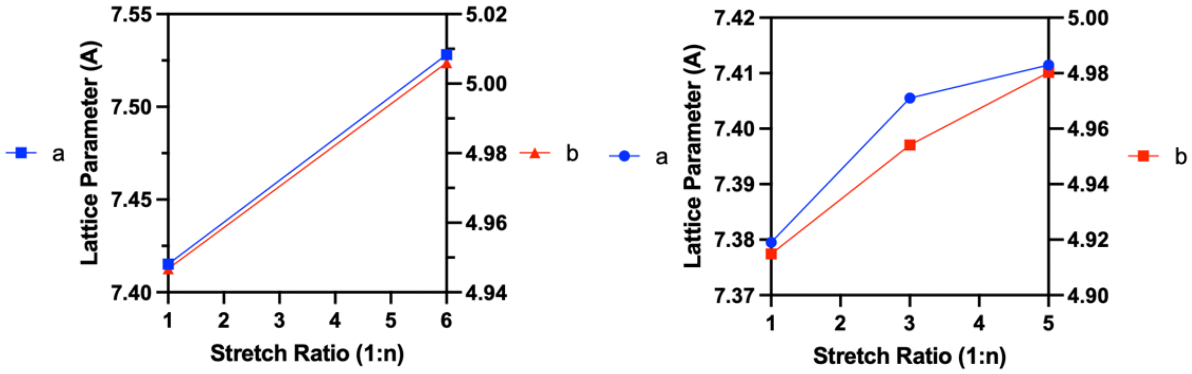

Stretch Ratio (1:n)	1	6
a	7.415	7.528
b	4.947	5.006

Stretch Ratio (1:n)	1	3	5
a	7.380	7.406	7.411
b	4.915	4.954	4.980

Fig. 3.45 Lattice parameter (in Å) as a function of stretching for 110k (left) and 190k (right) filaments.

3.5.4 Crystal Orientation

Fig. 3.46 shows the 2D azimuthal scans of 1:1 and 1:6 filaments. Fig. 3.47 plots the intensity of each Debye-Scherrer ring as a function of azimuthal angle β. Each ring corresponds with diffraction from a specific crystallographic plane. The diffraction intensity along a ring for a particular plane can be used to compare crystal orientation across samples (*23*). Bright spots in a ring reflect a strong diffraction signal from anisotropically oriented crystal planes, whereas a uniform ring indicates an isotropic sample.

In all scans, two rings were present. The inner ring corresponded to the (110) crystal plane at 2θ = 22° and the outer ring to the (200) crystal plane at 2θ = 24° (*102*). Only 1:6 filaments oriented ⊥ to the X-ray beam exhibited discrete OOP diffraction spots, whereas the remaining samples presented uniform rings. The contrast between sample orientations suggests stretched filaments possess strong anisotropic character.

Some artifacts due to XRD instrumentation arose, not to be confused with features of the sample. Software acquisition discontinuities took place around β = 50°, particularly evident in the 1:1|| scan. Another artifact was peak spreading in the IP direction (i.e., bottom left). Such spreading was a result of the 1° beam divergence in this direction; as the beam traveled from X-ray source to detector, it deviated farther from the origin axis. Mirrors were used to collimate the beam, so it was parallel in the OOP direction, but this was not done in the IP direction. The X-ray source was also wider in the IP direction than it was tall.

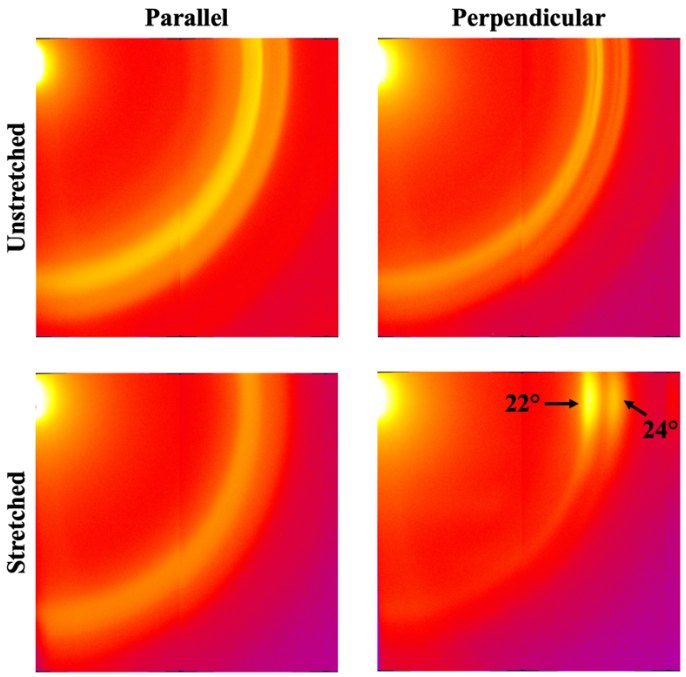

Fig. 3.46 2D XRD azimuthal scans of 1:1 and 1:6 filaments orientated parallel and perpendicular to X-ray beam. Debye-Scherrer rings for 2θ of 22° and 24° are marked on just one of the scans, although the rings are present in all scans.

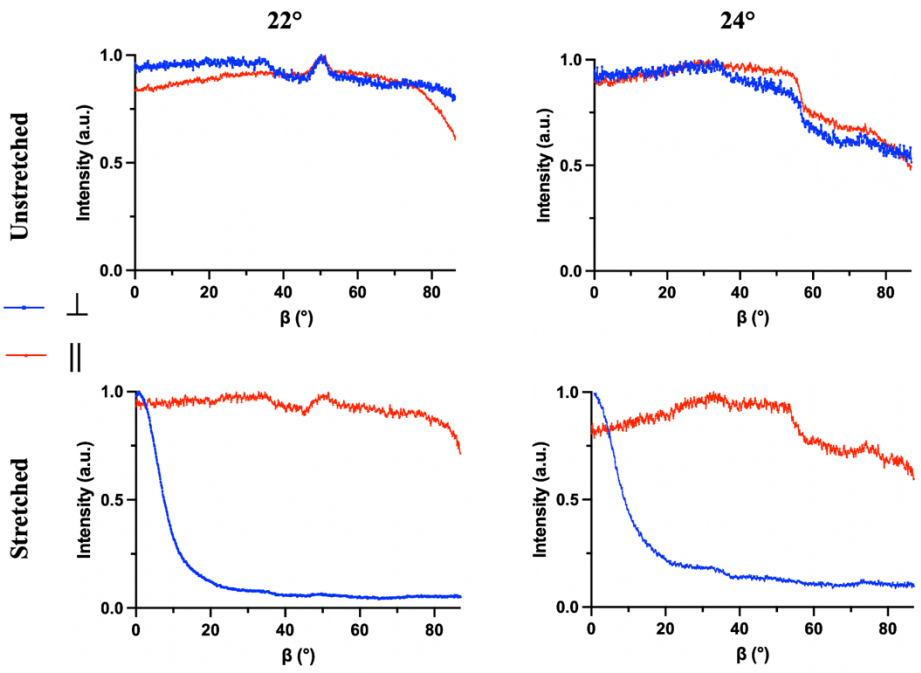

Fig. 3.47 Intensity of Debye-Scherrer ring at 2θ of 22° and 24° as a function of azimuthal angle β depending on orientation of sample to X-ray beam for 1:1 and 1:6 filaments.

To assess crystal c-axis orientation in individual fibers, the XRD-derived alignment $f_{overall}$ was normalized by the alignment of fibers in filaments f_{fiber}. Fig. 3.48 shows the respective f_{fiber} values for 1:1 and 1:6 filaments, with 1:6 possessing great anisotropy (with unity equating to complete alignment along the filament axis). 1:1 fiber alignment was not completely isotropic, as might have been expected in an unstretched sample. The slight alignment could have resulted from the light tugging of fibers during deposition on the dynamic wire collector and from the subsequent removal of the filament from the collector. It should be noted that the filaments imaged in SEM used to calculated f_{fiber} were separate from those analyzed by 2D XRD to calculate $f_{overall}$. Fortunately, fiber orientations examined in SEM displayed a very small SD, mitigating the concern regarding orientation heterogeneity in filaments subjected to the same degree of stretch.

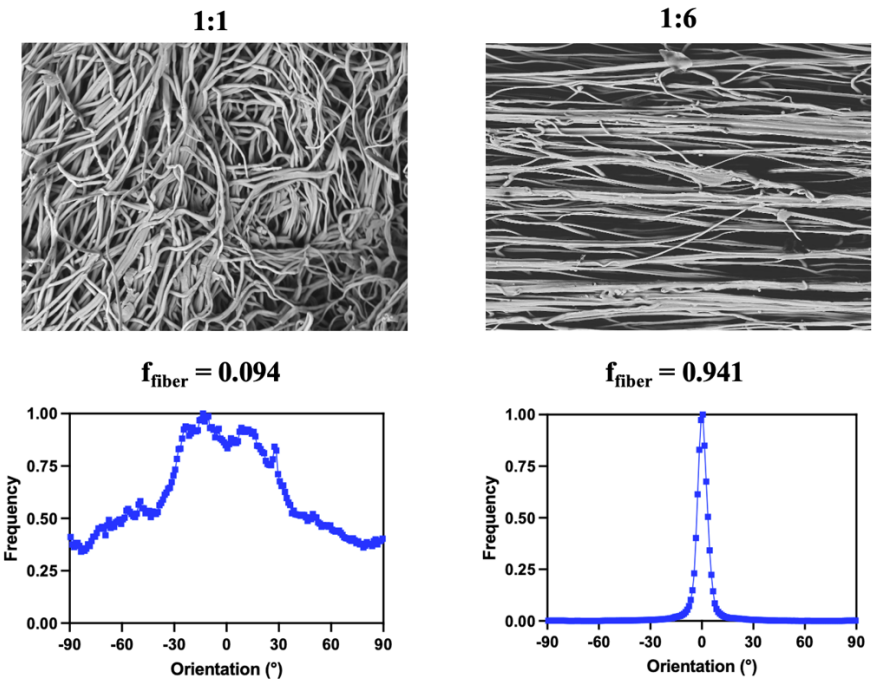

Fig. 3.48 SEM images (500x magnification) of 1:1 (left) and 1:6 (right) filaments with corresponding Herman's orientation factor for fiber orientation and associated orientation distribution.

$f_{crystal}$, representing crystal alignment within a fiber, as well as the XRD and SEM-derived orientation factors used to calculate $f_{crystal}$, are presented in Table 3.3. $f_{crystal}$ was 0.050 for 1:1 filaments and 0.631 for 1:6 filaments. This suggests that within a stretched microfiber, crystals are highly aligned, but not for unstretched fibers. These results are analyzed in greater depth in Section 4.5.1.

Measuring $f_{crystal}$ for filaments with completely random fiber deposition is not possible; f_{fiber} would be zero, rendering $f_{crystal}$ undefined, even though fibers may contain some degree of crystal alignment. The slight fiber anisotropy of my 1:1 filaments enabled calculation of $f_{crystal}$, but the accuracy of this deconvolution remains compromised by the low f_{fiber} as a result of near-random

deposition. Further investigation of filaments stretched to various degrees would be useful in strengthening confidence in the present results, as well as better understanding orientation progression.

Sample	**$f_{overall}$ [XRD]** (n=1)	**f_{fiber} [SEM]** (n=3)	**$f_{crystal}$**
Unstretched (1:1)	0.005	0.094 ± 0.045	0.050
Stretched (1:6)	0.593	0.941 ± 0.043	0.631

Table 3.3 Herman's orientation factor f for unstretched and stretched samples.

3.6 Viscoelasticity

Fig. 3.49 displays DMTA curves for filaments stretched to varying degrees, with the temperature range for the plots confined to -90 °C to 10 °C. This range was set to exclude measurement discontinuities at lower temperatures and the effects of epoxy melting at higher temperatures. The epoxy securing the filaments in the DMTA softened at around 10 °C (Fig. 3.50), impacting thermomechanical measurements beyond this point. As a result, melting onset analyses could not be reliably conducted in these experiments.

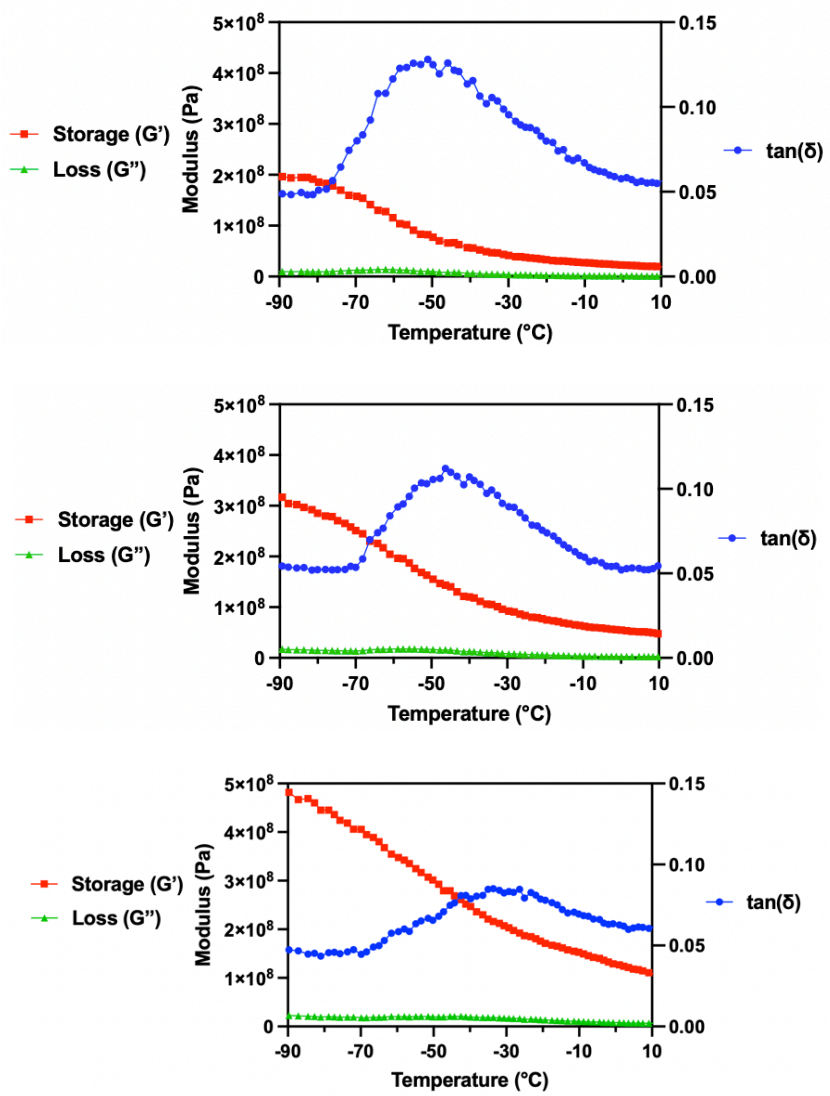

Fig. 3.49 DMTA curves for 1:1, 1:3, and 1:6 filaments (from top to bottom).

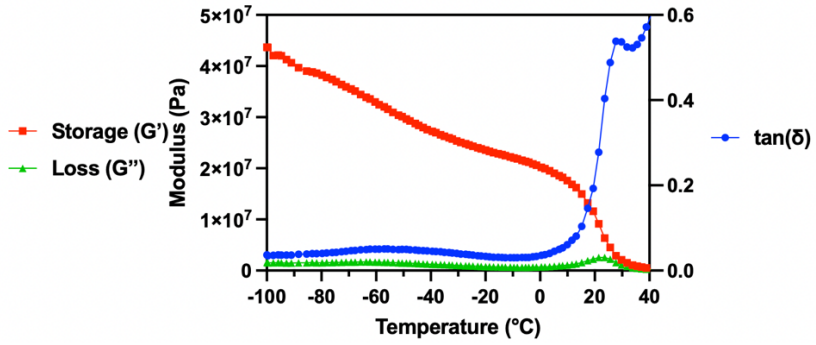

Fig. 3.50 DMTA curve for rapid Araldite epoxy.

The curve shape and peak location of 1:1 reflected findings in literature on PCL (*103*, *104*). However, a minority of the curves for stretched filaments did not exhibit prominent $tan(\delta)$ and G'' peaks, as expected for semicrystalline polymers. The lack of discrete T_g peaks may be due to experimental limitations; it is possible that the epoxy's added rigidity at cold temperatures may have caused the sample to slip from the DMTA clamps.

As shown in Table 3.4 and Fig. 3.51, average T_g increased from -59.13 ± 6.03 to -37.84 ± 9.96 °C upon stretching from 1:1 to 1:6, whereas the height of the $tan(\delta)$ peak decreased from 0.13 ± 0.01 to 0.08 ± 0.01.

Sample	**T_g via $tan(\delta)$ peak [°C] ($tan(\delta)$)**	**T_g via G'' peak [°C]**	**Average T_g [°C]**
1:1	-54.87 ± 2.51 (0.13 ± 0.01)	-63.39 ± 1.92	-59.13 ± 6.03
1:3	-41.05 ± 7.17 (0.10 ± 0.01)	-53.62 ± 3.85	-47.34 ± 8.89
1:6	-27.88 ± 5.22 (0.08 ± 0.01)	-47.80 ± 6.26	-37.84 ± 9.96

Table 3.4 T_g, measured using either the $tan(\delta)$ or G'' peak, of filaments stretched to varying degrees. Peak $tan(\delta)$ values where T_g was identified included in parentheticals.

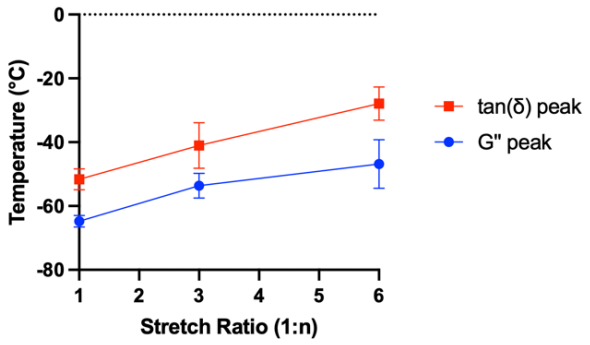

Fig. 3.51 T_g calculated based on the peak temperature of $tan(\delta)$ (red) or G'' (blue), as a function of stretching.

While the $tan(\delta)$ peak shifted upwards with stretch, its FWHM remained constant (Table 3.5). A wider $tan(\delta)$ peak reflects energetic heterogeneity in molecular mobility, as the varying proximity of amorphous chains to dispersed crystals modulates the energetic barriers to segmental motion within the interconnected network. Thus, the consistency of this FWHM provides further evidence that X_c remains constant through stretching.

Sample	**FWHM [°C]**
1:1	42.21 ± 2.23
1:3	37.97 ± 4.65
1:6	41.21 ± 2.51

Table 3.5 FWHM of $\boldsymbol{T_g}$ measured from $\boldsymbol{tan(\delta)}$ peak for filaments stretched to varying degrees. FWHM calculated by fitting Gaussian curve to peak.

4. Discussion

4.1 Microfiber Morphology

Starting the discussion at the fiber level, SEM revealed three notable phenomena impacting PCL fiber diameter as a result of stretching. First and most patently, stretching strained the fiber and reduced its diameter. However, this strain was not uniformly distributed. Unstretched islands — regions retaining the original 1:1 thickness despite the stretching of adjacent segments — emerged along the fiber axis due to necking. This is highlighted by the red circle in Fig. 3.5 within the 1:2 micrograph. It is suspected that necking is initiated in the amorphous region due to its relative flexibility, allowing for stress concentration that is then transferred to nearby crystalline regions. During this process, polymer crystals can also undergo plastic deformation akin to atomic solids through mechanisms such as slip, twinning, and martensitic transformations, though only intermolecular bonds are disrupted in polymeric plastic deformation, not covalent bonds (*105*). The necked islands, visible from 1:2, disappeared by 1:4 as the islands themselves became elongated. This observation correlates with Fig. 3.6, where

maximum fiber alignment was reached at 1:4. Additional stretching primarily resulted in fiber narrowing rather than further alignment. Excessive strain also caused breakage and subsequent random directional fraying. Put differently, extensive stretching up to fracture reduced net alignment.

Secondly, stretched filaments exhibited bifurcations — regions where one fiber transitions into two — as depicted in Fig. 3.5. It is difficult to tell from these static images whether bifurcations represent fiber splitting or joining upon stretching. In either case, the radius for a single 'parent' fiber R would follow conservation of volume when composed of two smaller 'child' fibers with radii a and b:

$$R = \sqrt{a^2 + b^2}$$

The bifurcation depicted in Fig. 3.5a followed the above relation. However, in Fig. 3.5c, the parent strand and supposed child strands did not follow this relation. This parent strand was too small to account for the child strand diameters. This, along with 1:1 SEM micrographs, indicate that some bifurcations were not necessarily a result of stretching and were instead artifacts of electrospinning deposition. Fig. 3.5b shows splitting of coalesced ribbons, for which this expression does not apply, as the ribbons were not cylindrical.

This brings us to the last of the three phenomena — coalescence. In contrast to narrowing, coalescence of fibers into wider ribbons increased average width. Coalescence may have resulted from the local increase in temperature when the mechanical work of plastic deformation converted to heat, causing adjacent fibers to melt together. Badami et al. found that an increase

in draw ratio from 1:3 to 1:5 increased the temperature of necked nylon-66 up to 120 °C depending on the drawing rate (*106*).

From a theoretical standpoint, the increase in temperature that causes fibers to coalesce together can be estimated using energy conservation. Assuming an adiabatic system:

$$W_{stretch} = Q$$

where W = work from stretching, and Q = heat energy released. Rewritten:

$$F * d = m * C_p * \Delta T$$

where F = force required to stretch, d = distance stretched, m = sample mass, C_p = specific heat capacity, and ΔT = temperature change. The calculated ΔT is likely an overestimate, as this expression does not account for local elastic energy stored in polymer chains nor heat dissipation to the surrounding environment.

Literature reports PCL's C_p to be about 2000 $\frac{J}{kg*°C}$ at RT (*107–109*). The magnitudes of the specific heats calculated using my DSC data are consistent with this literature value (*110*):

$$Cp\ \left[\frac{J}{kg * °C}\right] = \frac{\frac{dQ}{dt}\,[mW]}{m\,[mg] * \frac{dT}{dt}\ [\frac{°C}{s}]} * 1000\ [\frac{g}{kg}]$$

where dQ/dt = heat flow, and dT/dt = heating rate.

ΔT is estimated using the energy conservation equation with approximated constants based on my experimental observations:

$$(1\ N) * (0.5\ m) = (10^{-5}\ kg) * \left(2000\ \frac{J}{kg * C°}\right) * \Delta T$$

The calculated value of ΔT is 25 °C. This means that at RT (20 °C), an estimated temperature of ~45 °C would be reached upon stretching. DSC analysis revealed that PCL began to melt at temperatures as low as 40 °C, as indicated by the pre-peak for both pellets and unstretched filaments. This suggests that coalescence during stretching may result from the melting of less stable crystals with a T_m around and below ~45 °C. This hypothesis is further supported by SEM data that exhibits the effects of sequentially increasing the stretch ratio by one unit (i.e., from 1:2 to 1:3, 1:5 to 1:6). Both 1:2 (Fig. 3.3) and cold-stretched 1:5 filaments (Fig. 3.13) presented a fine microfibrous architecture with no noticeable coalescence. However, their architecture diverged when stretched one unit greater at RT. Stretching from 1:2 to 1:3 led to coalescence. Conversely, stretching these 1:5 filaments to 1:6 at RT presented no coalescence. This discrepancy suggests that unstretched and low-stretched filaments possess specific microstructural features that facilitate coalescence, namely unstable crystals whose lower temperature melting initiates coalescence.

In addition to strain-initiated coalescence, ambient coalescence (i.e., without strain) was observed in the multifilament stored at RT (Fig. 3.17). For the multifilament, coalescence likely results from gradual amorphous rearrangement rather than from the melting of unstable crystals, as RT is above PCL's T_g and below the pre-peak melting onset temperature. However, in ambient conditions, crystal transformation can still occur. Even without heat dissipation from plastic deformation, unstable crystals may rearrange into more thermodynamically stable structures, if the kinetic conditions allow so. Other potential mechanisms of ambient crystal transformation include trans-esterification (*111*), Ostwald ripening (*112*), and chain scission through humidity-induced hydrolysis — all of which could affect X_c and the entanglement

environment. Which specific microstructural changes take place in PCL at ambient conditions remains poorly understood. In future experiments, measuring X_c throughout aging could help clarify the extent to which ambient coalescence is driven by amorphous versus crystalline rearrangements.

Overall, SEM showed that fibers do not simply narrow uniformly upon stretching, but exhibit greater complexities such as unstretched islands, bifurcations, and coalescence.

4.2 Theories on Polymer Crystals

Transitioning from the fiber to crystal level, my data from DSC, XRD, and DMTA was used to build a microstructural, chain-based model for the observed crystal transformations following stretching. This section first discusses the crystal morphologies introduced in Section 1.4.2 — CEC and CFC. With a focus on crystal stability and strain-induced mechanisms of deformation, this theoretical contextualization provides a framework upon which my model is based. Finally, my proposed model is presented in Section 4.2.2.2. The experimental data supporting this model is detailed in Section 4.4 onwards, bolstered by thermodynamic theory and other experimental findings from literature.

It is important to note that CEC and CFC are not just theoretical conjectures. Multiple studies have confirmed that PCL crystallizes into both morphologies (*113–116*), most using small angle X-ray scattering (SAXS), a technique which allows for long period and lamellar thickness determination.

4.2.1 Thermodynamics of Crystal Morphologies

From a thermodynamics perspective, for a polymer with uniform Mw, a fully extended CEC morphology represents the lowest free energy state, i.e., equilibrium state (*51*, *117–120*). Lindenmeyer showed this through modeling the free energy of a crystal made from a single polymer chain, altering only the number of chain folds, i.e., crystal thickness (*121*). While crystallographic folding increases intramolecular energy due to bending strain, it also decreases intermolecular energy by an amount proportional to the length of chain brought into the crystal. The assumptions involved in Lindenmeyer's model included crystallization from a monodisperse melt, consideration of variations in only conformational energy (not vibrational nor electronic), no defects, and chain end exclusion from the crystal. Based on these assumptions, the canonical-ensemble partition function Z for the single-chain crystal can be written as:

$$Z(X,\zeta,T) = z_n \sum_f 2(|R|+1)e^{-E(X,\zeta,f)/kT}$$

where z_n = partition function for molecular vibrations, and E = energy of crystal system, as follows:

$$E(X,\zeta,f) = E_f f + \zeta E_c (f+1)$$

subject to the condition that

$$X = \zeta_f f + \zeta(f+1) + R$$

where X = number of segments in the molecule, ζ_f = number of segments in a fold, ζ = crystal thickness (in units of chain segments), E_f = energy per fold, E_c = crystal cohesive energy per segment, f = number of folds per molecule, and R = portion of the chain not included in the crystal. This does not take into account the interfacial energy between the amorphous and crystalline phases. Plotting the Helmholtz free energy as a function of crystal thickness, Lindenmeyer found that the lowest free energy conformation was when crystal thickness

corresponded with the full chain length, i.e., a completely extended chain. However, there were also subsidiary minima which corresponded to a crystal containing folds. Such minima indicate that the chain can remain in a metastable state if there is not sufficient energy to overcome the activation barrier to reaching a fully chain-extended crystal.

In theory, CFC will melt at a lower temperature than CEC, when applying Lindenmeyer's assumptions. The melting point of an ideal CFC is determined by the balance between the stabilizing bulk free energy of the crystal and the destabilizing surface free energy of chain fold insertion (*122*). This is expressed through the Gibbs-Thomson effect (*120*):

$$l\frac{\Delta h_f}{T_M^0}(T_M^0 - T_M) = 2\sigma_e$$

where l = lamellar thickness, Δh_f = heat of fusion per unit volume, T_M^0 = equilibrium melting point of an extended chain crystal, and σ_e = excess surface free energy. With a larger σ_e, T_m lowers. This effect also suggests that smaller crystals (lower l) melt at lower temperatures.

While no studies exist that investigate T_m differences between CFC and CEC in PCL, experimental findings on other semicrystalline polymers tend to reflect these ideal thermodynamic predictions of morphological stability (*41*, *47*, *122*, *123*). For example, Wunderlich's DSC examination of melting point variations in CFC and CEC for linear high polymers found that the former had a lower T_m (*51*). For example, measurements of PE revealed CFC melted between 80 and 135 °C, whereas CEC melted at 141 °C. Although PCL was not specifically tested by Wunderlich, PCL is a linear high polymer, so it may exhibit greater CEC thermal stability as observed by his study.

Lindenmeyer's theory agrees that, given equal crystal thickness, fully extended crystals are enthalpically favorable to those with chain folds due to additional fold surface energy this incurs (*47*, *122*). However, the applicability of this theory is challenged when considering a crystal in a system with more than one chain. In a multi-chain system, CFC is more entropically favorable because the surrounding amorphous chains can take on a greater number of conformations (i.e., more microstates). For CEC, chains above and below the crystal are more constrained because a greater fraction of these chains extend from and attach to the crystal.

In reality, formation of a crystal comprised of chains fully extended from end to end (i.e., the most extreme case of CEC) would require extensive untangling and rearrangement of chains. This poses significant kinetic and energetic barriers that are practically unattainable. Thus, the morphology that arises at a particular environment is most often that with the greatest growth rate rather than the lowest free energy. Depending on the environmental conditions, such as pressure, rate of cooling, mechanical forces, and initial phase prior to crystallization (i.e., melt, solution), crystals can exhibit different morphologies. In the case of PE, from melt, CEC formation required elevation of pressure to as much as 3000 atm (*52*). From solution, crystallization of PE under elevated pressures did not yield CEC. Thermodynamics are important in understanding driving forces and crystal stability, but kinetics are a necessary consideration when evaluating the likelihood a particular crystal structure forms.

The thermodynamics and kinetics of crystal transformation are also significantly mediated by the stress field induced via stretching. The next section describes possible mechanisms underlying how strain influences deformation in polymer networks.

4.2.2 Stretch-Induced Crystal Transformations

4.2.2.1 Literature

Stretching semicrystalline polymers can cause crystal transformation (*14*). A large body of literature on polymer crystals grown from the random state (i.e., melt, solution) concludes that nucleation via chain folding drives the formation of CFC (*52*). When subjecting the random state to tensile stress, several studies have observed the formation of CEC, confirmed via electron diffraction (*124*).

Electrospinning has also been found to produce a CEC fraction in a variety of polymers due to the tensile forces the polymer jet is subject to (*125*, *126*). In polyoxymethylene (POM) ES nanofibers, Kongkhlang et al. found that dissolving the fibers then recasting them as a film transformed the original CEC into CFC, underscoring the powerful influence stretching has on crystal morphology (*125*). CEC and CFC produce unique FTIR spectra for POM, which allowed Kongkhlang to make such a conclusion. In general, for crystallization from macromolecular melt and solution, CEC are more likely to form through secondary extension in the solid state after initial chain folding crystallization (*52*). These observations indicate that the application of an external strain field lowers the free energy of CEC nucleation below that of CFC. On the chain level, the degree of coiling in a semicrystalline network decreases when strained, encouraging the formation of multi-chain fibrillar nuclei (associated with CEC crystallization) rather than single-chain lamellar nuclei (associated with CFC) (*127*).

While the term ‘fibril’ generally refers to an aligned crystalline bundle, this is rather vague. Depending on the source, ‘fibril’ refers to one of two distinct microstructures. Some studies use

the term to describe parallel-stacking of highly stretched chains, analogous to CEC (*128*), while other studies use it to describe fragmented lamellae connected by tie chains along the fibril axis (*129*, *130*). Broadly speaking, the former is said to result from lamellar unfolding, whereas the latter results from intra-lamellar shear, separation, and rotation. While the formation of highly oriented fibrils from randomly packed lamellae has been observed during stretching (*131*), which of the two microstructures such fibrils correspond to, as well as the formation mechanism, remain unclear from the literature. An atomic force microscopy (AFM) study on the surface morphology of PCL nanofibers by Lim et al. provides an example of this uncertainty (*29*). The micrographs presented a fibrillar topology parallel to the fiber axis on only stretched fibers. Lim concluded that the fibrils were composed of lamellae stacked along the fiber axis. While possible, they provided no molecular evidence to support this claim. They also illustrated extended amorphous chains in their microstructural model within these fibrils, but did not discuss potential CEC contribution, for which extended amorphous chains can be a precursor. This ambiguity surrounding the microstructural basis of fibrils found across literature warrants further investigation.

Although the deformation mechanisms underlying stretching of semicrystalline polymers have been studied extensively both theoretically and experimentally, there remains a lack of consensus as to which mechanism is accurate. For cold-drawing, which refers to stretching of the solid state rather than melt or solution, the most popular hypothesized mechanisms include lamellar fragmentation (*132*, *133*), stack rotation (*134–136*), melt recrystallization (*70*, *128*, *131*), and amorphous extension (*137*). Some studies suggest simultaneous occurrence of these phenomena (*138*), while others posit sequential incidence as stretching progresses (*128*, *139*).

Beginning the discussion with lamellar fragmentation and rotation, several mechanisms with varying levels of plausibility have been theorized, as summarized by Walczak (*41*). These mechanisms are based on crystallographic slip, which involves the sliding of one block over another via dislocation movement. Matsumoto et al. proposed that lamellae break down non-uniformly in a staggered staircase-like transformation (Fig. 4.1c) (*140*). Other theories include complete extension of chains at the crystal face (Fig. 4.1a) proposed by Kobayashi, as well as tilting of lamellae towards the stretch axis in the case of more uniformly distributed stress across the crystal (Fig. 4.1b) proposed by Peterlin. Matsumoto's staggered breakdown seems most energetically probable, as Kobayashi's complete extension would require greatest amounts of force without disrupting intermolecular bonds in the crystal bulk, and Peterlin's tilting would require high temperatures to soften these rigid lamellae. Tilting also presents a more gradual breakdown, which does not correspond to the dramatic changes in the diameter of necked specimens observed by literature and my SEM results.

Building off Matsumoto, Peterlin et al. developed the *fibrillar transition model*, where crystalline lamellae shear then break down into 'mosaic blocks' during plastic yielding (*136*). Then, these blocks stack to form microfibrils connected by tie chains. It is the modular, non-continuous fragmentation of lamellae in the fibrillar transition model which may underlie the abrupt change in diameter characteristic of necking. Peterlin stated the exterior of the microfibrils may also be covered in a layer of extended chains over several block lengths. Horizontal connections may develop between fibrils due to secondary lamellar crystallization. Given that this model is based on crystallographic slip, mosaic blocks should remain the same thickness as the parent lamellae

from which they originated. However, it is commonly reported that the long period of fibrils changes depending on the temperature at which the polymer is drawn (*136*), calling into question Peterlin's model and leading some to argue that crystal slip alone is not sufficient to describe the microstructural deformation observed during stretching.

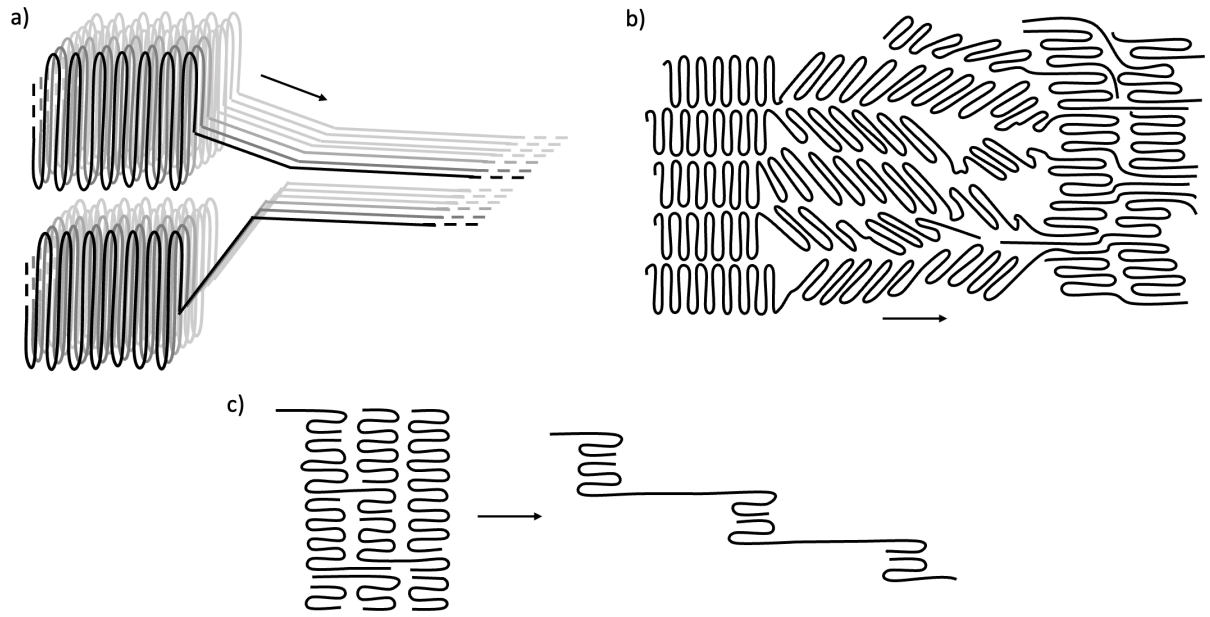

Fig. 4.1 Possible stretched-induced lamellar deformation mechanisms, proposed by a) Kobayashi, b) Peterlin, and c) Matsumoto ***(41)***. b) is not to be confused with the fibrillar transition model (not depicted), as Peterlin was involved in developing both mechanisms.

Many suggest that crystallographic slip is followed by melt-recrystallization during cold-drawing (*128*, *131*, *138*). Slip is said to first take place during yielding, after which CEC form as a product of melt-recrystallization during necking. During the transformation from CFC to CEC, this two-step mechanism suggests a highly disordered intermediate state with a lower X_c, analogous to melting (*136*). For strain-induced melt-recrystallization, 'melt' describes the destruction of original crystals. Even if the system does not reach T_m, the term 'melting' is apt as it reflects the cooperative breaking of inter/intra-molecular interactions that compose a

crystalline structure (*136*). 'Recrystallization' refers to the construction of new crystals under the coupling of thermal fluctuations and tensile stress (*131*). Strain-induced melting occurs at local segments rather than homogenously across the entire material, so the overall material remains solid. Because this melting occurs in an undercooled condition, chain relaxation is limited and thereby promotes accelerated recrystallization onto nuclei comprised of extended chains. In Flory's mechanism for stretch-induced recrystallization in high network polymers, he proposed that growth of existing crystals occurs simultaneously with nucleation, with chains attaching both laterally and longitudinally (*46*).

As with lamellar fragmentation, the chain level mechanism for melting during stretching is also unclear. Mechanically, melting can take place via the unfolding and pulling out of folded chains from CFC (*141*). Thermally, melting is promoted via stretch-induced self-heating and depression of T_m. For self-heating, the material temperature can increase during plastic deformation, particularly in necked regions, due to the heat dissipated from mechanical work. In addition, tensile stress can cause negative hydrostatic pressure that results in lowering of T_m, thereby increasing the thermodynamic drive to melt (*136*). These mechanical and thermal phenomena may occur simultaneously during melting, although the relative contribution of each to melting is not yet known.

Not all researchers agree that crystal slip precedes melt-recrystallization. Séguéla's 2003 review of existing literature on strain-induced deformation concluded that slip can occur at all strains, whereas melt-recrystallization and chain unravelling are restricted to larger, post-yield strains (*136*). However, a more recent 2023 study by Zhou et al. on molecular dynamics simulations of

stretch-induced crystal transformations found that depending on crystal size, Séguéla's claim was not always true (*138*). In Zhou's simulation, small crystals melt-recrystallized at lower, pre-yield strains.

Many theories exist on the structural mechanisms for strain-induced crystallization. None of the theories presented are confirmed universal truths for all semicrystalline polymers, but rather hypotheticals based on thermodynamics and experimental data on polymers other than PCL.

4.2.2.2 Proposed Mechanism

The mechanism with which strain-induced microstructural evolution takes place within Biolig's ES PCL microfibers is proposed in Fig. 4.2. Lamellar fragmentation and melt-recrystallization form the basis of this model. To begin, the unstretched filament contains randomly oriented CFC and CEC, albeit a significantly greater CFC fraction. Some CEC may be present in the unstretched filament due to polymer jet elongation during electrospinning. At low strains, CFC experience crystal slip and fragment into smaller blocks and amorphous chains uncoil and extend in the strain direction. Unstable crystals also melt-recrystallize. At high stains, CFC chains are pulled out and unfold (i.e., melt), and amorphous chains continue to elongate. These unfolded and extended chains align to form new, or join existing, CEC oriented along the stretch axis. Post-drawing may also cause the terminal amorphous segments of existing CEC to align and contribute to CEC lengthening along the stretch axis. As CFC shrink in width due to fragmentation, CEC grow longer. Existing CEC can also serve as nucleation zones for amorphous chains to join the crystals laterally. In addition to changes in crystal size and orientation, stretching results in greatly increasing the CEC fraction. Thus, in comparison to

unstretched filaments dominated by CFC, stretched filaments contain two distinct crystal populations, CFC and CEC, with different thermodynamic stabilities.

My proposed mechanism is likely a simplification, as it does not take into account mixed crystals (e.g., shish-kebab structures) nor crystal defects. Even so, this model encompasses the overall shift in crystal morphology from one extreme to another during stretching.

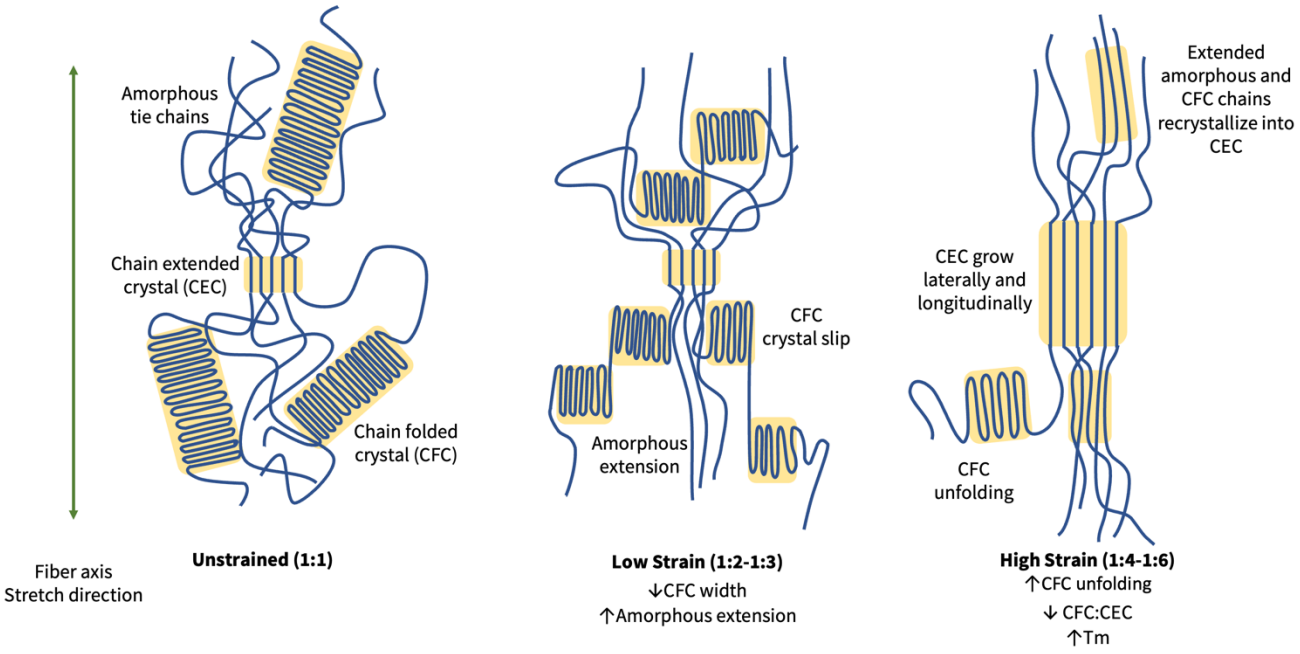

Fig. 4.2 Schematic of chain evolution upon stretching ES PCL microfiber. Yellow shading represents crystalline regions. Melt-recrystallization of unstable pre-peak crystals not included in the Low Strain graphic.

Multiple studies investigating PCL fibers have demonstrated that stretching promotes the extension of amorphous chains which act as a precursor to CEC recrystallization. A study on melt-spun fibers by Mochizuki et al. identified the presence of extended amorphous chains through tensile testing (*96*). Stretching increased fiber tenacity, which they attributed to an increase in extended amorphous chains and CEC. High-resolution SEM imaging of the fiber

surface confirmed the presence of CEC, which they suspected were formed via unfolding of CFC. In another study on melt-spun fibers, Selli et al. fitted simulated diffraction patterns to the fibers' 2D XRD profiles (*25*). The best-fit simulation included a highly oriented mesophase, which was defined as a non-crystalline phase more ordered than a random amorphous state, i.e., an extended amorphous fraction. This led them to conclude that strained PCL must contain this mesophase. They suspected that the mesophase existed around and in-between crystals, comprised of load-bearing extended tie chains. Finally, Brennan et al. showed via polarized Fourier transform infrared (FTIR) spectroscopy on ES fibers that both amorphous and crystalline phases became more aligned when stretched (*142*). An amorphous region with greater alignment corresponds with extension of amorphous chains. Through stretching, Brennan found that both phases first became less aligned to the stretch axis before increasing in alignment again. The non-linear relationship between orientation and stretch was theorized to reflect unfolding of CFC (decreasing alignment) followed by recrystallization of CEC (increasing alignment). While individually each of these studies lacks sufficient evidence to definitively determine the deformation mechanism and final morphology of strained PCL fibers, together these studies offer persuasive evidence that stretching extends amorphous chains which then form CEC.

Experimental findings from stretched fibers of other semicrystalline polymers also closely parallel my proposed mechanism. Using SAXS and wide angle XRD, a detailed study on strained poly(butylene succinate) (PBS) deduced the following: CFC fragmenting near the yield point, CFC chains freeing into the amorphous region, and a portion of these chains extending in the stretch direction and crystallizing into CEC (*19*). Furthermore, a simulation of PE-carbon nanotube nanocomposites demonstrated that fragmentation and melting co-occurred at low

strains (*138*); specifically, they observed fragmentation of larger crystals while smaller crystals melted. At high strains, amorphous chains recrystallized and merged into larger crystals. While PCL is not specifically investigated in these studies, their findings serve as relevant touchstones given the shared focus on semicrystalline polymers under strain. For some polymers, the CEC and CFC crystal phases can be detected by shifts in FTIR bands (*50*). However, no such band shifts have been identified for PCL, as morphology-dependent shifts are based on transition dipole-dipole coupling theory, detectable in polymers having tight helical skeletal conformations (*53*). Fortunately, a variety of other experimental techniques can be employed to investigate the microstructural evolution of strained PCL.

My study aims to contribute to this nascent body of research by employing additional experimental methods that no one study on ES PCL microfibers has yet to do in conjunction — namely DSC, XRD, and DMTA. The following results from my experiments not only generally align with these studies but also provide novel insights.

4.3 Crystallinity

There is not a sufficient body of research on stretched PCL fibers to discern whether a consistent relationship between X_c and stretching exists. My study did not find any influence of stretching on DSC-derived X_c, whereas other studies on PCL fibers generally report that X_c increases upon stretching. However, these studies present inconsistent results as to whether the X_c monotonically increases. Mochizuki measured continuous X_c increase (via XRD) when melt-spun fibers (300 um diameter) were stretched up to 1:9 (*96*). Contrarily, Brennan measured a decrease in X_c (via FTIR) when ES fibers (0.5 um diameter) were stretched to 1:3, after which X_c increased when stretched to 1:4 (*143*). These variable results may be due to the differences in

fiber diameter as well as experimental design, including fabrication technique and instrumentation used to measure X_c.

In contrast to the DSC results, the XRD-derived X_c increased with stretch (Fig. 3.43). A potential explanation lies in the detection limits of XRD. In the DSC profile of unstretched filaments, a pre-peak was observed, which likely reflects the melting of unstable crystals. It is possible that these crystals were too small (see Section 4.4.2) to produce a detectable diffraction peak, leading the XRD-derived X_c calculation to underestimate the true value for unstretched filaments. Stretching may have facilitated crystal perfection, transforming less stable pre-peak crystals into more stable Peak 1 crystals. This transformation could account for the absence of the pre-peak in highly stretched filaments. Additionally, in non-powder samples like filaments, not all crystal orientations may be detected in XRD, thereby reducing the diffracted intensity and consequently causing an underestimation of X_c.

Different X_c values are often reported within an individual study depending on the instrument from which the calculation is based. One study on poly(aryl-ether-ether-ketone) (PEEK) films found that, as compared to the true X_c determined via density measurements, DSC overestimated X_c up to 18% due to competitive phenomena between melting and recrystallization of the polymer during DSC heating (*144*). In the same study, XRD reportedly underestimated X_c up to 11% due to the broad amorphous halo that obscured crystalline peaks. Another study on PCL melt-spun filaments stretched to varying degrees found a similar instrumental trend, reporting a greater DSC-based X_c than that of XRD by about 10 percentage points across all samples (*25*).

Although quantitative values may differ between instruments, relative X_c comparisons from a particular instrument remain valuable.

It is also possible X_c differs on the surface and interior of the fiber. The interior experiences slower solvent evaporation following spinning. This could result in greater X_c by increasing chain mobility and allowing more time for chains to rearrange into thermodynamically stable arrangements (*31*). On the other hand, slower solvent evaporation also provides more time for chains to relax into coiled, entropically favorable arrangements, resulting in a greater interior amorphous fraction (*21*). Slower evaporation most commonly promotes crystallization (*145*), although it remains to be determined whether this is the case for PCL. Interior and exterior crystals might also possess different morphologies due to heterogeneous crystallization environments. Non-uniformity of X_c across the fiber diameter could result in steep changes in mechanical behavior if degradation occurs through surface erosion.

4.4 Thermal Analyses: Stretch-Induced Crystal Population

DSC was used to investigate the crystalline character of PCL microfibers at various processing stages, from as-received pellet to filament stretched to varying degrees. The shape of DSC curves can be compared across samples to uncover the mode through which polymer chains evolve through processing. Three prominent trends emerged from stretching, as illustrated by the curves in Fig. 3.18 and Fig. 3.19: i) lower temperature pre-peak disappeared, ii) height of Peak 1 (~60 °C) shortened slightly, and iii) Peak 2 (~70 °C) grew. Peak 1 refers to the tall peak that exists in all filaments, representing the original crystal population. Peak 2 refers to the stretch-induced secondary endotherm, representing the newly developed crystal population. The disparate temperatures at which melting occurred indicate that these peaks represent crystal

populations with distinct thermal stabilities. Thermodynamic stability can be influenced by crystal morphology and/or size, although DSC data alone is not sufficient to determine to what extent each of these factors define the differences in T_m. As will be detailed in the following sections, XRD and DMTA data provide key evidence for the formation of CEC during stretching. More broadly, DSC's primary contribution in informing my model is in exhibiting significant microstructural changes during stretching. First, I show that what is detected by DSC is reflective of the samples' original structure, rather than experimental artifacts. Then, the DSC results are analyzed by considering the effects of crystal size and morphology on stability.

4.4.1 Experimental Susceptibility

The literature presents contradicting accounts of the origin of double endotherms in DSC scans, be it a product of measuring technique or different crystal populations related to sample history. Blundell and Osborn proposed the former — that double endotherms are not representative of polymer morphology at RT nor processing history, but rather a result of continuous melting and recrystallization during the DSC heating ramp-up (*146*). Blundell's study examined unstrained, molded PEEK that was isothermally crystallized at different temperatures. When measured in the DSC, all samples exhibited double endotherms, with an upper endotherm that always appeared at the same temperature. However, the lower endotherm shifted, always 10 °C greater than the temperature of isothermal crystallization. Blundell proposed that the lower endotherm was associated with crystals formed during isothermal treatment, whereas the stable upper endotherm was characteristic of repeated polymer behavior during the DSC ramp up (*15*). The upper endotherm was said to form from melt-recrystallization, where low stability, imperfect crystals melt during DSC ramp up, then recrystallize into more stable crystals with thicker lamellae. (This temperature-induced melt-recrystallization is not to be confused with *strain-induced* melt

recrystallization introduced in Section 4.2.2.1.) Blundell claimed the upper endotherm represented the thermal point at which the temperature was too high for recrystallization of melted imperfect crystals to take place.

However, Basset et al. disagreed with Blundell, claiming that the double peaks represented two separate crystal morphologies formed at different times during isothermal treatment, with the lower endotherm associated with a less stable crystal phase (*42*). While Basset and others in this school of thought do not dispute the possibility of modest reorganization of crystals when using a slow DSC heating rate, they believe the upper endotherm is comprised of primary crystals present at RT and *not* of recrystallized crystals from DSC heating. It is argued that the area under the lower endotherm is too small to account for the melting of an entire crystalline fraction formed during isothermal treatment. Basset hypothesized that the upper endotherm was associated with a primary lamellae framework that forms in an unrestricted environment (*147*). The lower endotherm was said to represent secondary, lower stability crystals that formed in a constrained environment between existing lamellae. Such restrictions made it more likely for these crystals to take on non-ideal structures.

While my study examined polymers that were stretched rather than isothermally treated, the theories for double endotherms can still be considered. Blundell's theory, where the secondary endotherm is a product of melt-recrystallization during DSC heating, does not fit well with the DSC curves of my progressively stretched filaments. Peak 2 was not observed in my unstretched samples. Extending Blundell's reasoning, stretched filaments could contain metastable crystals that unstretched filaments do not, in which case Peak 2 is a result of the metastable crystals'

melt-recrystallization. On the other hand, Peak 2 could also reflect an original crystal feature unique to stretched filaments. In my study, stretching caused Peak 2 to extend to higher temperatures. This disagrees with Blundells' argument that the second endotherm represents the maximum threshold temperature for recrystallization, which remained at a constant temperature across his experiments. Basset's theory is more plausible, where Peak 2 is characteristic of a separate, more stable crystal population resulting from stretching, rather than an artifact of DSC heating. To test this hypothesis, the following subsections detail my experimental evidence proving that Peak 2 was neither a result of metastable structural melt-recrystallization during DSC heating nor from changes in sample-pan contact.

4.4.1.1 Metastability with Heating Rate

For both the pellet and filaments, the shape of their DSC profiles changed upon using different heating rates (Fig. 3.38, Fig. 3.40). This curve transformation means that at some heating rates, what is measured by the DSC deviates from the original structure. Mathot discussed how the faster a sample is heated, the closer the measurement is to its original structure (*148*). Fast heating rates allow unstable structures present in the original sample to be detected by suppressing kinetically-limited processes such as melt-recrystallization (*149*). The kinetic barrier to melting is created at the melting front where there is competition between melting and its reverse process of recrystallization (*150*). At slower heating rates, the kinetic barrier is lowered, and metastable structures can undergo crystal perfection via melt-recrystallization during DSC ramp up (*151*). Moreover, a faster heating rate increases measurement sensitivity, improving detection of lower energy transmissions.

The drawback of faster heating rates is that sensitivity comes at the expense of accuracy via thermal lag. The effect of thermal lag is observed by peak broadening and a shift upwards in T_m (*90*, *152*). A faster heating rate can push melting onset upwards via superheating, where only parts of the crystal are at a temperature above the melting point. Thermal lag is proportional to heating rate, mass, and specific heat capacity, as described by Newton's Law of Cooling (*149*):

$$\Delta T_{lag} = R_0 \frac{dQ}{dt} = R_0 (C_{p,sample} * m_{sample} + C_{p,pan} * m_{pan}) \frac{dT}{dt}$$

where R_0 = thermal resistance between the sample and sensor, dQ/dt = heat flow to the sample, Cp = specific heat capacity, m = mass, and dT/dt = heating rate experienced by the sample and pan. Toda et al. uses a separate 1D heat diffusion approximation to characterize how sample properties contribute to the thermal lag (ΔT_{lag}) experienced (*153*):

$$\Delta T_{lag} = \frac{\rho \, C_{p,sample} \, L^2}{2\kappa} \frac{dT}{dt}$$

where ρ = sample density, κ = thermal conductivity, and L = sample height.

For the pellet and 1:1 filament, the absence of the pre-peak from scans taken at slow heating rates indicates that melt-recrystallization takes place. During this process, the overlapping of the melting endotherm and recrystallization exotherm might obscure the pre-peak. By suppressing melt-recrystallization using high heating rates, unstable structures such as the pre-peak are captured by the DSC. However, the effect of thermal lag was observed by the slight increase in peak temperature when using a heating rate of 25 versus 2 °C/min — 65.7 versus 61.3 °C, respectively. Still, the overall takeaway is that the original structure, specifically the unstable crystals that make up the pre-peak, are best preserved at higher heating rates with the slight measurement penalty of thermal shifting.

Turning to the stretched samples in Fig. 3.40 (right plot), Blundell's theory suggests that Peak 2 is the result of melt-recrystallization of either i) metastable crystals unique to stretched filaments or ii) Peak 1 crystals. Neither of these hypotheses explain my results. First, if metastable crystals unique to stretched filaments existed, a lower-temperature endotherm would be present only at high heating rates at which crystal reorganization is suppressed. No such endotherm is observed. Second, if Peak 2 was the result of Peak 1's melt-crystallization, the slowest heating rate would produce the largest Peak 2 relative to Peak 1. This is the opposite of what was observed. The relative height of Peak 2 grew closer to that of Peak 1 with greater heating rates, indicating that the kinetic process of melting for these two crystal populations is not the same. The greater effect heating rate had on Peak 2 means the activation energy to initiate melting is lower for Peak 2 crystals than those of Peak 1. This provides convincing evidence that Peak 1 and 2 represent distinct crystal populations with different melting kinetics. Overall, my data best fit with Basset's theory that Peak 2 represents higher stability crystals that originate from the sample's morphology at RT.

Interestingly, studies have reported that CEC do not undergo melt-recrystallization (*120*, *154*, *155*). The consistent presence of Peak 2 across all heating rates shows that Peak 2 crystals do not undergo melt-recrystallization. If this were the case, Peak 2 would shift to higher temperatures with slower heating. This observation serves as one clue that Peak 2 may represent CEC.

4.4.1.2 Sample-Pan Contact

Using a higher heating rate (Fig. 3.40 (right plot)) and decreasing sample-pan contact (Fig. 3.23) produced similar results in stretched samples: a taller Peak 2. These experimental variables

yielded comparable results because heating rate is nearly proportional to DSC heat flow (see Section 3.4.3). As for why a taller Peak 2 was observed for samples with decreased pan contact, two hypothetical explanations relating to heating rate are presented.

First, with worse contact, the sample might experience greater thermal lag and thus a lower heating rate overall than what was reported by the DSC. This could allow for crystal perfection via melt-recrystallization of less stable Peak 1 crystals into more stable Peak 2 crystals, where existing Peak 2 crystals can serve as nuclei. In this case, a larger Peak 2 is expected at lower heating rates because crystal perfection is less kinetically inhibited. Yet the opposite was observed at lower heating rates, as shown in Fig. 3.40. It is possible that melt-recrystallization still took place but was difficult to detect at low heating rates due to decreased signal sensitivity. However, the relative height of Peak 1:Peak 2 was greater at low heating, rendering this hypothesis unlikely.

The second hypothesis is, in a sense, the inverse of the former: samples with incomplete pan contact may experience a greater heating rate in later stages of melting. Stretched filaments experienced significant contraction upon heating (Fig. 3.38). This contraction may have initially led to decreased contact and slowed the rate of heating experienced by the sample in these early heating stages, exacerbating the effects of incomplete sample-pan contact. Contact may have improved once the sample started to melt and flow onto the base upon passing through Peak 1's thermal range. This would have increased the heating rate experienced by the sample, while the DSC program's calculation of heat flow carried on assuming the same heating rate throughout measurement. Thus, it is possible that during DSC heating ramp up, both stretched filament

contraction and sample flow on the pan base affect sample-pan contact and subsequent Peak 2 height. In line with Fig. 3.23, contraction most likely occurred in Peak 1's thermal range, after which melt-flow onto the pan base prevailed when the DSC temperature progressed past Peak 2. This second hypothesis aligns more with my data, but it is not clear the exact temperature at which the transition from contraction to flow takes place.

While the specific mechanism behind the increase in Peak 2 magnitude with heating rate and contact remains unclear, the sustained presence of this peak under various DSC measurement conditions is a notable discovery. This consistency confirms that Peak 2 is an inherent characteristic of stretched filaments, rather than an artifact of the instrumentation.

Regarding the greater stability of Peak 2 crystals compared to Peak 1, factors such as crystal volume and morphology are primary considerations. Next, the significant impact of volume on stability is explored before delving into additional factors.

4.4.2 Volume

Thermodynamics explain how crystal volume relates to T_m. The free energy per unit volume of the crystalline (G'_c) and melt (G'_l) state can be characterized as follows:

$$\boldsymbol{G'_c = H'_c - TS'_c}$$

$$\boldsymbol{G'_l = H'_l - TS'_l}$$

Compared to the crystalline state, the melt, with no long-range order, has a less favorable enthalpy (H) and a much greater entropy (S). An additional term G_s can be added to the crystalline free energy to represent the surface free energy per crystal. For a crystal with volume V, the total free energy of the crystalline state (G_c) per crystal can be written as follows:

$$\boldsymbol{G_c = G'_c V + G_s}$$

For the sake of illustration, these expressions can be applied to a perfect tetragonal crystal with height h and width w, depicted in Fig. 4.3:

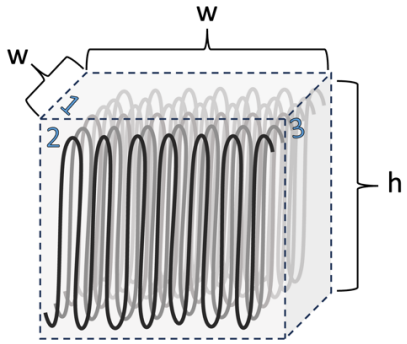

Fig. 4.3 Perfect square lamellar crystal with height *h* and width *w*.

G_s can be written using μ_1, μ_2, and μ_3 to represent the energy-per-surface area coefficients for the chain-folded crystal face and the two variants of chain-extended crystal faces, respectively:

$$\boldsymbol{G_c = G'_c V + \mu_1(2w^2) + (\mu_2 + \mu_3)(2wh)}$$

μ_1 is greater than μ_2 and μ_3 because the former surface faces both entropic and enthalpic penalties from conformational restriction and bending strain, respectively.

The lowest temperature at which melting is possible is when the free energy of the crystalline and melt state are equivalent, where G_l is the total free energy of the melt state:

$$\boldsymbol{G_l = G_c}$$

This can be rewritten in terms of free energy per unit volume, assuming the moles of polymer in crystal volume V remain the same as that of its liquid melt with volume V:

$$G'_l \mathrm{V} = G'_c \mathrm{V} + G_s$$

Solving for T after plugging in the enthalpy and entropy terms detail the relationship between temperature and surface free energy, where a greater G_s contribution results in a lower T_m:

$$(H'_l - TS'_l)V = (H'_c - TS'_c)V + G_s$$

$$H'_l - H'_c - TS'_l + TS'_c = G_s/V$$

$$T = \frac{\Delta H - G_s/V}{\Delta S} = \frac{\Delta H - G'_s}{\Delta S}$$

Small crystals possess a greater G'_s, surface free energy per unit volume of crystal. Hence, the temperature at which the free energy of the melt and crystal are equal, i.e., the melting temperature, is lower the smaller the crystal is. This is also described by the previously mentioned Gibbs-Thomson effect. The higher free energy renders small crystals more metastable with respect to larger crystals (*51*). When kinetic parameters allow, small crystals will reorganize into larger crystals.

This theoretical basis can be used to compare how crystal volume changes with stretch within a specific crystal population. With greater degrees of stretch, the breadth of Peak 2 increased, indicating that crystals within this new population grew with stretch (Fig. 3.19). For samples with different Mw, stretched 190k filaments had a greater Peak 2 width than that of 110k (Fig. 3.32), indicating that the new crystal population in 190k presented a wider size distribution. With no difference in X_c based on Mw (Fig. 3.25), the Mw-discrepancy in Peak 2 size distribution could be because 110k may start off with a relatively greater proportion of small crystals due to shorter chain lengths. These crystals could act as restriction points that make it more difficult for chains to rearrange into larger crystals upon stretching. It would be necessary to quantify the

number and size of crystals for each Mw to confirm this postulate, which was out of the technical scope of this present study.

In addition to variability in volume, crystal defects also contribute to endothermic broadening. The insertion of a defect poses competing thermodynamic effects — unfavorable enthalpic and favorable entropic changes — which can widen the distribution of stabilities within a crystal population. With both crystal size and defects affecting peak breadth, it is difficult to determine the extent to which each contributes.

Overall, the thermal range an endotherm spans for a specific crystal population (i.e., Peak 1 or Peak 2) suggests how crystal size distributions differ across samples. However, it is important to differentiate size distribution from absolute size. While progressive stretching increased the width of Peak 2, indicating that larger Peak 2 crystals formed with stretch, it is not possible to conclude that Peak 2 crystals are larger than Peak 1 just because Peak 2 crystals had a higher T_m. This is because thermodynamic stability is not only governed by crystal volume, but also crystal morphology.

4.4.3 Morphology

Stretching induced significant crystal transformations in the Biolig fibers, as evidenced by the emergence of a secondary endotherm (Peak 2) at a higher temperature compared to the original endotherm (Peak 1). These strain-induced structural changes are quantified in Fig. 3.20, which presents the melting enthalpy associated with each subpeak — a measure reflective of the relative quantity of each crystal population. Peak 2 crystals began to form only after stretching to 1:4, with their proportion increasing as the Peak 1 fraction diminished. The relationship between

these transformations at high strains remains unclear. It is not definitively known whether the original Peak 1 crystals directly converted into Peak 2 crystals, or if the reduction in the Peak 1 fraction occurred simultaneously with the formation of Peak 2 crystals due to other concurrent phenomena.

Because there are nearly no published studies on PCL stretched post-collection that include DSC analysis, it is not yet possible to externally validate these double endotherm observations. Only one relevant DSC experiment, by Selli et al., was found on stretched PCL melt-spun fibers, which did not present a secondary endotherm (*102*). Selli's fibers achieved a similar elongation to those in my study. However, the single endotherm in their results suggests minimal crystal transformation. Therefore, plastic deformation may occur through different mechanisms in our respective samples. This variation likely stems from our divergent fiber manufacturing processes — Selli's melt-spinning versus Biolig's electrospinning. Primary crystallization is predominantly thermally induced and occurs during cooling in melt-spinning, while in electrospinning, crystallization predominantly results from solvent evaporation. Additionally, Selli's melt-spinning produced fibers with larger diameters. These variations may yield fibers with dissimilar degrees of crystal orientation and subsequent distinct responses to tensile stress. In fibers with a low orientation, the initial response to stretching involves the uncoiling and alignment of amorphous chains prior to significant crystal deformation. Conversely, fibers with initially higher crystal orientation are prone to earlier stress-induced crystal transformations during stretching. Accordingly, it is possible Selli's fibers possessed a lower crystal orientation, as they exhibited less crystal transformation upon stretching. Unfortunately, comparing crystal orientation between our studies is challenging, as Selli employed a different method for

calculating orientation. Analyzing microstructural features across different fiber manufacturing techniques is a complex task involving many variables. Other researchers are encouraged to further investigate and validate my novel findings in ES PCL fibers.

Other semicrystalline polymers have exhibited a higher temperature secondary endotherm following stretching (*156*, *157*). Tang et al. investigated how various degrees of stretching affect the crystallization behavior of PVDF hollow fiber membranes (*20*). Stretching past 1:1.5 generated a beta (TTTT) crystalline phase, as confirmed by FTIR and wide angle XRD, and increased overall degree of X_c. As the stretching ratio increased, the secondary endotherm became more prominent and shifted to higher temperatures. Tang suggested the new peak was evidence of the beta phase, which has a higher T_m than that of the original alpha (TGTG') phase. As for my study, PCL is a polyester, not fluoropolymer like PVDF, so crystalline phase changes based on trans-gauche transformations are not applicable. Nonetheless, it is relevant to note that stretching can cause a novel crystal population to develop, visible as a secondary endotherm in DSC. Moreover, Zhang et al.'s investigation on the effect of uniaxially stretching PBS also exhibited the development of a secondary peak in DSC (*19*). The double endotherms were hypothesized to reflect two separate crystal populations, CFC and CEC, as confirmed by observing changes in long period with SAXS. Because PBS and PCL are both thermoplastic semicrystalline polyesters, it is reasonable to anticipate comparable findings in PCL. Microdifferential thermal analysis of PE at different pressures also exhibited double peaks (*123*). At atmospheric pressure, a single melting peak representing CFC was observed. For slow-cooled samples prepared at 3000 atm, two melting peaks were recorded. Fracture surface morphology images were used to confirm that the lower temperature peak represented CFC and the higher

peak represented CEC. Although no other DSC studies have been performed on stretched ES PCL microfibers, the results of my study sit in parallel with experiments on ES fibers made from other polymers which exhibited secondary endotherms.

Analyzing how the secondary endotherm evolves with stretching temperature also elucidates the mechanism of crystal deformation. It is notable that Peak 2 for the 1:5 Cold filament was much smaller than that of 1:5 RT (Fig. 3.35). Tensile plastic deformation likely takes place through a combination of amorphous extension and crystalline deformation, where CFC melt-recrystallize into CEC. Given constant X_c (Fig. 3.36), the smaller Peak 2 in cold-stretched samples means less crystal transformation takes place. At lower temperatures, crystals are more stable due to a reduction in molecular vibrational amplitude, which strengthens intermolecular forces contributing to crystal cohesivity. Hence, the filament extension under cold conditions can be primarily attributed to the amorphous region absorbing most of the tensile load. Conversely, for RT-stretched filaments, the larger Peak 2 reflects greater crystal transformation, indicating that strain-induced melt-recrystallization is more dominant at warmer stretch temperatures.

4.5 Diffractive Analyses: Dimensions and Alignment

Joining my XRD results with DSC provides a more detailed understanding of crystal evolution upon stretching. To clarify the terminology for the present discussion, width (i.e., wide, narrow) refers to horizontal dimensions of a crystal perpendicular to the molecular c-axis, while length (i.e., long, short) refers to the vertical dimension parallel to the c-axis.

4.5.1 Crystal Orientation

1:6 filaments produced significantly distinct azimuthal scans depending on the orientation of the filaments to the X-ray beam (Fig. 3.46). This indicates strong crystal anisotropy within stretched

samples. Fig. 4.4 illustrates a simplified schematic of the direction of diffraction off the characteristic (110) and (200) planes of aligned crystals in 1:6 filaments, depending on the filament orientation. These characteristic planes are presented in Fig. 4.5. When the X-ray beam was oriented along the filament axis (∥), scattering from the full angular range was recorded. In contrast, when the beam was perpendicular to the filament axis (⊥), only OOP diffraction was recorded for 1:6 filaments. Together, these observations suggest stretched filaments contain crystals with their c-axis aligned parallel to the fiber axis. In the ∥ case, the uniform azimuthal rings resulted from scattering of aligned crystals rotated about their c-axis with no radial preference, whereas in the ⊥ case, the beam encountered (110) and (200) planes tilted various degrees away from the beam source throughout the rotation of crystals about their c-axis, producing OOP diffraction spots.

These azimuthal observations were normalized to the orientation distribution of fibers within the filament, as shown in Table 3.3. The orientation factor for 1:6 filaments indicated strong alignment, whereas 1:1 filaments did not. This shows that crystals, whether pre-existing or newly formed due to strain, tend to align along the fiber axis during stretching. The rearrangement of crystals along the stretch axis requires interpenetrating amorphous chains to bear the initial tensile load, whose extension may serve as nucleation sites for CEC that are also subsequently aligned with this axis.

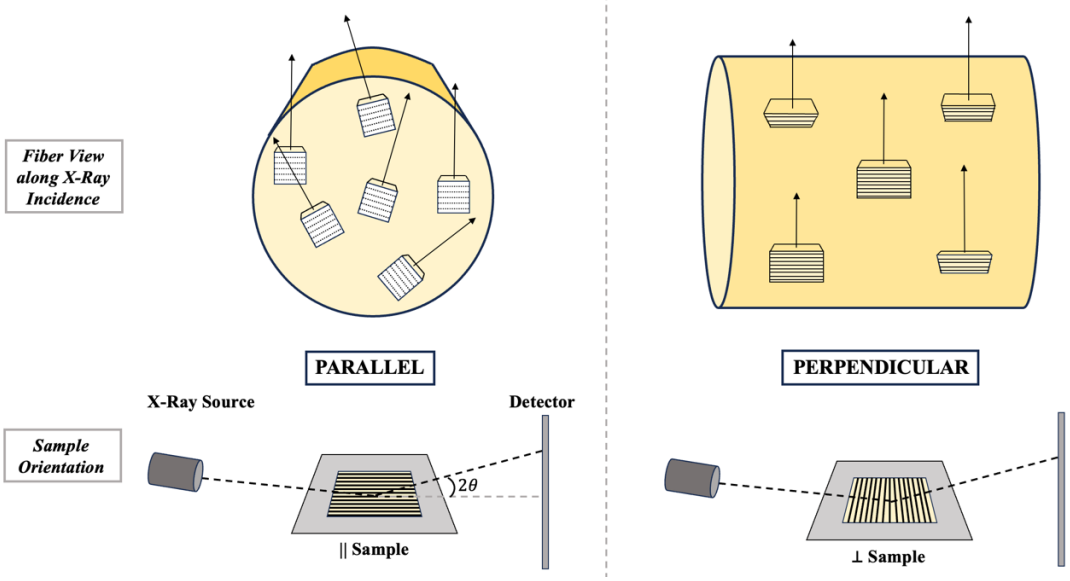

Fig. 4.4 Schematic of (top) X-ray scattering vector off planes of crystals with c-axis preferentially aligned to fiber axis and (bottom) filament orientation relative to beam in grazing incidence 2D XRD.

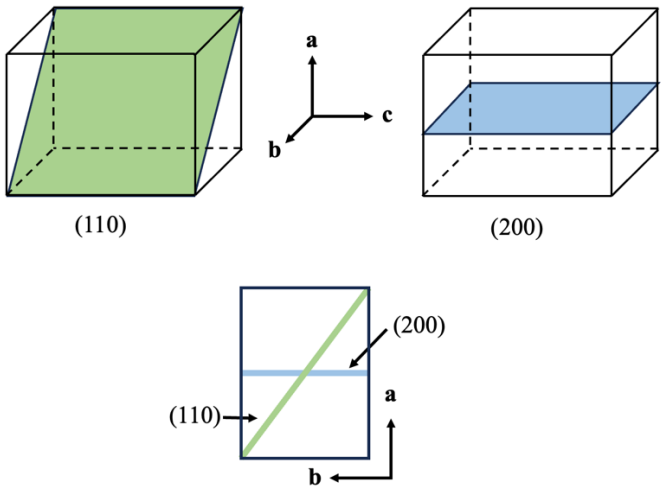

Fig. 4.5 Characteristic crystal planes of PCL that present diffraction peaks in XRD. Note: Unit cell not drawn to proportion. Based on Lozano-Sánchez et al. (***158***).

Quantifying crystal orientation in hierarchical materials poses various layers of potential error. At the filament scale, the filaments placed in the XRD holder may not have been aligned

perfectly parallel to one another, potentially obscuring the detected anisotropy, quantified by $f_{overall}$. At the fiber scale, some fibers may have been frayed and tangled in regions not captured by the sampling of SEM micrographs used to calculate f_{fiber}.

Another source of potential error on the micro-level was that crystal orientation might have also differed on the fiber surface and interior. Diffraction occurs through all layers of the filament, so it was not possible to disentangle these potential radial differences in microstructure. The polydispersity of fiber diameters can also confound orientation results, as crystal orientation may differ for fibers with different diameters (*58*). Larger fibers occupy a greater mass of material and contribute more signal, skewing the average orientation. Crystal alignment might be greatest on the exterior of the fiber, or the 'polymer skin', as found by Zussman et al (*159*). The skin carries the brunt of stress during spinning, allowing the interior solution to experience relatively less stress and exhibit lower anisotropy (*88*). Although my study did not examine variations between the fiber surface and interior, existing literature indicates that exploring these distinctions could be useful in understanding the molecular structures on which degradation initiates.

While 2D XRD extracts an average orientation estimate that is a convolution of several factors, this information is still useful in indicating that stretching induces significantly greater crystal alignment. Crystal alignment can result in an anisotropy of properties, such as increased stiffness and strength along the molecular axis (*160*).

4.5.2 Crystal Size

Stretching, as demonstrated by DSC analysis, clearly led to the formation of a new and more stable crystal population in the PCL filaments. XRD-derived Scherrer calculations showed that the average horizontal dimensions of the crystals decreased upon stretching, as shown in Fig. 3.44. Together, these observations suggest that stretching may reduce the width of the original crystals or result in the formation of new crystals that are narrower than the original. Both these possibilities could also occur simultaneously. Because Scherrer calculations provide only an average width for all crystals in the sample, it is challenging to pinpoint which specific crystal population(s) contribute to the overall horizontal shrinkage upon stretching. Applying mechanical reasoning can help provide plausible explanations for these dimensional transformations.

Tensile stress transforms CEC and CFC in different manners. 2D XRD showed that there is strong crystal alignment to the fiber axis in stretched samples, so we will now consider the theoretical effect of stretching crystals along their chain axis. For CEC, stretching can lengthen the crystal due to terminal amorphous chains joining the crystal from its top and bottom ends. The effect of stretching on CEC width is less clear. CEC might narrow if chains at the edge of the crystal are pulled out, while widening could occur if nearby amorphous chains join the crystal laterally. For CFC, stretching can cause narrowing through both fragmentation and unfolding. It is unlikely stretching lengthens or widens CFC. Lengthening of CFC would pose a large enthalpic barrier requiring complete rearrangement of all inter-segment bonds of the crystal interior. A narrowing fiber diameter could theoretically push CFC blocks closer together to merge at lamellar interfaces and grow wider. However, given that the DSC showed the

development of crystals with significantly greater stability upon stretching, it is unlikely that lateral merging of CFC would account for such an increase in stability. The decrease in interfacial energy by CFC merging is much less significant compared to that of CEC longitudinal growth. This is because the decrease in interfacial energy from favorable intermolecular interactions is proportional to chain length, given a sufficiently long chain.

Consequently, it is plausible that fragmentation and unfolding of CFC contribute to the observed average narrowing of crystals upon stretching. Fragmentation is likely to be the dominant mode of crystal narrowing at low strains, as the fraction of Peak 1 crystals remained constant up to 1:4 (Fig. 3.20). At high strains past 1:4, the fraction of Peak 1 crystals decreased as that of Peak 2 increased. The decrease in the original crystal fraction was likely a result of strain-induced melting via lamellar unfolding.

Whether CEC also contributed to average narrowing is unclear, particularly due to competing dynamics: CEC can narrow if chains are pulled out, whereas incorporation of amorphous chains into CEC can cause widening. It is unclear if CEC can form from amorphous extension alone, independent of the unfolding of CFC. It is likely that such unfolding eases amorphous extension, as CFC melting would decrease the constraints experienced by amorphous chains during rearrangement.

Some studies have found that stretching results in simultaneous narrowing and lengthening of polymer crystals (*53*, *96*). For example, Mochizuki et al.'s study on melt-spun PCL fibers found that the crystal length along the fiber axis increased when stretched to 1:9 (*96*). Interestingly, this

study, which uniquely identified a (0 0 14) peak, also noted that the width and volume of the crystals decreased upon stretching. Applying these findings to my study suggests that strain-induced Peak 2 crystals may be volumetrically smaller than Peak 1 crystals. This is possible if Peak 2 crystals possess a more stable morphology than that of Peak 1, where the morphological stability of Peak 2 crystals compensates for the instability incurred by a lower volume. While proof of volumetric shrinkage upon stretching would further substantiate that each subpeak represents distinct crystal morphologies, I was unable to confirm this in my study due to the absence of a peak with a non-zero l-index.

Overall, my DSC and XRD findings indicate that stretching promotes the formation of crystals with greater thermodynamic stability and decreases average crystal width. Coupled with the understanding that unfolding of CFC and uncoiling of amorphous chains may increase the CEC fraction, these observations suggest that CFC are likely associated with Peak 1 and CEC with Peak 2.

4.5.3 Lattice Parameter

XRD peak shift calculations showed an increase in the *a*, *b* horizontal lattice parameters upon stretching. One might expect these parameters to decrease when a crystal stretched along its c-axis, as my experimental results have established that crystal width shrunk, as well as fiber diameter. It would intuitively follow that the distance between adjacent polymer chains (i.e., *a*, *b* lattice parameters) also decreases.

This apparent paradox can be explained by several potential phenomena. During crystal deformation, interchain distances may increase due to mechanisms such as crystal slip, unfolding

of CFC, and the formation of other non-ideal intermediate structures. Additionally, tensile forces may directly stretch the a- or b-axis of crystals that are not perfectly aligned with the stretch axis. However, it is more likely the amorphous fraction of the polymer network bears most of the tensile load, owing to its greater flexibility compared to the crystalline regions. Whether stretching the unit cell directly is mechanically feasible with the forces exerted during manual stretch can be estimated using Young's modulus (E):

$$E = \frac{\sigma}{\varepsilon} = \frac{F/A}{\varepsilon}$$

where σ = stress, ε = strain, F = force applied along the a-axis, and A = cross-sectional area of the crystal normal to the tensile direction. Because E for a PCL polymer crystal could not be found in the literature, a general E was used to reflect the general magnitude of single polymer crystals noted in the literature, around 5 GPa (*161*). ε can be taken from one of the samples in Fig. 3.3; stretching the filament from 1:1 to 1:5 results in a unit cell strain of $4.2*10^{-3}$ in the a-direction. The diameter of an unstretched filament ($8*10^{-4}$ m) can be used to estimate the total cross-sectional area by dividing by 2, assuming a symmetrical crystal with 50% X_c. This yields A = $2.51*10^{-7}$ m^2. Substituting these values into the equation above:

$$5\ GPa = \frac{\frac{F}{(2.51 * 10^{-7})\ m^2}}{4.2 * 10^{-3}}$$

Solving for F gives 5.28 N. Because F is a reasonable value for manual stretching, this estimation suggests that direct tensile extension of the crystalline unit cell parameters is physically possible. Still, the substantial crystal transformation observed in DSC suggests that destructive mechanisms requiring local chain rearrangement, such as chain unfolding, are more likely the primary drivers of increasing horizontal lattice parameters, rather than direct stretching of the unit cell.

4.6 Viscoelasticity

Preceding the discussion on viscoelasticity, it is important to clarify the term 'stretched', as all samples are cyclically stretched within the DMTA apparatus, while some filaments are also stretched prior to DMTA analysis. 'Stretched' is used to refer to this latter case, as it has been through the thesis.

Analyzing the thermally modulated viscoelastic nature of filaments via DMTA offers clarity on underlying microstructure. Let us first contextualize the thermodynamic basis for why the temperature at which $tan(\delta)$ peaks in the DMTA curve corresponds to T_g. $tan(\delta)$ represents a ratio of energy dissipation to energy storage. Unlike melting, there is no change in intermolecular bonding during the glass transition. Below T_g, the polymer system is in a glassy state where molecular mobility is highly restricted. As temperatures increase and approach T_g, chains in the amorphous regions exhibit increased segmental motion, both torsional and translational. An energy barrier must be overcome for amorphous chains to relax to lower energy states. If the barrier is not successfully surpassed, the energy input is dissipated as heat instead of transforming into mechanical work. As temperature exceeds T_g, $tan(\delta)$ decreases because the activation energy is almost always overcome at higher temperatures, as described by the Arrhenius equation. Stated differently, the remaining proportion of chains in a glassy state diminishes as T_g is surpassed, reducing the glassy-to-mobile transitional contribution to energy dissipation. T_g is also affected by the molecular orientation of polymer chains. For stretched filaments with greater chain orientation and extension, T_g rises due to increased chain stiffness and reduced mobility. Compared to amorphous polymers with no orientation, polymeric fibers with high degrees of molecular orientation have been found to yield a T_g 30 °C higher (*162*).

DMTA measurements showed a significant increase in T_g as samples were stretched (Fig. 3.51). Given T_g is a parameter that relates to the amorphous region, its stretch-induced increase indicates amorphous chain extension. This supports the hypothesis that stretching leads to the formation of CEC, as amorphous chain extension acts as a precursor to CEC formation.

In addition to extension, T_g may rise due to the constraining effects of nearby crystalline regions on the molecular mobility of adjacent amorphous regions. Crystals act as barriers that curtail amorphous chains from transitioning from a rigid to a more flexible state. While the DSC results showed that overall X_c was not altered by stretching, it is possible that the new strain-induced crystals pose a greater barrier to molecular motion than the original crystals. When comparing such a barrier presented by CEC versus CFC, there is a clear difference in the freedom of their terminal chains, which exist in both the crystalline and amorphous state. Chains exiting CEC face spatial restrictions in their amorphous movement across all three axes (apart from chains bordering the crystal exterior). In contrast, chains exiting CFC face no restriction along the axis parallel to the normal of the crystal face, as illustrated in Fig. 4.6.

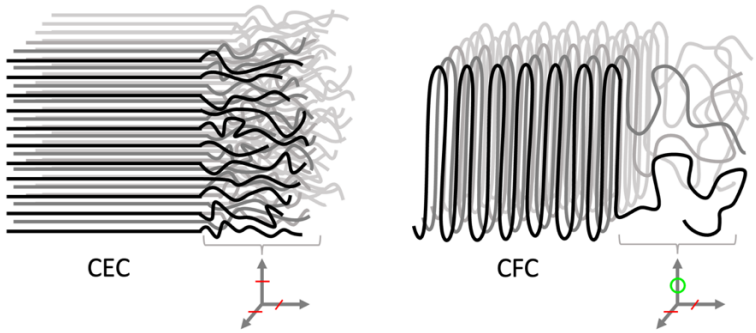

Fig. 4.6 Chains exiting crystalline region for CEC (left) and CFC (right) with axes that experience restricted molecular movement marked in red and non-restricted marked in green.

In 1:6 filaments, in addition to the upwards shift of the $tan(\delta)$ T_g peak, this peak was also shorter along the y-axis (i.e., a smaller change in $tan(\delta)$ going through T_g). A shorter peak indicates lower levels of energy dissipation during the glass transition. This can reflect a lower amorphous fraction in the material, but because X_c was constant regardless of degree of stretch (via DSC), this explanation is inapplicable. Instead, the shorter $tan(\delta)$ peak could be further evidence that the amorphous fraction is less coiled in stretched filaments. If amorphous chains in 1:6 filaments are more extended, the amplitude of segmental motion can be reduced due to the more rigid nature of elongated chains. This rigidity can decrease the maximum energy dissipation possible during glass transition, thereby lowering peak $tan(\delta)$.

To summarize, both the higher T_g and lower $tan(\delta)$ maximum in stretched filaments may be attributed to greater amorphous chain extension. When the DMTA applies a cyclic tensile force on a filament at a temperature around its T_g, either i) elastic energy is stored in the chains (associated with greater G') or ii) energy is dissipated during plastic deformation (associated with greater G''), where chains change conformation after overcoming an energy barrier. Elastic storage is greater in stretched filaments because further plastic deformation is more energetically costly for chains that are already extended. For stretched filaments, intrachain bonds bear the tensile load, whereas for unstretched filaments, tension disrupts interchain interactions within coiled amorphous chains. The extended, restricted character of the amorphous regions in 1:6 filaments explains why these filaments present a greater storage modulus G' (i.e., lower maximum $tan(\delta)$) whilst requiring greater T_g temperatures to enter a rubbery state.

The proposition that amorphous chains are more extended and contain greater elastic potential energy in 1:6 filaments compared to 1:1 is also supported by hot plate experiments. As shown in Fig. 3.1, only 1:6 filaments contracted upon heating. On a microstructural level, as T_m is approached during heating, amorphous chains take on lower entropy conformations by coiling, thereby shrinking the overall sample. The amorphous chains in 1:1 filaments presumably possessed more relaxed conformations and subsequently did not experience a thermodynamic drive to coil further. The fact that 1:6 filaments did not elastically recoil back into their original shorter length directly after stretching indicates that crystal rearrangement takes place during stretching. Initiation of plastic crystal transformations such as CFC unfolding at high strains can maintain the filament's elongated state at RT. Contraction of stretched filaments only happens at elevated temperatures where there is sufficient thermal energy to overcome the enthalpic barrier to achieving a relaxed, coiled conformation.

4.7 Simplified Structure of Microfiber

A simplified schematic of the microfibers' structural hierarchy is presented in Fig. 4.7, using fiber diameter data from SEM, and crystal size and lattice parameter data from XRD. The maximum number of crystals that fit across a fiber's diameter is presented as the fibril count. The true value is likely below this when considering the contribution of amorphous chains and defects.

Fibrils are used for the schematic because they have been observed in polymer fibers via AFM and 2D SAXS (*67*, *130*, *163*). Such techniques were out of the scope of my study, so the presence of fibrils in the Biolig fibers cannot presently be confirmed. Fibrils are most likely present, if at all, in stretched fibers, resulting from tensile stress along the fiber axis. My results

suggest that the strain-induced crystal population represents CEC aligned to the stretch axis. Tie chains exiting CEC experience greater lateral constraint than chains exiting CFC (Fig. 4.6). Thus, when CEC are present, crystals are more likely to connect to adjacent crystals along the fiber axis, chaperoning the formation of fibrils.

Fibrils are unlikely to exist in unstretched fibers, as evidenced by low crystal alignment via 2D XRD. The schematic use of fibrils in the unstretched fiber, while likely an inaccurate morphological representation, is employed only to compare the relative sizes of crystals between sample types.

The number of chains extending across a fibril, or the (200) horizontal crystal width, was calculated using lattice parameter *a*.

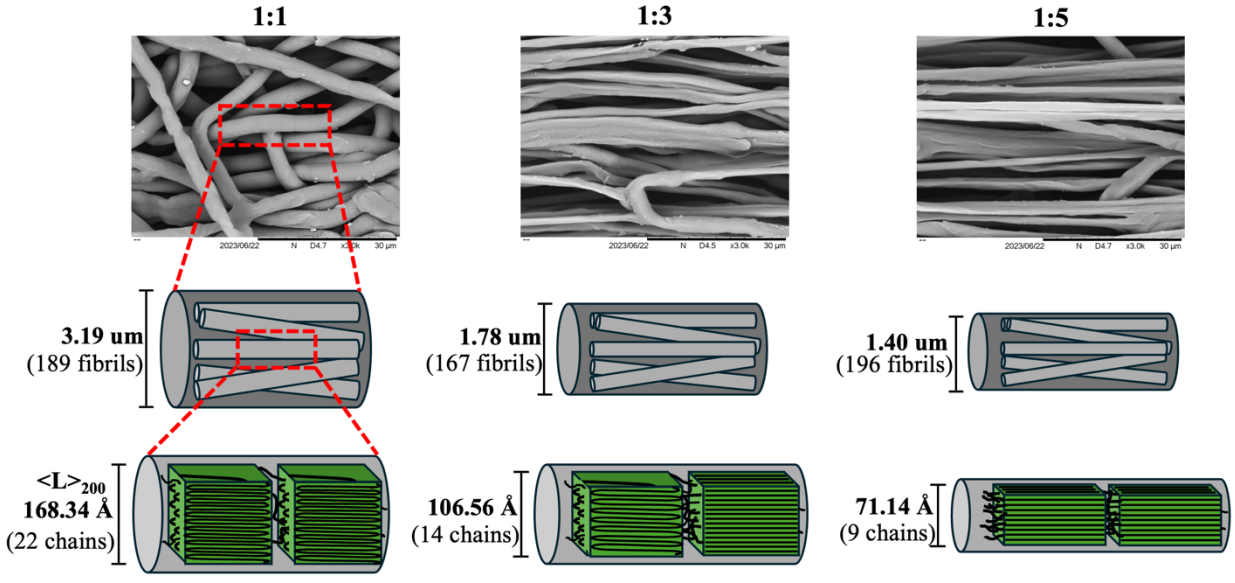

Fig. 4.7 Simplified schematic of structural hierarchies within filaments stretched to various degrees: (top) SEM micrograph of fibers, (middle) individual fiber containing fibrils, and (bottom) individual fibril containing crystals.

5. Conclusions

5.1 Summary of Supporting Evidence of Model

In this study, ES PCL filaments were uniaxially stretched to varying degrees after electrospinning. With increasing degrees of stretch, microfibers within filaments became more aligned, but also exhibited necking and coalescence resulting from heat dissipated during plastic deformation. The initial stages of microstructural evolution involved melting of small, unstable crystals, lamellar fragmentation of the main CFC crystal population, and amorphous chain extension. Fragmentation of CFC into smaller blocks at low strains was evidenced via 1D XRD by the decrease in average crystal width upon stretching while the fraction of original crystals remained constant. The extension of amorphous chains with stretching was demonstrated via DMTA by an increase in T_g and lower relative energy dissipation during glass transition. At high degrees of strain beyond 1:4, DSC showed the development of a novel, more thermodynamically stable crystal population as the fraction of the original crystal population decreased. This new population was distinct from the original crystals not just in T_m, but also in kinetic barriers to melting. High strains caused unfolding, or 'melting', of laterally wide CFC dominating the crystal fraction of unstretched filaments. Elongated chains, originating from CFC and the amorphous phase, recrystallized into CEC oriented along the stretch axis, as shown via 2D XRD. Stretch temperature and polymer Mw also modulated microstructure. My mechanism for stretch-induced crystal transformation was supported by thermodynamic theory and literature findings on other semicrystalline polymers. These findings reveal significant microstructural changes due to stretching which may have profound mechanical and degradative implications for biomedical applications. Specifically, an increased T_g could make the material less rubbery at physiological

temperatures, while elongated CEC chains might enhance the material's axial tensile stiffness. Further investigation is warranted to explore these potential effects.

5.2 Further Investigatory Suggestions

Single fiber studies might offer value in better understanding fundamental behaviors of this hierarchical material. Single fiber 2D XRD scans could directly display crystal alignment in a fiber without convolution from fiber misalignment within filaments. This is not presently possible with my lab's available equipment, as the XRD is not sensitive enough to detect the weaker diffraction signal from a single fiber. Micro-mechanical measurements would enable discernment of foundational properties that influence the overall performance of Biolig, including the extent to which fiber behavior is additive and affected by factors like fiber-fiber adhesion. Such adhesion could contribute to filament strength (*24*), while also decreasing porosity which is unfavorable from a tissue regeneration perspective.

The effect of strain rate on subsequent microstructure might also be studied, as this is a parameter that can be controlled during manufacturing. Higher strain rates better resist chain relaxation and are hypothesized to be more likely to form CEC than CFC (*128*). Varying thermal conditions also serve as a proxy for different drawing rates, where lower temperatures simulate the effects of fast drawing due to limited mobility. To build off my work on stretch temperature, further experiments should be carried out to disaggregate the influences of temperature and the surrounding fluid medium on coalescence. Experimental conditions could include cold-stretching in air and RT-stretching in water.

Due to the timeframe of this master's degree and the slow hydrolytic rate of PCL, it was not possible to carry out investigations on degradation, such as how it affects mechanical properties and whether CFC and CEC have differential degradation rates. These experiments would enhance microstructural understanding of PCL in an environment more closely resembling its actual application context.

6. Bibliography

1. S. Wu, T. Dong, Y. Li, M. Sun, Y. Qi, J. Liu, M. A. Kuss, S. Chen, B. Duan, State-of-the-art review of advanced electrospun nanofiber yarn-based textiles for biomedical applications. *Applied Materials Today* **27** (2022).

2. B. Sowmya, A. B. Hemavathi, P. K. Panda, Poly (ε-caprolactone)-based electrospun nano-featured substrate for tissue engineering applications: a review. *Progress in Biomaterials* **10**, 91–117 (2021).

3. J. R. Dias, A. Sousa, A. Augusto, P. J. Bártolo, P. L. Granja, Electrospun Polycaprolactone (PCL) Degradation: An In Vitro and In Vivo Study. *Polymers* **14**, 1–15 (2022).

4. A. S. Richard, R. S. Verma, Bioactive nano yarns as surgical sutures for wound healing. *Materials Science and Engineering C* **128**, 112334 (2021).

5. J. Xue, T. Wu, Y. Dai, Y. Xia, U. States, U. States, Electrospinning and Electrospun Nanofibers: Methods, Materials, and Applications. **119**, 5298–5415 (2019).

6. T. Z. Ferreira, "Characterization and modelling of biodegradable biomedical fi," (2022).

7. A. Azari, A. Golchin, M. M. Maymand, F. Mansouri, A. Ardeshirylajimi, Electrospun Polycaprolactone Nanofibers: Current Research and Applications in Biomedical Application. *Advanced Pharmaceutical Bulletin* **12**, 658–672 (2022).

8. R. E. Abhari, P. A. Mouthuy, A. Vernet, J. E. Schneider, C. P. Brown, A. J. Carr, Using an industrial braiding machine to upscale the production and modulate the design of electrospun medical yarns. *Polymer Testing* **69**, 188–198 (2018).

9. R. E. Abhari, A. J. Carr, P. A. Mouthuy, Multifilament electrospun scaffolds for soft tissue reconstruction. *Electrofluidodynamic Technologies (EFDTs) for Biomaterials and Medical Devices: Principles and Advances*, 295–328 (2018).

10. F. Haghighat, S. Abdolkarim, H. Ravandi, Mechanical Properties and In Vitro Degradation of PLGA Suture Manufactured via Electrospinning. **15**, 71–77 (2014).

11. M. Rashid, M. Rashid, J. Dudhia, S. G. Dakin, S. G. Dakin, S. Snelling, S. Snelling, A. Lach, A. Lach, R. D. Godoy, P. A. Mouthuy, P. A. Mouthuy, R. Smith, M. Morrey, M.

Morrey, M. Morrey, A. J. Carr, A. J. Carr, Histological evaluation of cellular response to a multifilament electrospun suture for tendon repair. *PLoS ONE* **15**, 1–17 (2020).

12. S. Wu, R. Zhou, F. Zhou, P. N. Streubel, S. Chen, B. Duan, Materials Science & Engineering C Electrospun thymosin Beta-4 loaded PLGA / PLA nano fi ber / micro fi ber hybrid yarns for tendon tissue engineering application. *Materials Science & Engineering C* **106**, 110268 (2020).

13. L. Savić, E. M. Augustyniak, A. Kastensson, S. Snelling, R. E. Abhari, M. Baldwin, A. Price, W. Jackson, A. Carr, P. A. Mouthuy, Early development of a polycaprolactone electrospun augment for anterior cruciate ligament reconstruction. *Materials Science and Engineering C* **129** (2021).

14. A. J. Robinson, A. Pérez-Nava, S. C. Ali, J. B. González-Campos, J. L. Holloway, E. M. Cosgriff-Hernandez, Comparative analysis of fiber alignment methods in electrospinning. *Matter* **4**, 821–844 (2021).

15. S. Z. D. Cheng, S. Jin, Crystallization and melting of metastable crystalline polymers. *Handbook of Thermal Analysis and Calorimetry* **3**, 167–195 (2002).

16. E. K. Kostakova, L. Meszaros, G. Maskova, L. Blazkova, T. Turcsan, D. Lukas, Crystallinity of Electrospun and Centrifugal Spun Polycaprolactone Fibers: A Comparative Study. *Journal of Nanomaterials* **2017** (2017).

17. R. Augustine, S. Thomas, N. Kalarikkal, In Vitro Degradation of Electrospun Polycaprolactone Membranes in Simulated Body Fluid. *International Journal of the Institute of Materials Malaysia* **2**, 211–220 (2014).

18. Z. Song, X. Hou, L. Zhang, S. Wu, Enhancing crystallinity and orientation by hot-stretching to improve the mechanical properties of electrospun partially aligned polyacrylonitrile (PAN) nanocomposites. *Materials* **4**, 621–632 (2010).

19. W. Zhang, C. Zhou, Y. Zhang, F. Xue, B. Luo, H. Li, X. Ren, J. Li, Y. Shang, Z. Wu, S. Jiang, Direct investigations of temperature related structure transitions in strained poly(butylene succinate) with SAXS and WAXS. *Colloid and Polymer Science* **294**, 321–328 (2016).

20. Y. Tang, Y. Lin, H. Lin, C. Li, B. Zhou, X. Wang, Effects of room temperature stretching and annealing on the crystallization behavior and performance of polyvinylidene fluoride hollow fiber membranes. *Membranes* **10**, 1–14 (2020).

21. D. A. Brennan, K. Shirvani, C. D. Rhoads, S. E. Lofland, V. Z. Beachley, Electrospinning and post-drawn processing effects on the molecular organization and mechanical properties of polyacrylonitrile (PAN) nanofibers. *MRS Communications* **9**, 764–772 (2019).

22. M. V. Natu, H. C. De Sousa, M. H. Gil, Influence of polymer processing technique on long term degradation of poly(ε-caprolactone) constructs. *Polymer Degradation and Stability* **98**, 44–51 (2013).

23. A. K. Pandey, V. Katiyar, H. Takagi, N. Shimizu, N. Igarashi, S. Sasaki, S. Sakurai, Structural evolution in isothermal crystallization process of poly(L-lactic acid) enhanced by silk fibroin nano-disc. *Materials* **12** (2019).

24. X. Li, H. Xie, J. Lin, Y. Zeng, Microstructure evolution of electrospun polyvinylidene fluoride fibers via stretching at varying temperatures. *Polymer* **262**, 125434 (2022).

25. F. Selli, U. H. Erdoğan, R. Hufenus, E. Perret, Mesophase in melt-spun poly(ϵ-caprolactone) filaments: Structure–mechanical property relationship. *Polymer* **206** (2020).

26. M. Burman, A. Arinstein, E. Zussman, Do surface effects explain the unique elasticity of polymer nanofibers? *Epl* **96** (2011).

27. S. C. Wong, A. Baji, S. Leng, Effect of fiber diameter on tensile properties of electrospun poly(ε-caprolactone). *Polymer* **49**, 4713–4722 (2008).

28. P. S. Clay, N. Fibers, Y. Ji, B. Li, S. Ge, J. C. Sokolov, M. H. Rafailovich, Structure and Nanomechanical Characterization of Electrospun. 1321–1328 (2006).

29. C. T. Lim, E. P. S. Tan, S. Y. Ng, Effects of crystalline morphology on the tensile properties of electrospun polymer nanofibers. *Applied Physics Letters* **92**, 2011–2014 (2008).

30. A. Arinstein, M. Burman, O. Gendelman, E. Zussman, Effect of supramolecular structure on polymer nanofibre elasticity. *Nature Nanotechnology 2007 2:1* **2**, 59–62 (2007).

31. X. Wang, H. Zhao, L. S. Turng, Q. Li, Crystalline morphology of electrospun poly(ε-caprolactone) (PCL) nanofibers. *Industrial and Engineering Chemistry Research* **52**, 4939–4949 (2013).

32. H. Bittiger, R. H. Marchessault, W. D. Niegisch, Crystal structure of poly-ε-caprolactone. *Acta Crystallographica Section B Structural Crystallography and Crystal Chemistry* **26**, 1923–1927 (1970).

33. Y. Chatani, Y. Okita, H. Tadokoro, Y. Yamashita, Structural Studies of Polyesters. III. Crystal Structure of Poly-ε-caprolactone. *Polymer Journal* **1**, 555–562 (1970).

34. W. Kossack, M. Schulz, T. Thurn-Albrecht, J. Reinmuth, V. Skokow, F. Kremer, Temperature-dependent IR-transition moment orientational analysis applied to thin supported films of poly-ϵ-caprolactone. *Soft Matter* **13**, 9211–9219 (2017).

35. M. Bartnikowski, T. R. Dargaville, S. Ivanovski, D. W. Hutmacher, Degradation mechanisms of polycaprolactone in the context of chemistry, geometry and environment. *Progress in Polymer Science* **96**, 1–20 (2019).

36. M. Labet, W. Thielemans, Synthesis of polycaprolactone: a review. *Chem. Soc. Rev.* **38**, 3484–3504 (2009).

37. L. A. Bosworth, S. Downes, Physicochemical characterisation of degrading polycaprolactone scaffolds. *Polymer Degradation and Stability* **95**, 2269–2276 (2010).

38. D. Łysik, J. Mystkowska, G. Markiewicz, P. Deptuła, R. Bucki, The influence of mucin-based artificial saliva on properties of polycaprolactone and polylactide. *Polymers* **11** (2019).

39. M. I. Hassan, N. Sultana, S. Hamdan, Bioactivity assessment of poly(ε -caprolactone)/hydroxyapatite electrospun fibers for bone tissue engineering application. *Journal of Nanomaterials* **2014** (2014).

40. E. P. S. Tan, S. Y. Ng, C. T. Lim, Tensile testing of a single ultrafine polymeric fiber. *Biomaterials* **26**, 1453–1456 (2005).

41. Z. K. Walczak, Formation of synthetic fibers. 338 (1977).

42. M. Toft, The Effect of Crystalline Morphology on The Glass Transition and Enthalpic Relaxation in Poly (Ether-Ether-Ketone). 1–85 (2011).

43. H. Assender, Microstructures of Polymers Presentation (2023).

44. A. Askadskii, M. Popova, T. Matseevich, E. Kurskaya, The influence of the degree of crystallinity on the glass transition temperature of polymers. *Advanced Materials Research* **864–867**, 751–754 (2014).

45. A. Mizuno, M. Mitsuiki, M. Motoki, Effect of Crystallinity on the Glass Transition Temperature of Starch. *Journal of Agricultural and Food Chemistry* **46**, 98–103 (1998).

46. P. J. Flory, Thermodynamics of crystallization in high polymers. I. Crystallization induced by stretching. *The Journal of Chemical Physics* **15**, 397–408 (1947).

47. V. Ratta, Semicrystalline Polyimides. *Chemical Engineering* **PhD**, 29–79 (1999).

48. L. Alexander, *X-Ray Diffraction Methods in Polymer Science* (John Wiley & Sons, Inc, 1969).

49. A. Peterlin, E. W. Fischer, Thermodynamische Stabilität makromolekularer Kristalle - I. Der Einfluß der Longitudinalschwingungen der Kettenmoleküle. *Zeitschrift für Physik* **159**, 272–287 (1960).

50. M. Kobayashi, M. Sakashita, Morphology dependent anomalous frequency shifts of infrared absorption bands of polymer crystals: Interpretation in terms of transition dipole-dipole coupling theory. *The Journal of Chemical Physics* **96**, 748–760 (1992).

51. B. Wunderlich, Melting Point Variations in Linear High Polymers. *Thermochimica Acta* **4**, 175–188 (1972).

52. B. Wunderlich, Extended Chain Crystals of Linear High Polymers. 49–63.

53. T. Kongkhlang, K. Tashiro, M. Kotaki, S. Chirachanchai, Electrospinning as a new technique to control the crystal morphology and molecular orientation of polyoxymethylene nanofibers. *Journal of the American Chemical Society* **130**, 15460–15466 (2008).

54. T. Arakawa, B. Wunderlich, Thermodynamic Properties of Extended Chain Polymethylene Single Crystals. 653–658 (1967).

55. J. Hu, M. A. Jahid, N. Harish Kumar, V. Harun, *Fundamentals of the Fibrous Materials* (2020).

56. P. A. Mouthuy, N. Zargar, O. Hakimi, E. Lostis, A. Carr, Fabrication of continuous electrospun filaments with potential for use as medical fibres. *Biofabrication* **7** (2015).

57. Theoretical Background of Coherence, *Quantitative orientation analysis*. https://bigwww.epfl.ch/demo/orientationj/theoretical-background.pdf.

58. D. Papkov, N. Delpouve, L. Delbreilh, S. Araujo, T. Stockdale, S. Mamedov, K. Maleckis, Y. Zou, M. N. Andalib, E. Dargent, V. P. Dravid, M. V. Holt, C. Pellerin, Y. A. Dzenis, Quantifying Polymer Chain Orientation in Strong and Tough Nanofibers with Low Crystallinity: Toward Next Generation Nanostructured Superfibers. *ACS Nano* **13**, 4893–4927 (2019).

59. X. Wang, H. Zhao, L. S. Turng, Q. Li, Crystalline morphology of electrospun poly(ε-caprolactone) (PCL) nanofibers. *Industrial and Engineering Chemistry Research* **52**, 4939–4949 (2013).

60. B. Bandeira, E. L. V. Lewis, D. C. Barton, I. M. Ward, The degree of crystalline orientation as a function of draw ratio in semicrystalline polymers: a new model based on the geometry of the crystalline chain slip mechanism. *J Mater Sci* **51**, 228–235 (2016).

61. Z. Bashir, Measurement of orientation in uniaxially drawn polyacrylonitrile. *Acta Polymerica* **47**, 125–129 (1996).

62. V. B. Gupta, S. Kumar, Determination of Crystallite Orientation in Polyethylene Terephthalate Fibers. *Textile Research Journal* **49**, 405–406 (1979).

63. Z. W. Wilchinsky, On Crystal Orientation in Polycrystalline Materials. *Journal of Applied Physics* **30**, 792–792 (1959).

64. Z. W. Wilchinsky, Measurement of Orientation in Polypropylene Film. *Journal of Applied Physics* **31**, 1969–1972 (1960).

65. A. M. Jordan, “Fiber-Composite In Situ Fabrication: Multilater Coextrusion as an Enabling Technology,” thesis, Case Western Reserve University (2016).

66. H. Koerner, Y. Luo, X. Li, C. Cohen, R. C. Hedden, C. K. Ober, Structural Studies of Extension-Induced Mesophase Formation in Poly(diethylsiloxane) Elastomers: In Situ Synchrotron WAXS and SAXS. *Macromolecules* **36**, 1975–1981 (2003).

67. S. Ran, D. Fang, X. Zong, B. S. Hsiao, B. Chu, P. M. Cunniff, Structural changes during deformation of Kevlar fibers via on-line synchrotron SAXS/WAXD techniques. *Polymer* **42**, 1601–1612 (2001).

68. M. Yuan, B. Li, S. Zhang, R. Rajagopalan, M. T. Lanagan, High-Field Dielectric Properties of Oriented Poly(vinylidene fluoride-co-hexafluoropropylene): Structure–Dielectric Property Relationship and Implications for Energy Storage Applications. *ACS Appl. Polym. Mater.* **2**, 1356–1368 (2020).

69. B. Li, C. I. Camilli, P. I. Xidas, K. S. Triantafyllidis, E. Manias, Structured Polyethylene Nanocomposites: Effects of Crystal Orientation and Nanofiller Alignment on High Field Dielectric Properties. *MRS Advances* **2**, 363–368 (2017).

70. W. Li, D. Zhang, C. Qv, R. Zhao, Z. Ma, Stretching-Induced Melting and Recrystallization Polymorphism Revealed in Polybutene-1. *Macromolecules* **56**, 2761–2771 (2023).

71. F. Meyer, K. Oldörp, F. de Jong, Dynamic Mechanical Thermal Analysis (DMTA) on Polymer Composites. *ThermoFisher Scientific* **241**, 1–4 (2021).

72. A. R. Mclauchlin, N. L. Thomas, Biodegradable polymer nanocomposites. *Advances in Polymer Nanocomposites: Types and Applications*, 398–430 (2012).

73. R. Longo, M. Catauro, A. Sorrentino, L. Guadagno, Thermal and mechanical characterization of complex electrospun systems based on polycaprolactone and gelatin. *Journal of Thermal Analysis and Calorimetry* **147**, 5391–5399 (2022).

74. L. de Siqueira, F. R. Passador, A. O. Lobo, E. de S. Trichês, Morphological, thermal and bioactivity evaluation of electrospun PCL/β-TCP fibers for tissue regeneration. *Polimeros* **29**, 1–6 (2019).

75. M. P. Arrieta, A. L. Gil, M. Yusef, J. M. Kenny, L. Peponi, Electrospinning of PCL-based blends: Processing optimization for their scalable production. *Materials* **13**, 1–15 (2020).

76. S. Unal, S. Arslan, B. K. Yilmaz, F. N. Oktar, D. Ficai, A. Ficai, O. Gunduz, Polycaprolactone/gelatin/hyaluronic acid electrospun scaffolds to mimic glioblastoma extracellular matrix. *Materials* **13** (2020).

77. A. Repanas, W. F. Wolkers, Coaxial Electrospinning as a Process to Engineer Biodegradable Polymeric Scaffolds as Drug Delivery Systems for Anti-Inflammatory and

Anti- Thrombotic Pharmaceutical Agents. *Clinical & Experimental Pharmacology* **05** (2015).

78. M. Zhang, X. Li, S. Li, Y. Liu, L. Hao, Electrospun poly(l-lactide)/zein nanofiber mats loaded with Rana chensinensis skin peptides for wound dressing. *Journal of Materials Science: Materials in Medicine* **27**, 1–12 (2016).

79. C. Merlini, G. M. O. Barra, T. Medeiros Araujo, A. Pegoretti, Electrically pressure sensitive poly(vinylidene fluoride)/polypyrrole electrospun mats. *RSC Advances* **4**, 15749–15758 (2014).

80. O. Ero-Phillips, M. Jenkins, A. Stamboulis, Tailoring Crystallinity of Electrospun Plla Fibres by Control of Electrospinning Parameters. *Polymers* **4**, 1331–1348 (2012).

81. M. Ansari, M. Golzar, M. Baghani, M. Soleimani, Shape memory characterization of poly(ε-caprolactone) (PCL)/polyurethane (PU) in combined torsion-tension loading with potential applications in cardiovascular stent. *Polymer Testing* **68**, 424–432 (2018).

82. Q. Shi, K. T. Wan, S. C. Wong, P. Chen, T. A. Blackledge, Do electrospun polymer fibers stick? *Langmuir* **26**, 14188–14193 (2010).

83. Y. He, Y. Inoue, Novel FTIR method for determining the crystallinity of poly(ε-caprolactone). *Polymer International* **49**, 623–626 (2000).

84. M. D. Flamini, T. Lima, K. Corkum, N. J. Alvarez, V. Beachley, Annealing post-drawn polycaprolactone (PCL) nanofibers optimizes crystallinity and molecular alignment and enhances mechanical properties and drug release profiles. *Materials Advances* **3**, 3303–3315 (2022).

85. Z. Song, X. Hou, L. Zhang, S. Wu, Enhancing crystallinity and orientation by hot-stretching to improve the mechanical properties of electrospun partially aligned polyacrylonitrile (PAN) nanocomposites. *Materials* **4**, 621–632 (2010).

86. Z. Wang, B. Sun, X. Lu, C. Wang, Z. Su, Molecular Orientation in Individual Electrospun Nanofibers Studied by Polarized AFM-IR. *Macromolecules* **52**, 9639–9645 (2019).

87. B. Sickler, Tempo Labs Materials Research Laboratory UCSB, Interpreting DSC Data. *DSC interpreting data*, 11 (2022).

88. S. D. Mohan, G. R. Mitchell, F. J. Davis, Chain extension in electrospun polystyrene fibres: A SANS study. *Soft Matter* **7**, 4397–4404 (2011).

89. Determination of Wax Appearance Temperature (WAT) for Crude Oil and Petroleum Products Using Differential Scanning Calorimetry (DSC) - TA Instruments. https://www.tainstruments.com/applications-notes/determination-of-wax-appearance-temperature-wat-for-crude-oil-and-petroleum-products-using-differential-scanning-calorimetry-dsc/.

90. R. M. Saeed, J. P. Schlegel, C. Castano, R. Sawafta, Uncertainty of Thermal Characterization of Phase Change Material by Differential Scanning Calorimetry Analysis. *International Journal of Engineering Research and Technology* **5**, 405–412 (2016).

91. E. M. Abdelrazek, A. M. Hezma, A. El-khodary, A. M. Elzayat, Spectroscopic studies and thermal properties of PCL/PMMA biopolymer blend. *Egyptian Journal of Basic and Applied Sciences* **3**, 10–15 (2016).

92. M. Ravi, S. Song, J. Wang, R. Nadimicherla, Z. Zhang, Preparation and characterization of biodegradable poly(ε-caprolactone)-based gel polymer electrolyte films. *Ionics* **22**, 661–670 (2016).

93. R. Balu, T. S. Sampath Kumar, M. Ramalingam, S. Ramakrishna, Electrospun polycaprolactone/Poly(1,4-butylene adipate-co-polycaprolactam) blends: Potential biodegradable scaffold for bone tissue regeneration. *Journal of Biomaterials and Tissue Engineering* **1**, 30–39 (2011).

94. M. D. Flamini, T. Lima, K. Corkum, N. J. Alvarez, V. Beachley, Annealing post-drawn polycaprolactone (PCL) nanofibers optimizes crystallinity and molecular alignment and enhances mechanical properties and drug release profiles. *Materials Advances* **3**, 3303–3315 (2022).

95. K. Sownthari, S. A. Suthanthiraraj, Synthesis and characterization of an electrolyte system based on a biodegradable polymer. *Express Polymer Letters* **7**, 495–504 (2013).

96. M. Mochizuki, M. Hirano, Y. Kanmuri, K. Kudo, Y. Tokiwa, Hydrolysis of polycaprolactone fibers by lipase: Effects of draw ratio on enzymatic degradation. *Journal of Applied Polymer Science* **55**, 289–296 (1995).

97. S. A. Hassanzadeh-Tabrizi, Precise calculation of crystallite size of nanomaterials: A review. *Journal of Alloys and Compounds* **968**, 171914 (2023).

98. S. Wu, F. Zhang, Y. Yu, P. Li, X. Yang, J. Lu, S. Ryu, Preparation of PAN-based carbon nanofibers by hot-stretching. *Composite Interfaces* **15**, 671–677 (2008).

99. E. S. Yoo, S. S. Im, Effect of molecular orientation on biodegradability of aliphatic polyester. *Macromolecular Symposia* **142**, 13–21 (1999).

100. Y. Chatani, Y. Okita, H. Tadokoro, Y. Yamashita, Structural Studies of Polyesters. III. Crystal Structure of Poly-ε-caprolactone. *Polymer Journal* **1**, 555–562 (1970).

101. C. Böhm, P. Stahlhut, J. Weichhold, A. Hrynevich, J. Teßmar, P. D. Dalton, The Multiweek Thermal Stability of Medical-Grade Poly(ε-caprolactone) During Melt Electrowriting. *Small* **18**, 1–7 (2022).

102. F. Selli, U. H. Erdoğan, R. Hufenus, E. Perret, Mesophase in melt-spun poly(ϵ-caprolactone) filaments: Structure–mechanical property relationship. *Polymer* **206**, 122870 (2020).

103. A. Avella, R. Mincheva, J. M. Raquez, G. Lo Re, Substantial effect of water on radical melt crosslinking and rheological properties of poly(ε-caprolactone). *Polymers* **13**, 1–16 (2021).

104. J. Li, Y. He, Y. Inoue, Study on Thermal and Mechanical Properties of Biodegradable Blends of Poly(e-caprolactone) and Lignin. *Polymer Journal* **33**, 336–343 (2001).

105. R. Young, P. Lovell, "Introduction to Polymers" in *Introduction to Polymers* (EBSCO Publishing, 2011), pp. 531–555.

106. D. V. Badami, F. P. Chappel, M. F. Culpin, D. M. Jones, T. C. Tranter, The effect of extension on the structure of filaments of 6.6-nylon. *Rheologica Acta* **1**, 639–647 (1961).

107. P. Skoglund, A. Fransson, Continuous cooling and isothermal crystallization of polycaprolactone. *Journal of Applied Polymer Science* **61**, 2455–2465 (1996).

108. A. Wurm, M. Merzlyakov, C. Schick, Reversible melting during crystallization of polymers studied by temperature modulated techniques (TMDSC, TMDMA). *Journal of Thermal Analysis and Calorimetry* **60**, 807–820 (2000).

109. K. Li, D. Battegazzore, O. Monticelli, A. Fina, Polycaprolactone / graphite nanoplates composite nanopapers Experimental part Materials.

110. R. B. Cassel, How Tzero Technology Improves DSC Performance Part III: The Measurement of Specific Heat Capacity. *Ta 279*, 1–4 (2001).

111. J. Pal, S. Sanwaria, A. Choudhary, K. Thakur, B. Nandan, R. K. Srivastava, Thermally Initiated Trans-esterification in Poly(ε-caprolactone) and Its Dependence on Molecular Weight. *Journal of Polymers and the Environment* **22**, 479–487 (2014).

112. M. J. Hill, P. J. Barham, Ostwald ripening in polyethylene blends. *Polymer* **36**, 3369–3375 (1995).

113. A. Fernández-Tena, R. A. Pérez-Camargo, O. Coulembier, L. Sangroniz, N. Aranburu, G. Guerrica-Echevarria, G. Liu, D. Wang, D. Cavallo, A. J. Müller, Effect of Molecular Weight on the Crystallization and Melt Memory of Poly(ϵ-caprolactone) (PCL). *Macromolecules* **56**, 4602–4620 (2023).

114. T. Kamal, T. J. Shin, S.-Y. Park, Uniaxial Tensile Deformation of Poly(ε-caprolactone) Studied with SAXS and WAXS Techniques Using Synchrotron Radiation. *Macromolecules* **45**, 8752–8759 (2012).

115. I. Vozniak, R. Hosseinnezhad, J. Morawiec, A. Galeski, Microstructural Evolution of Poly(ε-Caprolactone), Its Immiscible Blend, and In Situ Generated Nanocomposites. *Polymers (Basel)* **12**, 2587 (2020).

116. Z. Wang, Y. He, A. J. Müller, Using PCL oligomers to study the differences in melting behavior between polymers and small molecules crystals. *Polymer* **271**, 125783 (2023).

117. G. Strobl, *The Physics of Polymers: Concepts for Understanding Their Structure Aand Behavior* (New York, 1997).

118. R. A. L. Jones, *Soft Condensed Matter* (Oxford University Press, Oxford, 2002).

119. A. Toda, R. Androsch, C. Schick, Melting Kinetics of Superheated Polymer Crystals Examined by Isothermal and Nonisothermal Fast Scanning Calorimetry. *Macromolecules* **54**, 8770–8779 (2021).

120. A. Toda, M. Hikosaka, K. Yamada, Superheating of the melting kinetics in polymer crystals: A possible nucleation mechanism. *Polymer* **43**, 1667–1679 (2002).

121. P. H. Lindenmeyer, Theory of polymer-chain folding. *The Journal of Chemical Physics* **46**, 1902–1907 (1967).

122. P. H. Lindenmeyer, Theory of polymer-chain folding. *The Journal of Chemical Physics* **46**, 1902–1907 (1967).

123. M. Yasuniwa, C. Nakafuku, T. Takemura, Melting and Crystallization Process of Polyethylene under High Pressure. *Polymer Journal* **4**, 526–533 (1973).

124. A. J. Pennings, A. M. Kiel, Fractionation of polymers by crystallization from solution, III. On the morphology of fibrillar polyethylene crystals grown in solution. *Kolloid-Z.u.Z.Polymere* **205**, 160–162 (1965).

125. T. Kongkhlang, K. Tashiro, M. Kotaki, S. Chirachanchai, Electrospinning as a new technique to control the crystal morphology and molecular orientation of polyoxymethylene nanofibers. *Journal of the American Chemical Society* **130**, 15460–15466 (2008).

126. Y. Liu, L. Cui, F. Guan, Y. Gao, N. E. Hedin, L. Zhu, H. Fong, Crystalline Morphology and Polymorphic Phase Transitions in Electrospun Nylon 6 Nanofibers. *Macromolecules* **40**, 6283–6290 (2007).

127. G. K. Elyashevich, V. G. Baranov, S. Ya. Frenkel, Thermodynamics of crystallization of macromolecules of various degrees of coiling. *Journal of Macromolecular Science, Part B* **13**, 255–289 (1977).

128. Y. Nie, H. Gao, W. Hu, Variable trends of chain-folding in separate stages of strain-induced crystallization of bulk polymers. *Polymer* **55**, 1267–1272 (2014).

129. Y. Zhang, P.-Y. Ben Jar, S. Xue, L. Li, Quantification of strain-induced damage in semi-crystalline polymers: a review. *J Mater Sci* **54**, 62–82 (2019).

130. C. T. Lim, E. P. S. Tan, S. Y. Ng, Effects of crystalline morphology on the tensile properties of electrospun polymer nanofibers. *Applied Physics Letters* **92**, 2011–2014 (2008).

131. X. Chen, W. Zhang, K. Ye, L. Meng, F. Lv, T. Cao, C. Wan, X. Chen, L. Li, Stretch-Induced Melting and Recrystallization of Polyethylene-Plasticizer Film Studied by In Situ X-Ray Scattering: A Thermodynamic Point of View. *Journal of Polymer Science, Part B: Polymer Physics* **56**, 1521–1528 (2018).

132. Y. Liu, L. Yin, H. Zhao, G. Song, F. Tang, L. Wang, H. Shao, Y. Zhang, Strain-induced structural evolution during drawing of poly(ethylene terephthalate) fiber at different temperatures by *in situ* synchrotron SAXS and WAXD. *Polymer* **119**, 185–194 (2017).

133. Z. Bartczak, A. Vozniak, Deformation Instabilities and Lamellae Fragmentation during Deformation of Cross-linked Polyethylene. *Polymers (Basel)* **11**, 1954 (2019).

134. R. Hiss, S. Hobeika, C. Lynn, G. Strobl, Network Stretching, Slip Processes, and Fragmentation of Crystallites during Uniaxial Drawing of Polyethylene and Related Copolymers. A Comparative Study. *Macromolecules* **32**, 4390–4403 (1999).

135. A. Peterlin, Molecular model of drawing polyethylene and polypropylene. *J Mater Sci* **6**, 490–508 (1971).

136. R. Séguéla, Plasticity of semi-crystalline polymers: crystal slip versus melting-recrystallization. *e-Polymers* **7** (2007).

137. X. Liu, L. Zou, B. Chang, H. Shi, Q. Yang, K. Cheng, T. Li, K. Schneider, G. Heinrich, C. Liu, C. Shen, Strain dependent crystallization of isotactic polypropylene during solid-state stretching. *Polymer Testing* **104**, 107404 (2021).

138. Y.-H. Zhou, J. Yang, Z.-P. Zhou, T.-F. Hao, Y.-J. Nie, Molecular Dynamics Simulations of Stretch-Induced Crystal Changes in Crystallized Polyethylene/Carbon Nanotubes Nanocomposites. *Chin J Polym Sci* **41**, 1425–1438 (2023).

139. Y. Men, Critical Strains Determine the Tensile Deformation Mechanism in Semicrystalline Polymers. *Macromolecules* **53**, 9155–9157 (2020).

140. T. Matsumoto, T. Kawai, H. Maeda, Molecular Unfolding in the Drawing Process of Polyethylene Films. *Macromolecular Chemistry* **107**, 250–252 (1967).

141. S. Xu, J. Zhou, P. Pan, Strain-induced multiscale structural evolutions of crystallized polymers: From fundamental studies to recent progresses. *Progress in Polymer Science* **140**, 101676 (2023).

142. D. A. Brennan, M. D. Flamini, J. Posselt, C. T. Wagner, V. Beachley, Effect of post-drawing and tension on enzymatic degradation of electrospun polycaprolactone nanofibers. *Materials Today Communications* **34** (2023).

143. D. A. Brennan, M. D. Flamini, J. Posselt, C. T. Wagner, V. Beachley, Effect of post-drawing and tension on enzymatic degradation of electrospun polycaprolactone nanofibers. *Materials Today Communications* **34** (2023).

144. M. Doumeng, L. Makhlouf, F. Berthet, O. Marsan, K. Delbé, J. Denape, F. Chabert, A comparative study of the crystallinity of polyetheretherketone by using density, DSC, XRD, and Raman spectroscopy techniques. *Polymer Testing* **93**, 106878 (2021).

145. Crystals | Free Full-Text | Evaporation-Induced Crystal Nucleation and Morphology of Dried Poly(Vinylidene Fluoride) Droplets. https://www.mdpi.com/2073-4352/11/12/1442.

146. D. J. Blundell, B. N. Osborn, The morphology of poly(aryl-ether-ether-ketone). *Polymer* **24**, 953–958 (1983).

147. D. C. Bassett, R. H. Olley, I. A. M. Al Raheil, On crystallization phenomena in PEEK. *Polymer* **29**, 1745–1754 (1988).

148. G. Vanden Poel, V. B. F. Mathot, High performance differential scanning calorimetry (HPer DSC): A powerful analytical tool for the study of the metastability of polymers. *Thermochimica Acta* **461**, 107–121 (2007).

149. R. B. Cassel, High Heating Rate DSC. **297**, 1–11 (2011).

150. A. Toda, K. Taguchi, K. Nozaki, T. Fukushima, H. Kaji, Superheated Melting Kinetics of Metastable Chain-Folded Polymer Crystals. *Crystal Growth and Design* **18**, 3637–3643 (2018).

151. L. C. Thomas, Modulated DSC #6: Measurement of Initial Crystallinity in Semi-crystalline Polymers. *TA Instruments Technical Paper*, TP011 (2005).

152. M. Schulz, A. Seidlitz, A. Petzold, T. Thurn-Albrecht, The effect of intracrystalline chain dynamics on melting and reorganization during heating in semicrystalline polymers. *Polymer* **196**, 122441 (2020).

153. A. Toda, M. Konishi, An evaluation of thermal lags of fast-scan microchip DSC with polymer film samples. *Thermochimica Acta* **589**, 262–269 (2014).

154. E. Hellmuth, B. Wunderlich, Superheating of Linear High-Polymer Polyethylene Crystals. *Journal of Applied Physics* **36**, 3039–3044 (2004).

155. F. N. Liberti, B. Wunderlich, Melting of polycaprolactam. *Journal of Polymer Science Part A-2: Polymer Physics* **6**, 833–848 (1968).

156. J. S. Youm, J. H. Kim, C. H. Kim, J. C. Kim, Y. A. Kim, K. S. Yang, Densifying and strengthening of electrospun polyacrylonitrile-based nanofibers by uniaxial two-step stretching. *Journal of Applied Polymer Science* **133**, 1–9 (2016).

157. C. Lai, G. Zhong, Z. Yue, G. Chen, L. Zhang, A. Vakili, Y. Wang, L. Zhu, J. Liu, H. Fong, Investigation of post-spinning stretching process on morphological, structural, and mechanical properties of electrospun polyacrylonitrile copolymer nanofibers. *Polymer* **52**, 519–528 (2011).

158. L. Lozano-Sánchez, I. Bagudanch, A. Sustaita, J. Iturbe-Ek, L. Elizalde, M. Garcia-Romeu, A. Elías-Zúñiga, Single-Point Incremental Forming of Two Biocompatible Polymers: An Insight into Their Thermal and Structural Properties. *Polymers* **10**, 391 (2018).

159. E. Zussman, M. Burman, A. L. Yarin, R. Khalfin, Y. Cohen, Tensile deformation of electrospun nylon-6,6 nanofibers. *Journal of Polymer Science, Part B: Polymer Physics* **44**, 1482–1489 (2006).

160. C. Ye, C. Wang, J. Wang, C. G. Wiener, X. Xia, S. Z. D. Cheng, R. Li, K. G. Yager, M. Fukuto, B. D. Vogt, Rapid assessment of crystal orientation in semi-crystalline polymer films using rotational zone annealing and impact of orientation on mechanical properties. *Soft Matter* **13**, 7074–7084 (2017).

161. Q. H. Guo, M. Jia, Z. Liu, Y. Qiu, H. Chen, D. Shen, X. Zhang, Q. Tu, M. R. Ryder, H. Chen, P. Li, Y. Xu, P. Li, Z. Chen, G. S. Shekhawat, V. P. Dravid, R. Q. Snurr, D. Philp, A. C. H. Sue, O. K. Farha, M. Rolandi, J. F. Stoddart, Single-Crystal Polycationic Polymers Obtained by Single-Crystal-to-Single-Crystal Photopolymerization. *Journal of the American Chemical Society* **142**, 6180–6187 (2020).

162. W. J. Sichina, Measurement of Tg by DSC, *Thermal Analysis Application Note* (2018). https://thermalsupport.com/wp-content/uploads/2018/05/PETech-09.pdf.

163. P. B. McDaniel, K. E. Strawhecker, J. M. Deitzel, J. W. Gillespie, Nanoscale interfibrillar adhesion in UHMWPE fibers. *J Polym Sci B Polym Phys* **56**, 391–401 (2018).